A LOW-COST, PORTABLE, WEB-BASED IMPEDANCE SPECTROSCOPE FOR AGRICULTURAL APPLICATIONS

BY

SEOKCHAN YOO

THESIS

Submitted in partial fulfillment of the requirements
for the degree of Master of Science in Agricultural and Biological Engineering
in the Graduate College of the
University of Illinois at Urbana-Champaign, 2017

Urbana, Illinois

Master's Committee:

Associate Professor Kaustubh Bhalerao, Chair
Associate Professor Tony Grift
Associate Professor Robert Knox

Abstract

Electrical impedance spectroscopy (EIS) is an electrochemical characterization technique widely exploited in the field of chemistry, material science, and biology. EIS characterizes the dynamics of fixed and mobile charge carriers at the electrode-sample interface. It has proved useful in the characterization of electrochemical properties of diverse materials, including electrolytic media and biological tissues.

Traditionally, an EIS spectroscope consists of a bulky and expensive electronic system, and handling this equipment can be difficult without proper training. These limitations forestall EIS spectroscopy to be employed for in-field and mobile agricultural applications.To overcome these issues, a low-cost, mobile, web-based EIS spectroscopy device was developed based on the AD5933, a high precision impedance measurement system-on-chip. A user-friendly web application was programmed to promote ease of use and operational simplicity.

Application of the developed spectroscope as demonstrated through four different experiments; measuring standard RC circuits, monitoring copper corrosion, detecting adulterated milk and characterizing the estrous cycle of sows. Based on results from these experiments, it was found that the spectroscope is capable of producing accurate data as well as capturing different electrochemical characteristics for agricultural applications. Most importantly, the spectroscope shows its potential to be used as a decision-making tool to optimize artificial insemination in swine breeding operations.

To my family and Sarah.

Table of Contents

List of Figures

List of Tables

List of Abbreviations

AC	Alternating Current.
ADC	Analog to Digital Converter.
AFE	Analog Front End.
DC	Direct Curret.
DFT	Discrete Fourier Transform.
DSP	Digital Signal Processor.
EIS	Electrical Impedance Spectroscopy.
FSH	Follicular-Stimulating Hormone.
GnRH	Gonadotrpin-Releasing Hormone.
I^2C	Inter-Integrated Circuit.
LH	Lutenizing Hormone.
MSPS	Millions of Samples Per Second
PGF-α	Prostaglandin Alpha.
SoC	System-on-Chip.

Chapter 1

Introduction to Electrical Impedance Spectroscopy

1.1 Background

Electrical impedance spectroscopy (EIS) is a powerful electrochemical research tool which has been widely used in the field of chemistry, material science, and biology [1–4]. EIS allows the investigation of the dynamics of fixed or mobile charge carriers at the electrode-sample interface [1, 5–7]. It is used to characterize electrical properties of materials, an electrolytic media, as well as biological tissues. A large numbers of studies [1, 4, 5, 8, 9] underline the great potential of EIS due to the following features:

1. **It is fast.** Although measurements at low frequency ranges (<100 Hz) are inherently slow, the entire process of sweeping along a frequency spectrum can usually be completed in a few seconds. Therefore, EIS can be particularly useful to capture changes in the eletrochemical properties of an analyte over time.

2. **It provides rich information about the electrochemical system of interest.** By probing the material over a range of frequencies, one can obtain properties at different scales, from large charge carriers, down to vibrational modes of specific chemical bonds [1]. Collected raw impedance data can be fit to an equivalent circuit model which aids in understanding electrochemical phenomena occurring in the sample.

3. **It is label-free and non-invasive.** EIS is one of few label-free and non-invasive techniques currently available [2, 4]. Typical excitation levels of well under 1V for short durations minimize the impact of the measurement tool and avoid serious perturbations on the measured system.

These advantages of EIS make for attractive possibilities of using the technology in agricultural

sensing applications.

1.2 Theory of Operation

1.2.1 Principle of EIS

Electrical networks are typically modeled using three ideal electrical elements - resistors (R), capacitors (C), and inductors (L). Each element models a unique relationship between the voltage (V) and the current (I). Electrical resistance, denoted by R, is related to the ability of circuit element to resist the current flow. It describes a relationship between voltage applied across an element and the current that flows through it [5]. This relationship is known as Ohm's Law and is shown in Equation 1.1.

$$R = \frac{V}{I} \tag{1.1}$$

As electrical resistance is measured with direct current (DC) signals, the electrical resistance is restricted to describe pure resistors. In order to model capacitors and inductors mathematically, the concept of electrical impedance was first introduced by Oliver Heaviside in the 1880s [6–8]. Electrical impedance (Z) models not only the property of resistance but also the ability of capacitors and inductors to modulate the availability of electrical energy [2, 6, 8]. Since the behaviors of capacitors and inductors depend on the frequency, impedance is measured by injecting a small amplitude alternating current (AC) excitation voltage signal followed by measuring the corresponding current response. Analogous to Ohm's Law, impedance is calculated as a complex ratio of AC input voltage to AC output current. Impedance is modeled as a complex number; thus it can be expressed as a polar form consisting of impedance magnitude ($|Z|$) and frequency dependent phase shift (ϕ). As stated by Euler's relationship, polar form of impedance can also be represented in a Cartesian form consisting of real (Z_{Re}) and imaginary (Z_{Im}) impedance. This is illustrated graphically in 1.1 and 1.2. Equation 1.2 expresses the impedance in three different forms:

$$Z(jw) = \frac{Vsin(wt)}{Isin(wt)} = |Z|e^{\phi t} = Z_{Re} + jZ_{Im} \tag{1.2}$$

where V and I denote the maximum voltage and current signals, ω is the angular frequency, t is the time, and ϕ is the phase difference between the voltage and the current signals. Therefore, complex impedance represents the impedance value at one particular frequency [1].

In a purely resistive circuit, the AC voltage response has the same phase as the excitation signal, i.e. the phase shift is always zero. However, with capacitors and inductors, their charge storing properties (i.e., reactance) cause the response waveform to respectively lag or lead the excitation in the waveform when visualized in the time domain. This difference in time between the excitation and response signals is represented as the phase shift which is defined as the ratio between resistive and reactive elements of the output signal. The value of phase shift can be easily calculated using the ratio of the imaginary and the real impedances based on the Equation 1.3.

$$\phi = \arctan(\frac{Z_{Im}}{Z_{Re}}) \tag{1.3}$$

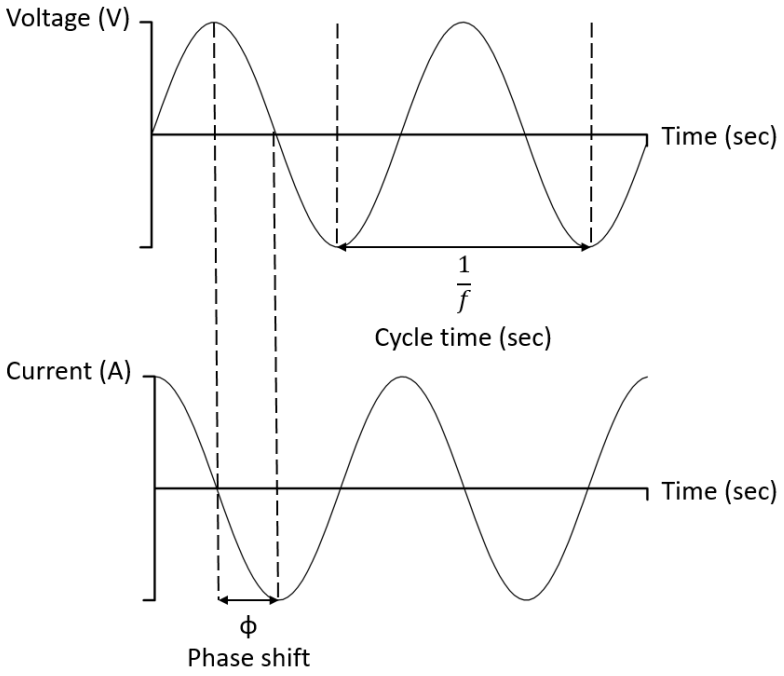

Figure 1.1: Graphical representation of voltage and current signals in time domain [5].

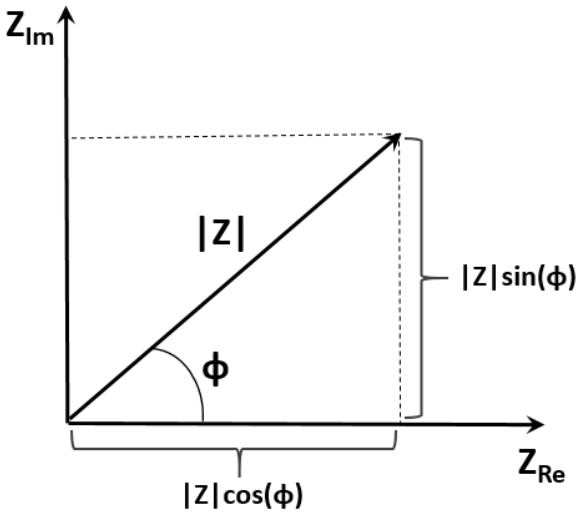

Figure 1.2: Graphical representation of complex impedance in Catesian and polar form.

1.2.2 Measuring electrochemical parameters

Impedance is a direct way of interrogating the electrochemical properties of a system. Measuring the impedance of an electrochemical system typically involves electrodes in contact with an electrolyte solution. When electrodes are electrically stimulated, various microscopic processes take place within an electrochemical system [1]. While the raw impedance data is unable to directly shed light on the electrochemical phenomena under study, it is possible to model aspects of the complex electrochemical system as an equivalent pure electrical system that produces the observed response. Lvovich describes six parameters that can be used to represent a microscopic process of an electrochemical system regarding simple analogous electrical properties [5].

Uncompensated impedance, Z_{ohm}

The uncompensated impedance arises from inherent nature of wires, connectors, and electrodes. It can be represented by a simple resistor-capacitor-inductor circuit (RLC) circuit that consists of a resistor and an inductor series in parallel with a capacitor. As a result, the uncompensated impedance can be estimated by calculating the equivalent impedance of this circuit.

For the most of cables, the values of R_{ohm}, C_{ohm}, and L_{ohm} are approximated to be 1 Ω, $1pF$, and $10^{-4}mH$ respectively. Due to the very small inductance, all current flows through a resistor at a low frequency range where the effect of a capacitor and an inductor become negligibly small. On the other hand, the inductance effect becomes significant at a frequency range above 1 MHz. Therefore, the equivalent impedance can be simplified as the Equation 1.4 at a high frequency range.

$$Z_{ohm} \sim R_{ohm} + \frac{\omega L_{ohm}}{1 - \omega^2 C_{ohm} L_{ohm}} \tag{1.4}$$

As almost all cables exhibit some inductance. The adverse effect of uncompensated impedance becomes apparent when the impedance of the unknown sample is relatively small in comparison to the uncompensated impedance at a very high frequency range. In other words, the uncompensated impedance must be taken account for frequency range above 1 MHz when the impedance data is interpreted. However, since the uncompensated impedance is approximated to be very small for

a typical cable at a frequency below MHz range (1 Ω), it is often omitted during the data fitting process. Also, the uncompensated impedance can be alleviated by twisting wires or placing wires properly [5].

Solution resistance, R_{sol}

For a current to flow, there must exist conducting species such as ions and electrons present near the electrodes. The solution resistance is the resistance of electrolytic media between the measuring electrodes and R_{sol} is one of essential parameters obtained from EIS. The solution resistance is directly due to the migration of ions between the bulk media and the electrodes. Thus R_{sol} is a measure of the availability of conducting species in the solution.

Electrical double layer capacitance, C_{dl}

In 1853, Helmholtz and Stern first described the formation of an electrical double layer (EDL) which shows capacitive charging behavior when ions and charged species from bulk solution stick to the electrode surface. Figure 1.3 illustrates three components of the EDL [5, 9]: The Inner Helmholtz Plane (IHP) is composed of charged species specifically adsorbed onto the metal electrode surface. The Outer Helmholtz Plane (OHP) is composed of electrostatically attracted species. The outermost Diffusion Layer is formed by electroactive species coming from the bulk media. At low frequencies, electroactive ions move slowly between electrodes resulting in a severe blocking effect by the EDL capacitance. On the other hand, ions are supplied to the electrode surface at high speed during high frequency so that the effect of EDL capacitance is decreased. Typical EDL capacitance values of ionic and nonpolar solutions are reported to be 10-60 $\frac{\mu f}{cm^2}$ and 1 $\frac{\mu f}{cm^2}$ respectively [5].

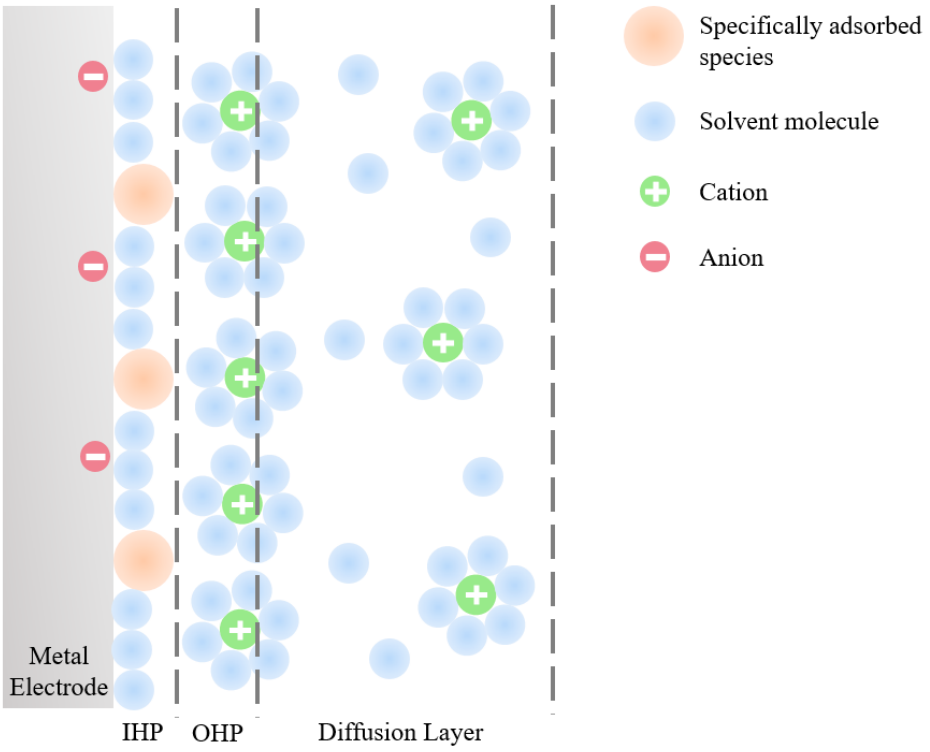

Figure 1.3: Helmholtz-Stern's model at the electrode-sample interface [5,9]. The negatively charged electrode interface is shown on the left. Inner Helmholtz layer (IHP) is formed with specifically adsorbed species at the electrode interface. The positively charged cation species are aligned along the electrode interface forming Outer Helmholtz layer (OHP). A diffusion layer, composed of electrostatically attracted spcies at some distance from the electrode, is formed. The electrical double layer (EDL) structure consists of IHP, OHP, and a diffusion layer.

Charge transfer resistance R_{ct}

The charge transfer resistance (R_{ct}) is the resistance formed by an electrochemical reaction at the electrode-electrolyte interface. When an external voltage is applied to the electrodes, electric charges are transferred between electrodes. If adsorbed species on the electrodes are reactive, then electrochemical redox reaction occurs. This process is controlled by the Faradaic response, which is the rate of electron transfer to electroactive species near the surface of the electrode. The speed of this process depends on the concentration of electroactive species, type of reaction, applied voltage, temperature, pressure, the surface area of the electrode, and convection [5]. In general, Faradaic current can be estimated using Faraday's law 1.5:

$$i = i_0[\frac{C_o}{C^{*o}}\exp\frac{\alpha \mathrm{nF}\eta}{\mathrm{RT}} - (\frac{C_R}{C^{*R}}\exp\frac{(1-\alpha)\mathrm{nF}\eta}{\mathrm{RT}})] \tag{1.5}$$

where i_0 is exchange current density or rate of reaction, n is number of electrons involved in reaction, α is order of reaction, F is Faraday's constant, R is the gas constant, T is temperature, η is overpotential (i.e. the difference between the applied voltage and the open circuit voltage), C_o is the concentration of oxidant at the electrode surface, C_R is the concentration of reductant at the electrode surface, and C_o, C_R are the concentration of oxidant, reductant in the bulk solution respectively. However, the above equation yields to the simpler Butler-Volmer form with an assumption that the concentration of the solution is equal to that at the electrode surface 1.6.

$$i = i_0[\exp\frac{\alpha \mathrm{nF(V-V_{EQ})}}{\mathrm{RT}} - \exp\frac{(1-\alpha)\mathrm{nF(V-V_{EQ})}}{\mathrm{RT}}] \tag{1.6}$$

Note that concentration terms are excluded and the overpotential is replaced by applied voltage V, and equilibrium electrode potential V_{EQ}. When the difference between the applied voltage and the equilibrium electrode potential is subtle, the charge transfer resistance can be expressed as the Equation 1.7 [5, 10].

$$R_{ct} = \frac{RT}{nFi_0} \tag{1.7}$$

The charge transfer resistance should be disregarded if there is no electron transfer process.

However, if there is an electron transfer, the charge transfer resistance must be taken into account to represent an electrochemical reaction. During equivalent circuit model fitting, charge transfer resistance is placed in parallel with electrical double layer capacitance in order to demonstrate the fact that electroactive species must tunnel through the double layer to reach the surface of the electrode [5]. As the Equation 1.7 illustrates, the charge transfer resistance can be used to calculate the exchange current density, and the charge transfer resistance is inversely related to the rate of reaction.

Sorption impedance, Z_{sorp}

The sorption impedance occurs due to the current resulting from kinetics of adsorbed/desorbed molecules in the region of EDL [5]. These species do not exchange electrons and therefore typically do not produce a Faradic current, but they alter the surface charge density. Interfacial kinetics of sorption impedance are considered negligible compared to other interfacial processes such as charge transport and mass transport, hence it is frequently omitted during the data fitting process.

Diffusion impedance, Z_W

Diffusion process occurs when there is a concentration gradient in an electrochemical system. This concentration gradient is manifested by consumption of reactive species at the electrode interface due to adsorption and charge transfer reaction. Consequently, the diffusion impedance (also known as the mass transport impedance or Warburg impedance) is used to reveal the amount of species moved from the bulk solution to the electrode surface and the amount of reactants transported from electrode surface to bulk media.

The diffusion impedance is frequently employed in the full Randles model or mixed charge transfer and diffusion controlled models. As the charge transfer reaction consumes reactive species and causes concentration gradient to promote diffusion process, the diffusion impedance is placed in series with the charge transfer resistance to demonstrate the Faradaic process. On the contrary, double layer impedes reactive species to reach the electrode surface. For this reason, double layer capacitance is placed in parallel with Faradaic process elements.

According to Nernst equation described in Equation 1.8 [5], the thickness of diffusion layer can

be estimated:

$$L_D = \sqrt{\frac{D}{2\pi f}} \tag{1.8}$$

whereas L_D is the length of the diffusion layer, D is the diffusion coefficient, and f is the frequency of the applied signal. As one can predict, the thickness of diffusion layer depends on frequency. For example, reactive species at low frequencies are spread out further into the bulk media and move slowly toward the electrode surface causing thicker diffusion layer to be formed. However, reactive species at high frequencies are transported quickly to the electrode surface, causing the thickness of the diffusion layer to decrease. The diffusion impedance is distributed within an electrochemical system. Hence it is expressed with its mathematical equation rather than expressed with ideal, non-distributed circuit elements. More details on equation and impedance behavior are discussed in the following section.

Importance of the low frequency data

Unlike dielectric spectroscopy, which studies the insulating properties of materials, EIS focuses on the analysis of Faradaic and double-layer interfacial kinetics [4, 5]. Kurzweil [11] points out that the high frequency data reflects the conductivity of the electrolyte (R_s), whereas the intermediate frequency data represents charge transfer reactions (R_{ct}) and EDL capacitance (C_{dl}) at the electrode-sample interface. The low frequency data is influenced by the mass transport (Z_W) due to the concentration gradient caused by charge transfer reaction at the electrode surface [11]. Thus the low-intermediate frequency region is more significant than high frequency information to determine the kinetic process is occurring at the electrode interface.

The low-intermediate range of frequency is frequently used to identify electrochemical parameters such as charge transfer resistance, EDL capacitance, and diffusion impedance [6, 11]. For example, a DNA impedance biosensor analyzing samples at a low-intermediate frequency range (0.1 Hz to 5 kHz) has successfully demonstrated the ability to detect DNA bound events at the electrode interface [6]. Also, the low-intermediate frequency region (10 mHz to 1 kHz) was selected to study slow charge transfer kinetics at the interface of hemin paste electrode [12]. Therefore, the recommended low-intermediate frequency range (less than 100 kHz) is used to explore electro-

chemical process at the electrode-sample interface [5, 13].

1.2.3 Data representation and interpretation: An example of Randle's circuit modeling

As discussed, the electrical impedance can be represented in polar and cartesian forms. Accordingly, the measured impedance data can be visualized in two different ways, Nyquist and Bode. The Nyquist plot is a visualization of the cartesian form of impedance. The real part of the impedance is plotted on the x-axis, and the negative imaginary part of the impedance is plotted on the y-axis.

Each point on the Nyquist plot denotes impedance at a specific frequency. As presented in Figure 1.2, frequency decreases from left to right. Nyquist plot can be a great tool when finding relevant parameters of electrochemical systems. Also, possible kinetic mechanisms can be discovered by counting the number of semi-circular shapes on the graph [5, 10, 14]. As an example, EIS can be used to investigate grain boundary of two-phase microstructures such as zirconia [1]. As each arc represents one possible reaction mechanism, two arcs corresponding to two different grain boundary phases appear on Nyquist plot. Therefore, this type of plot is particularly useful in identifying reaction mechanisms of electrochemical systems. However, the Nyquist plot obscures frequency dependence and lacks phase shift information, which is valuable in verifying a capacitive element.

Bode plot is a polar form representation of impedance. Thus, unlike the Nyquist plot, the Bode plot yields two graphs - one corresponds to the impedance while the other corresponds to the phase shift. Bode diagram plots impedance and phase angle on the y-axis against the logarithmic scale of frequency on the x-axis. Bode plot is readily identifies the frequency-dependent behaviors of a system and also useful in estimating electrochemical parameters. Figure 1.3 illustrates an example of a Bode plot.

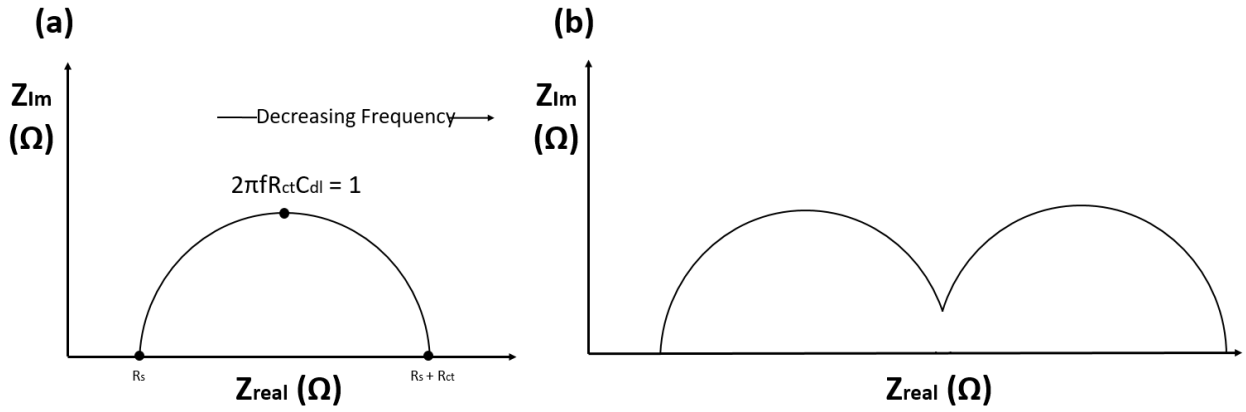

Figure 1.4: Nyquist plots for (a) One reaction system (b) Two reactions system. Note that frequency information is obscured in this type of plot.

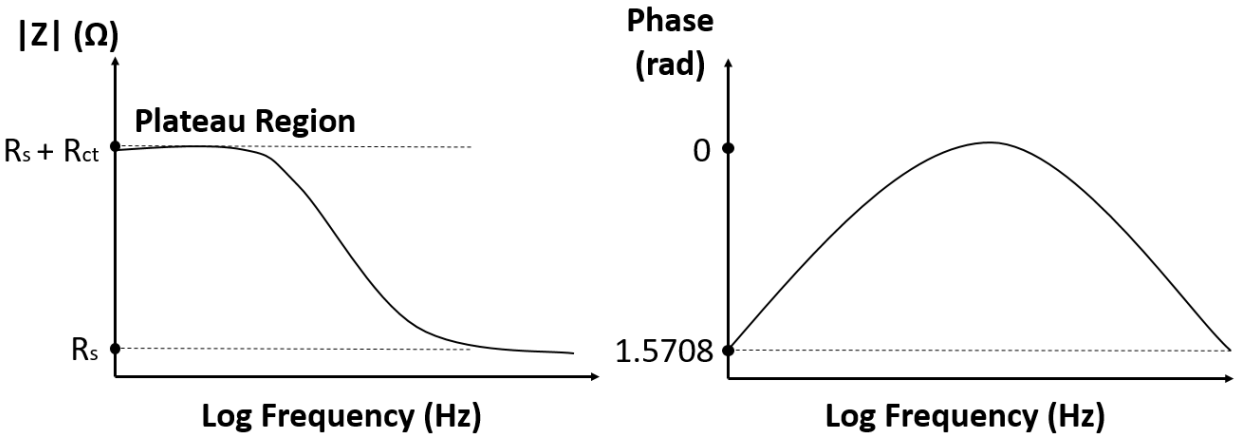

Figure 1.5: An example of Bode plot. Frequency information is explicit compared to the Nyquist plot.

Bode plots are frequently used to estimate solution resistance, charge transfer resistance, and electrical double layer capacitance (C_{dl}). The charge transfer resistance and the solution resistance can be estimated by looking at the diameter of Nyquist plot or plateau region of Bode plot [15]. Once two resistance values are found, the value of C_{dl} is calculated using Equation 1.9:

$$w_{\phi max} = \frac{1}{C_{dl} R_{ct} (1 + \frac{R_{ct}}{R_{sol}})^{\frac{1}{2}}} \tag{1.9}$$

in which $\omega_{\phi max}$ indicates the point at the maximum phase angle [15]. As the phase data reflects important information related to reactive elements, Bode diagram is powerful in providing insight to frequency response behavior.

Upon data representation, EIS data can be interpreted by correlating the measured data to the equivalent circuit (EC) model. Randles and Warburg [5] initially devised the EC model in an attempt to represent physical, electrical, mechanical, and chemical processes occurring in an electrochemical system in pure electrical terms employing ideal electrical elements. However, in real systems, it may not be sufficient to model the system only with ideal elements. Therefore, non-ideal elements such as the diffusion impedance (Z_W) or a constant phase element (CPE) that replaces a double layer capacitance are often used to model the system. Equivalent elements, as well as, impedance and phase representations of elements are shown in Table 1.1. The Bode diagrams of each equivalent element are illustrated in Figure 1.6 1.7 1.8 1.9 1.10.

Equivalent Element	*Impedance (ohms)*	*Phase (rad)*
R	R	0
C	$\frac{1}{jwC}$	-1.5708
L	jwL	1.5708
Z_W	$\frac{Rw}{jw}$	0.7854
Z_{CPE}	$\frac{1}{Q(jw)^n}$	-1.5708*n

Table 1.1: Circuit elements for equivalent circuit model [5, 10]

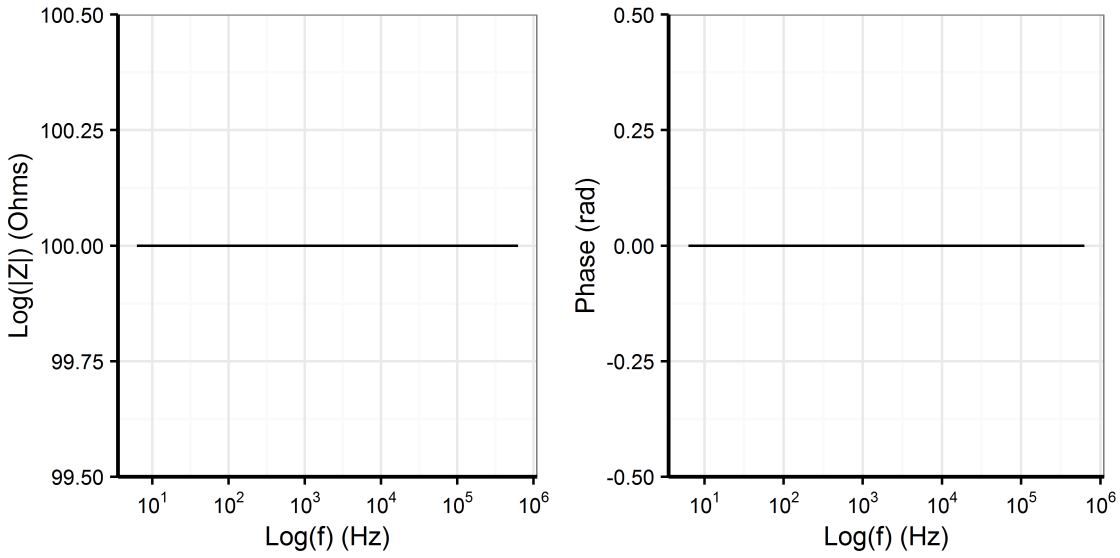

Figure 1.6: Bode diagram for a single resistor.

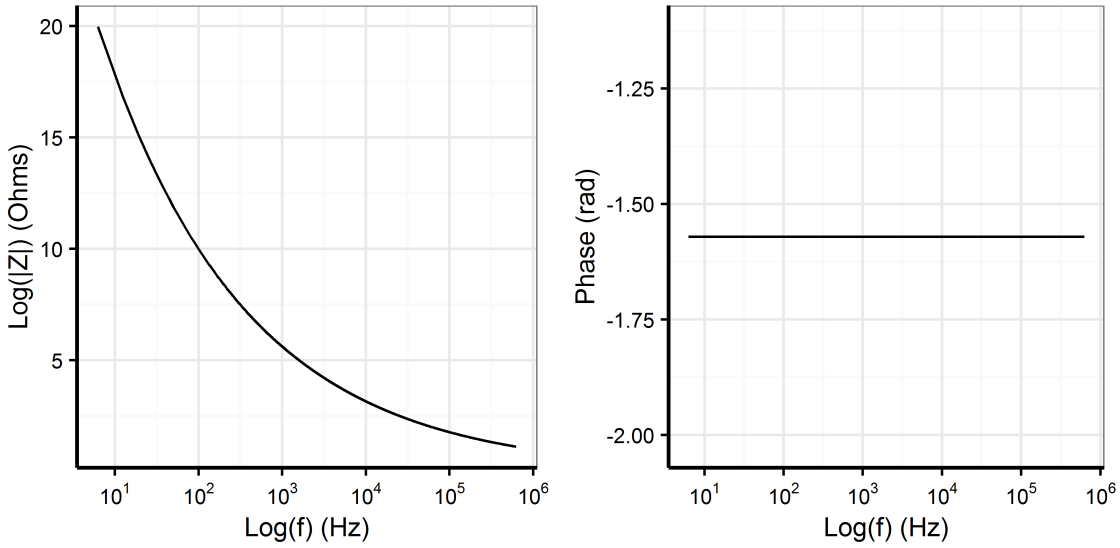

Figure 1.7: Bode diagram for a single capacitor.

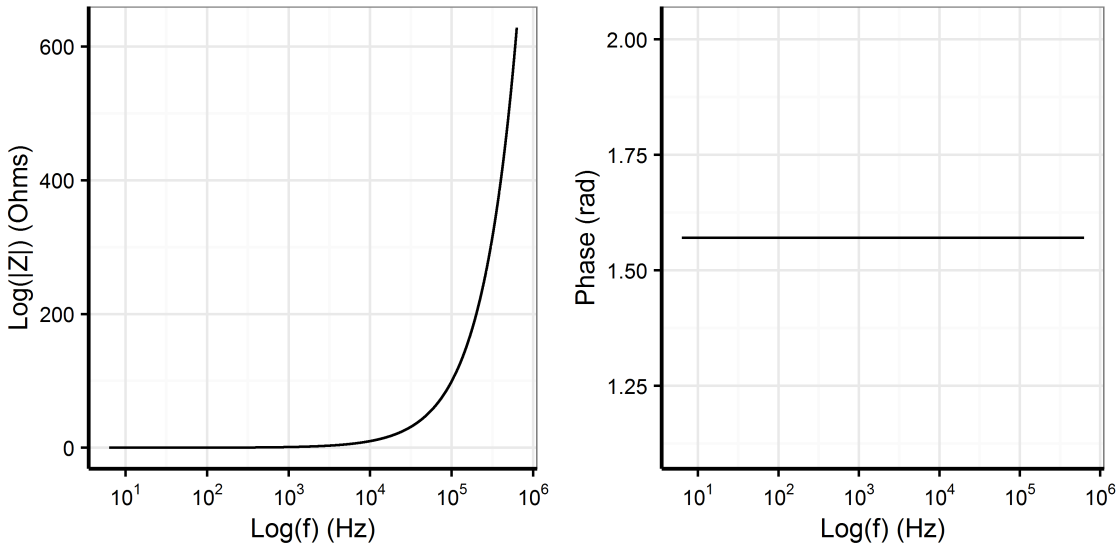

Figure 1.8: Bode diagram for a single inductor.

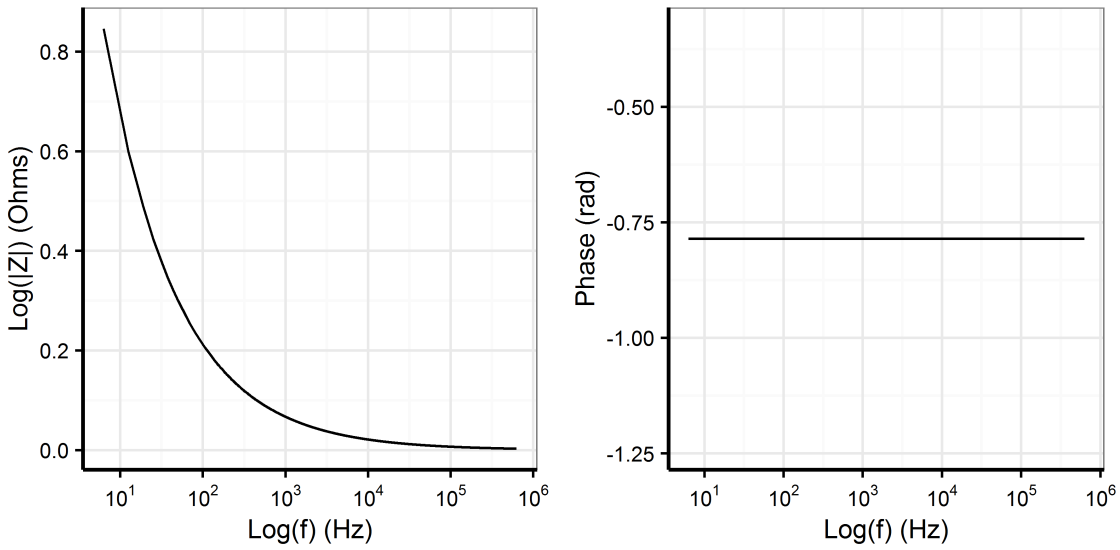

Figure 1.9: Bode diagram for a Warburg element.

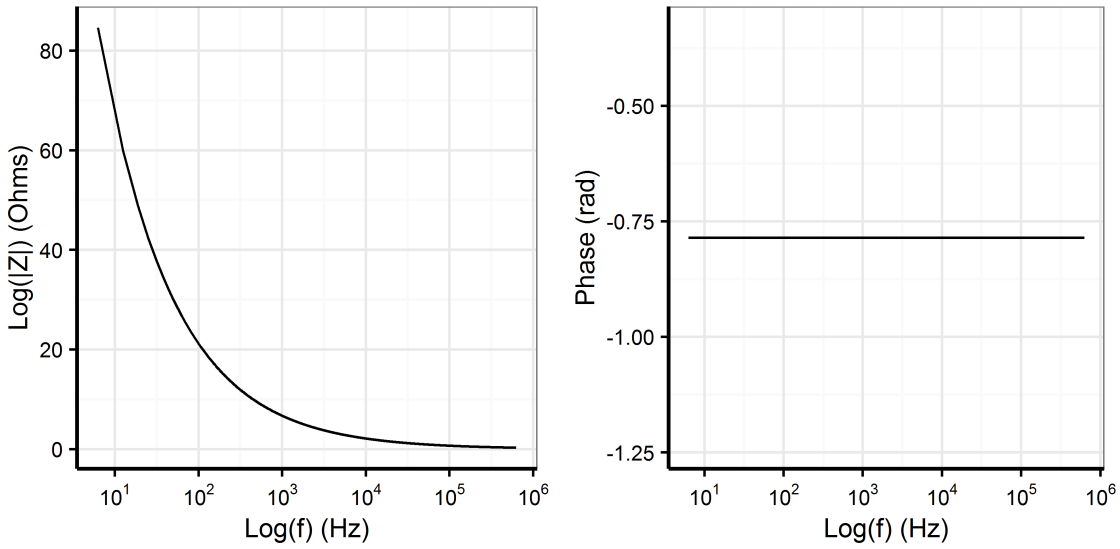

Figure 1.10: Bode diagram for a constant phase element (n=0.5).

As presented in Figure 1.6, a pure resistor does not exhibit phase shift while others do. A capacitor has the highest impedance magnitude at a low frequency with a constant phase shift of -1.5708 rad (Figure 1.7). Conversely, an inductor presents the highest impedance magnitude at a high frequency with a constant phase shift of 1.5708 rad (Figure 1.8). According to Figure 1.9, Warburg element renders a capacitor-like behavior, showing the highest impedance magnitude at a low frequency. However, its phase angle is kept constant at 0.7854 rad. Constant Phase Element (CPE) also behaves like a capacitor, but its phase angle varies with the value of n (Figure 1.10). Noted that if n goes to 1, CPE acts as a pure capacitor. On the other hand, if n goes to 0, CPE acts as a pure resistor.

One major problem in implementing an EC model is in deciding which particular model to represent the electrochemical system among infinite possibilities. To ease this complication, Randles circuit model is commonly employed as a starting model. As Figure 1.11 describes, Randles EC model is designed to investigate the phenomena of mixed charge transfer, homogeneous and diffusion controlled kinetics [5]. Thus, the circuit is composed of bulk properties of electrolyte from solution resistance (R_s), as well as electrode-electrolyte interface properties from EDL capacitance (C_{dl}), charge transfer resistance (R_{ct}), and Warburg impedance (Z_W) [10, 14, 16]. The parallel elements serially connected to R_s models the total current flowing through the electrodes as the sum of contributions from the Faradic process (of R_{ct} and Z_W) and double-layer effect (C_{dl}). From this model, we can derive an equation for the equivalent impedance and phase by performing several steps.

In order to find the real and imaginary components of the Warburg impedance, Cartesian form conversion is done to the original formula of Z_w. The acquired Cartesian form of the Warburg impedance is further simplified with Warburg coefficient σ which includes $\frac{1}{\sqrt{2}}$.

$$Z_W = \frac{R_W}{\sqrt{jw}} = \frac{R_W}{\sqrt{w}}\frac{1}{\sqrt{2}}(1-j) = \frac{\sigma}{\sqrt{w}}(1-j) \tag{1.10}$$

The impedance of serially connected elements is acquired by summing the impedance of each element. Therefore, the series impedance of charge transfer resistance and Warburg impedance

from Figure 1.9 is calculated by adding them up. Based on the parallel impedance equation, the equivalent impedance of charge transfer resistance, Warburg impedance, and EDL capacitance are calculated using the following equations:

$$Z_{parallel} = \frac{Z_1 Z_2}{Z_1 + Z_2} = \frac{R_{ct} + Z_W}{1 + jwC_{dl}(R_{ct} + Z_W)} = \frac{R_{ct} + \frac{\sigma}{\sqrt{w}}(1-j)}{1 + jwC_{dl}(R_{ct} + \frac{\sigma}{\sqrt{w}}(1-j))} \tag{1.11}$$

$$= \frac{R_{ct} + \frac{\sigma}{\sqrt{w}} - j[wC_{dl}(R_{ct} + \frac{\sigma}{\sqrt{w}})^2 + \frac{\sigma}{\sqrt{w}}(1 + \sqrt{w}C_{dl}\sigma)]}{(1 + \sqrt{w}C_{dl}\sigma)^2 + (wC_{dl}R_{ct} + \sqrt{w}C_{dl}\sigma)^2} \tag{1.12}$$

Based on the Equation 1.9, the total equivalent impedance of Randles circuit is purely an addition of solution resistance and parallel impedance. This complex form of the total equivalent impedance is further dissembled into real and imaginary part of the impedance as shown in Equation 1.0-11. Then the phase angle can be calculated by simply taking the ratio of imaginary part and real part.

$$Z_{total} = R_s + \frac{R_{ct} + \frac{\sigma}{\sqrt{w}} - j[wC_{dl}(R_{ct} + \frac{\sigma}{\sqrt{w}})^2 + \frac{\sigma}{\sqrt{w}}(1 + \sqrt{w}C_{dl}\sigma)]}{(1 + \sqrt{w}C_{dl}\sigma)^2 + (wC_{dl}R_{ct} + \sqrt{w}C_{dl}\sigma)^2} \tag{1.13}$$

$$Z_{Re} = R_s + \frac{R_{ct} + \frac{\sigma}{\sqrt{w}}}{(1 + \sqrt{w}C_{dl}\sigma)^2 + (wC_{dl}R_{ct} + \sqrt{w}C_{dl}\sigma)^2} \tag{1.14}$$

$$Z_{Im} = \frac{-j[wC_{dl}(R_{ct} + \frac{\sigma}{\sqrt{w}})^2 + \frac{\sigma}{\sqrt{w}}(1 + \sqrt{w}C_{dl}\sigma)]}{(1 + \sqrt{w}C_{dl}\sigma)^2 + (wC_{dl}R_{ct} + \sqrt{w}C_{dl}\sigma)^2} \tag{1.15}$$

To show an example Bode plot of Randles circuit, parameter values are selected and plotted over a frequency range from 0 Hz to 100 kHz. The Warburg coefficient is assumed to be 150 $\Omega\ sec^{-0.5}$

which implies condition with typical diffusion coefficient of 1.6 x 10^{-5} $\frac{cm^2}{s}$ at bulk concentration 100 uM. Other parameters are: $R_s = 20\ \Omega$, $R_{ct} = 200\ \Omega$, and $C_{dl} = 20$ uF.

As Figure 1.12 illustrates, Randles model can elucidate the effect of bulk media and electrode-electrolyte interface. It is observed that diffusion process dominates the Randles system at a very low frequency (0 to 10 Hz) and Faradaic process at a frequency between 10 Hz and 100 Hz. The effect of solution resistance becomes predominant at a frequency of 100 Hz.

Randles circuit can be further expanded to understand various behaviors of electrochemical systems. However, it is important to note that a more complex EC model does not necessarily lead to higher accuracy in describing the system [1]. This thesis adopts Randles EC model in later chapters due to its simplicity and comprehensiveness.

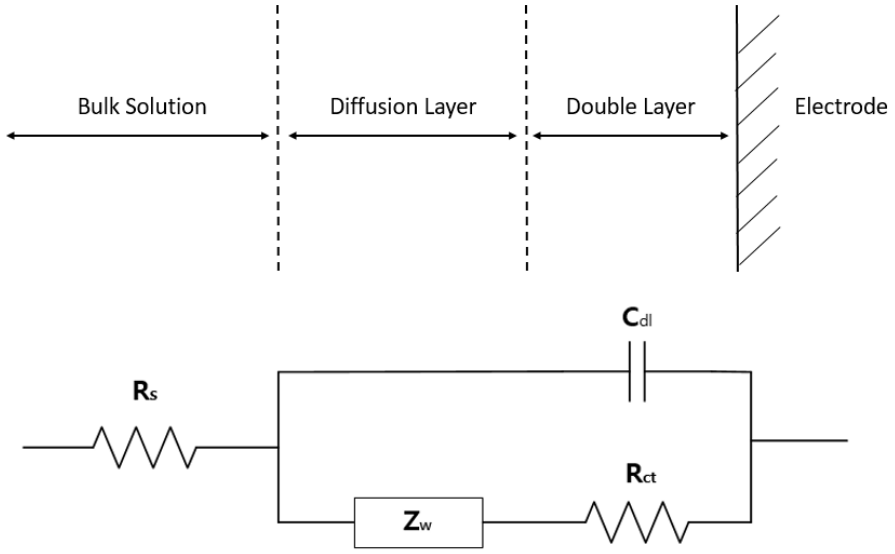

Figure 1.11: Randles equivalent circuit model. Solution resistance represents bulk solution, Warburg element represents diffusion layer, and double layer capacitance as well as charge transfer resistance represent electrical double layer [5, 9].

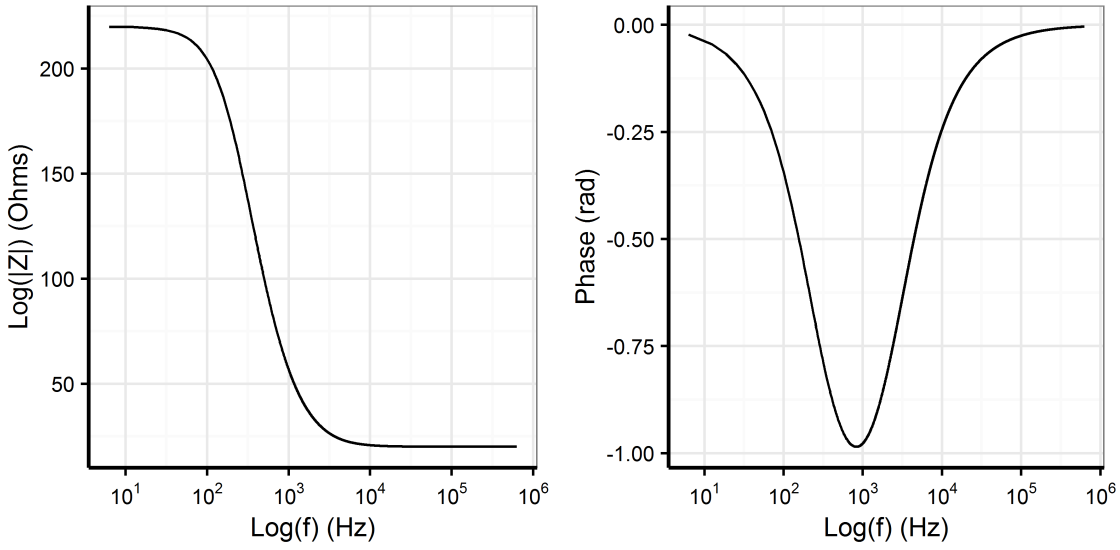

Figure 1.12: A Bode diagram for an example Randles circuit.

1.3 The effect of electrode polarization on the impedance data

Electrical impedance measurements are typically done with two electrodes where they inject current and sense voltage at once. During two electrodes measurements, electrode polarization (EP) occurs due to the induced polarization potential between the electrode and the sample. As a result, EP adds unwanted impedance to the sample impedance. EP impedance involves with both polarization resistance and polarization capacitance. Accordingly, EP becomes severely adverse at a frequency region between 0.1 Hz and 100 kHz where both the effect from capacitive and resistive impedance appear to be very significant [17, 18]. The problem of EP becomes more predominant when the impedance of sample is lower than the impedance of EP. To demonstrate its impact, Mirtaheri [19] reported EP impedance of silver, aluminum, platinum, and the gold electrode in NaCl aqueous solutions. According to their results, the value of polarization capacitance and polarization resistance were measured to be $10uF$ and $1M\Omega$ at 0.01 Hz. At 100 Hz,their values were measured to be $1uF$ and $1k\Omega$ respectively which are still very dominant. Therefore, the effect of EP is extremely significant at a low frequency range.

Schwan proposes several possible solutions to eliminate EP during impedance measurement so that EIS can properly investigate interfacial phenomena [17,18,20]. Among many solutions, Schwan suggests to employ four-electrode technique and elaborates its methodology [20]. As Figure 1.13 depicts, this method uses a pair of current electrodes and voltage electrodes separately. Because this setup does not allow current to pass through voltage electrodes, the total impedance measured by voltage electrodes is independent of polarization impedance by the current.

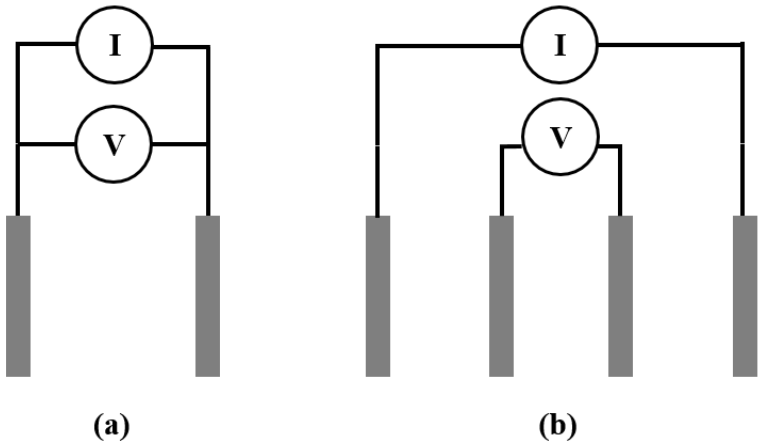

Figure 1.13: Illustrations of (a) two and (b) four electrode configuration.

In the previous study, Chang compared two and four-electrode measurements techniques for blood impedance to validate the usefulness of four-electrode technique [21]. He identifies that EP adversely affects the low frequency data (100 Hz up to 20 kHz) with two electrodes measurements. But he reports that EP effect was eliminated with four-electrode measurements technique at a low frequency range. Based on the result, Chang concluded that four-electrode technique could harness EIS properly without experiencing the EP effect [21].

There are several recommended implementations for a four-electrodes setup. First, it is advised to implement differential input amplifier at voltage electrodes to increase the accuracy of the data [20, 22, 23]. For the best accuracy, input differential amplifier must have the very high input impedance (TΩ) and high common mode rejection ratio (CMRR) to eliminate the effect of EP. In addition, Moron [22] reports that utilization of ideal polarized electrode (gold or platinum) can also reduce EP impedance significantly. Therefore, the four-electrode measurements technique and gold electrode are to be implemented in sensor design in order to minimize the effect of EP while maximizing the potential of EIS.

1.4 References

[1] E. Barsoukov and J. R. Macdonald, *Impedance spectroscopy: theory, experiment, and applications, 2nd edition.* NJ: Wiley, 2005.

[2] O. Panke et al., "Impedance spectroscopy and biosensing," *Adv. Biochem. Eng. Biotechnol*, vol. 109, pp. 195–237, 2013.

[3] I. D. Raistrick, "Application of impedance spectroscopy to materials science," *Annual Review of Material Science*, vol. 16, pp. 343–370, 1986.

[4] F. Lisdat and D. Schafer, "The use of electrochemical impedance spectroscopy for biosensing," *Annalytical and Bioanalytical Chemistry*, vol. 391, pp. 1555–1567, 2008.

[5] V. F. Lvovich, *Impedance spectroscopy: applications to electrochemical and dielectric phenomena.* NJ: Wiley, 2012.

[6] E. P. Randviir et al., "Electrochemical impedance spectroscopy: an overview of bioanalytical applications," *Analytical Methods*, vol. 5, pp. 1098–1115, 2013.

[7] J. R. Macdonald, "Impedance spectroscopy," *Annals of Biomedical Enginerring*, vol. 20, pp. 289–305, 1992.

[8] A. Lasia, *Electrochemical Impedance Spectroscopy and its Applications.* NY: Springer, 2014.

[9] B. Chang and S. Park, "Electrochemical impedance spectroscopy," *Annual Review of Analytical Chemistry*, vol. 3, pp. 207–229, 2010.

[10] "Basics of electrochemical impedance spectroscopy," 2016. [Online]. Available: http://www.gamry.com/application-notes/EIS/basics-of-electrochemical-impedance-spectroscopy

[11] P. Kurzeweil and H. J. Fischle, "A new monitoring method for electrochemical aggregates by impedance spectroscopy," *Journal of Power Sources*, vol. 127, pp. 331–340, 2004.

[12] S. Varma and C. K. Mitra, "Low frequency impedance studies on covalently modified glassy carbon paste," *Electroanalysis*, vol. 14, no. 22, pp. 1587–1595, Feb. 2002.

[13] S. Varma and C. K. Mitra, "Ac impedance characterization of highly resistive media using four-electrode electrochemical cells," *ECS Transactions*, vol. 25, no. 32, pp. 1–25, 2010.

[14] P. Vanysek, "Introduction to impedance," M.S. thesis, Univ. of Calgari, Canada, 1994.

[15] D. V. Ribeiro, C. A. C. Souza, and J. C. C. Abrantes, "Use of electrochemical impedance spectroscopy (eis) to monitoring the corrosion of reinforced concrete," *Revista IBRACON de Estruturas e Materiais*, vol. 8, no. 4, pp. 529–546, Aug. 2015.

[16] S. Park and J. Yoo, "Electrochemical impedance spectroscopy for better electrochemical measurements," *Analytical Chemistry*, vol. 75, no. 21, pp. 451–461, Nov. 2003.

[17] H. P. Schwan, "Alternating current electrode polarization," *BioPhysik*, vol. 3, pp. 181–201, May 1966.

[18] H. P. Schwan, "Electrode polarization impedance and measurements in biological materials," *Annals of the New York Academy of Sciences*, vol. 148, pp. 191–209, 1968.

[19] P. Mirtaheri, S. Grimnes, and O. G. Martinsen, "Electrode polarization impedance in weak nacl aqueous solutions," *IEEE Transactions on Biomedical Engineering*, vol. 52, no. 12, pp. 2093–2099, Dec. 2005.

[20] H. P. Schwan, "Four-electrode null techniques for impedance measurement with high resolution," *The Review of Scientific Instruments*, vol. 39, no. 4, Apr. 1968.

[21] Z. Chang, G. A. M. Pop, and G. C. M. Meijer, "A comparison of two- and four-electrode techniques to characterize blood impedance for the frequency range of 100 hz to 100 mhz," *IEEE Transactions on Biomedical Engineering*, vol. 55, no. 3, pp. 1240–1247, Mar. 2008.

[22] Z. Moron, "Considerations on the accuracy of measurements of electrical conductivity of liquids," presented at the XVIII IMEKO World Congress, 2006.

[23] D. Pelc, S. Marion, and M. Basletic, "Four-contact impedance spectroscopy of conductive liquid samples," *The Review of Scientific Instruments*, vol. 82, no. 7, pp. 073 907–073 907–5, 2011.

Chapter 2

System Development

2.1 Abstract

This chapter describes a novel system design for a low-cost, portable, and wireless electrical impedance spectroscope (EIS) that performs measurements using four electrodes. This chapter is separated into three parts. In the first part, the theory of electrical impedance spectroscopy is briefly reviewed and the high precision impedance measurement system-on-chip, AD5933, is introduced. The design criteria of the proposed sensor system are listed as well.

The second part details the hardware and the software design. In the hardware design section, a comparison of three open-source microcontrollers and a comprehensive overview of the developed analog front-end are explained. In addition, a impedance calculation process and a system calibration procedure are described to help understand how the developed impedance sensor obtains impedance measurements from the sample. In the following software design section, the explanation on how the user-friendly web application has been designed to operate the impedance spectroscope is presented.

In the third part of this chapter, the performance of the developed impedance sensor is evaluated through three different experiments. Firstly, a Randles circuit consisting of resistors and capacitors is analyzed, and the results demonstrate its high accuracy by comparing the measured value to the theoretical values. Secondly, the experiment of monitoring copper electrode corrosion in acidic media is conducted with custom made copper tape electrodes. The resulting data is fitted to the Randles equivalent circuit model, and three important electrochemical parameters are obtained. Lastly, the impedance sensor is used to detect diluted milk samples as milk adulteration is a big issue in many developing countries. The preliminary experiment of dilution detection showed that impedance spectroscope can detect diluted milk by investigating the change in the impedance

spectrum. These three experiments show that the proposed impedance spectroscope is capable of being employed for various applications.

2.2 Review of Electrical Impedance Spectroscopy

Electrical impedance spectroscopy (EIS) is a widely used analytical research technique in the field of chemistry, material science, and biology. This analytical technique allows the investigation of the dynamics of fixed or mobile charge carriers at the electrode-sample interface and is known to be especially useful in identifying electrical properties of solid materials, electrolytic mediums, and biological tissues [1, 2]. Numbers of studies have shown high potential of EIS due to its speed, simplicity of operation, and non-invasiveness. In theory, EIS measures electrical impedance by injecting a small amplitude alternating current (AC) excitation signal followed by measuring an AC response. The obtained impedance data is then plotted and further analyzed with the equivalent circuit model. An equivalent circuit model is very useful in analyzing the data because it simplifies complex electrochemical phenomena in simple electrical terms. Based on the model, EIS focuses on studying interfacial kinetics to provide information related to electrical double layer, charge transfer reaction, ionic contents, and diffusion mechanisims of analytes.

Recent advancement in electronics and wireless communication technology have led the trend in developing wireless and portable smart sensors as the US market is predicted to reach $58 billion by the year 2022 [3]. Unlike traditional sensors, smart sensors are capable of collecting, processing, transmitting, and displaying the data to users [4]. Utilization of these smart sensors range from biomedical [5], environmental [6, 7], to agricultural applications [8–10]. On top of physical information (e.g. temperature, humidity, pressure, and light intensity) that sensors can provide, implementation of EIS technique extends the measurement capability of the sensor by allowing the investigation of electrochemical systems. Therefore, we can benefit from developing a low-cost, portable EIS which can be used for a multitude of applications. In this study, a commercialized precision impedance measurement chip called the AD5933 is used to design a low-cost, portable, and wireless EIS. The detailed explanation of the AD5933 is presented in the following section.

2.3 AD5933 Opportunity

The AD5933 is the first commercially available high precision impedance measurement system-on-chips (SoC). It is equipped with an on-board frequency generator and digital-signal-processor (DSP) engine for the calculation of discrete Fourier transform (DFT), and a 12-bit, 1 MSPS (millions of samples per second) analog-to-digital converter (ADC) [11]. The measurement process of the AD5933 can be separated into three steps. Initially, the AD5933 generates the sinusoidal excitation voltage signal at specific frequencies. This excitation signal is injected from one electrode into the sample and the current is measured at the other electrode by a current-voltage (I-V) converter. Followed by Ohm's law relationship, the unknown impedance is calculated by taking a ratio of the voltage over the current. An onboard DSP engine automatically performs DFT on measured impedance and provides a real and an imaginary part of impedance as a result. This result is temporarily stored in a memory of the AD5933 and can be transferred to the microcontroller through Inter-Integrated Circuit (I^2C) communication protocol.

EIS data is collected over a particular frequency range. Since different regions of the frequency spectrum are related to different electrochemical information, the sweep frequency range has to be carefully considered. As Kurzweil points out, a low to intermediate frequency region (mHz to kHz) represents the electrode-sample interface reaction and diffusion influence, while a high frequency region (MHz) pertains to the property of solutions [12]. According to the AD5933 specification sheet, a range of frequency is limited from 1 kHz to 100 kHz [11]. However, the lower limit can be adjusted down to 10 Hz by employing an external clock [11], and the upper limit can be adjusted up to 500 kHz by reprogramming this chip [13]. Since diffusion effect is normally detected at a very low frequency (10 mHz), it may be difficult to obtain information related to diffusion over this frequency range using the AD5933. In spite of lower frequency limit, the frequency range from 10 Hz to 100 kHz is appropriate to identify other key information related to the electrode-sample interface. Therefore, the frequency range of the AD5933 is adequate to operate EIS technique.

The AD5933 has several benefits that make it an attractive solution for developing a low cost, portable EIS. Foremost, the AD5933 is a tiny and inexpensive chip which includes the most of the necessary components to operate EIS technique. To do this, instruments such as a function generator, an ADC, and a current sensing amplifier are required [14, 15]. The AD5933 contains

an on-board frequency generator, a DSP engine, and an ADC which satisfy the requirement of EIS operation. Besides, the AD5933 requires a single power supply ranging from +2.7V to +5.5V, which can be easily satisfied by using commercialized batteries. Lastly, the AD5933 is designed to be controlled by a master device or a microcontroller via I^2C communication protocol. In recent years, many single-board microcontrollers were become available on the market. These palm-sized single-board microcontrollers such as Arduino, BeagleBone Black, and Raspberry Pi are highly viable and robust [16–18]. They can easily interface various SoCs and control them with few lines of code. Consequently, these benefits make the AD5933 chip an attractive solution for developing a portable impedance sensor by reducing the overall cost and miniaturizing the size of EIS.

Nevertheless, there are limitations pertaining to the AD5933. First, the excitation voltage signal from the AD5933 includes a positive direct current (DC) bias [19–21]. The existence of this DC bias may be perilous for samples because it can modify the inherent property of samples by causing electrochemical reactions at the electrode-sample interface [19]. Introduced DC current is also very unsafe especially for biological or living samples [20]. Furthermore, the AD5933 is originally designed to operate with two electrodes. As Schwan identifies, measurements with two electrodes can add the unwanted electrode polarization (EP) impedance to the result impedance at a low frequency region up to 100 kHz [22, 23]. Accordingly, these issues must be mitigated or resolved during the sensor design for more accurate measurements.

By taking into account both advantages and disadvantages, numerous research endeavors were performed to devise a low-cost, portable EIS using the AD 5933 for various applications, e.g. healthcare [24–26], and environmental monitoring [27,28]. As these studies have shown, the AD5933 based impedance spectroscope can become more accurate and robust with meticulously designed external circuits to compensate drawbacks. Therefore, this study proposes a novel extension circuit design to eliminate its internal issues while attempting to make the system more robust.

2.4 Design Criteria

Currently, there are many commercialized impedance analyzers on the market. Although these instruments have high performances, they cost over $30,000 and are very cumbersome. These impedance analyzers are often difficult to handle without proper instructions and training. On

the other hand, portable impedance analyzers, such as LCR meters, are also available. These hand-held impedance analyzers cost about $200 which is 100 times cheaper than conventional instruments. Nevertheless, they allow measurements only at single or dual frequencies. This insufficient frequency spectrum of LCR meters can lose valuable electrochemical information. LCR meters also lack a visualization feature since they do not automatically generate graphs after measurements. Considering current trends of commercialized products, we aim to develop an electrical impedance spectroscope that is low-cost, portable, web-connected, and easy to use.

Firstly, there are good reasons to develop an inexpensive sensor. It is economically more viable than other commercial products. Because the cost of each sensor unit is low, it is feasible to deploy multiple sensor units at the same time and make use of them for various applications. In order to meet this criterion, the extension circuit was designed carefully to minimize the cost. The goal of this design is to make the total cost of sensor below $100. The total estimated cost is presented in the system construction section.

Fulfilling portability requirement is critical to facilitate field and point-of-care (POC) tests. Due to the relatively large size of conventional impedance analyzers, exploitation of EIS technique has been limited to laboratory environments. The application of portable LCR meters may be inadequate since the range of frequency is restricted. As many field tests using impedance spectroscope had been previously unavailable due to the size, reducing the overall size of the system can significantly promote its use for various field applications. In this study, the portability requirement has been satisfied by employing an open-source single board computer, the BeagleBone Black. This computer is a size of a credit card and can be powered by a +5V battery which is suitable for the development of a portable sensor. An extension sensor circuitry is desinged to be operated with the auxiliary input and output (I/O) pins of BeagleBone Black.

Conventional instruments lack data logging, and visualization features and users may have to log and visualize the data manually.To simplify the process of data logging and visualization, we designed our sensor system to be equipped with wireless capability. With current wireless technology, it is possible to log the data inside the microcontroller, while wirelessly connected smart devices display the result data. In this particular design, Wi-Fi is selected due to its robust security and fast data transfer speed compared to Bluetooth and Zigbee technology.

Lastly, operating commercial devices is often troublesome without reviewing details of the instrument manual. In an attempt to assist and promote the operation by non-experts, we aim to program the user-friendly application software that is easy to use and visualizes the result with minimal training. The application software is based on an open-source Javascript engine, the Node.js and incorporates libraries such as bonescript, I^2C,and D3. Bringing an open-source single board computer and open-source program libraries together, implementation and prototyping of a complete sensor system become easier and faster.

2.5 Hardware Design

2.5.1 Microcontroller selection

A single-board microcontroller refers to a computer that consists of a processor, memory, and programmable I/O pins. It can be designed to be connected to peripheral sensors and actuators, and automatically control them based on the implemented program. Due to their small size and configurability, they are commonly employed in developing or prototyping electronic devices. A lot of single-board microcontrollers are currently available on the market. Among them, the three most famous microcontrollers (i.e. Arduino Uno, Raspberry Pi 2, and BBB) are selected and their specifications are reviewed and compared. Although Raspberry Pi 3 and BBB Revision C are now available, Raspberry Pi 2 and BBB Revision B are reviewed due to the fact that newer boards were not commercialized during the early phase of this study. Table 2.1 demonstrates several key characteristics of each microcontroller.

	Arduino Uno [17]	Raspberry Pi 2 [18]	BeagleBone Black Rev.B [16]
Price	$24.95	$39.95	$45
Clock speed	16 MHz	900 MHz	1GHz
Number of Analog input pints	6	0	7
Number of Digital input pins	14	27	69
Onboard memory	32kB	SD card	2GB
GPU	No	Yes	Yes
Ethernet	No	Yes	Yes

Table 2.1: Comparison of three microcontrollers [16–18]

Arduino Uno is probably the most popular single-board microcontroller in the electronic market [17]. Arduino Uno is a great choice due to its low cost and high configurability. First of all, Arduino Uno costs only $24.95 which is very inexpensive compared to other microcontrollers. In addition, it runs at the clock speed of 16 MHz which is capable of collecting data at the maximum speed of 115200 Hz. Moreover, Arduino Uno provides both analog input pins and programmable digital I/O pins. This allows users to control machines via digital pins and read analog outputs from external sensors. Arduino Uno also provides +3.3V or +5V power supply pins which extend the choice of exeternally connectable electronics. Despite these advantages, Uno poses several limitations in developing a portable, wireless sensor system for this design. Since there is a restriction on the speed of the clock, systems can not process data at high speeds. It also does not have a graphic engine (GPU) and a large enough onboard memory to run the operating systems. Thus, while low-cost, reliable, and user-friendly Arduino Uno is an interesting solution for prototyping electronics, it lacks few features to be implemented in this study.

Another microcontroller called, Raspberry Pi, became available in 2012 [18]. It gained its own popularity quickly and undergone several modifications on the board design since then. This microcontroller has several advantages over Arduino Uno. First, it contains a 900 MHz clock that enables much faster sample rates during data acquisition process. Furthermore, it does not have fixed size of on-board memory and can be easily modified by inserting different size of SD card to Raspberry Pi. It also comes with a GPU chip, an Ethernet port, and USB ports which allow running operating systems to mimic features of modern computers. Notably, Raspberry Pi supports WiFi and Bluetooth connectivity through on-board USB ports. Nevertheless, Pi restrains employment of peripheral electronics because it does not have an ADC to process the analog data and this ADC has to be programmed properly. In order to receive analog data from peripheral electronics, it has to be used in conjunction with an additional ADC chip. In this study, Raspberry Pi is excluded from the choice to minimize efforts implementing an additional ADC to sample the analog signal from the AD5933.

BeagleBone Black (BBB) was launched by Texas Instruments in 2013 [16]. Similar to Raspberry Pi, BBB has been modified multiple times to be robust and versatile single-board microcontroller. BBB is designed to incorporate benefits of both Raspberry Pi and Arduino. First, it utilizes 1 GHz

clock in order to increase the overall speed of processing. 1 GHz is 100 times faster than Arduino Uno and 100 MHz faster compared to Raspberry Pi 2. In addition, BBB contains numbers of analog and digital I/O pins as well as ADC which empower broad applications with peripheral sensors or machines. Few of these pins can be configured to produce pulse width modulation (PWM) signal and they can be employed as external clocks to extend the frequency limit of the AD5933. At last, BBB can run operating systems with a 2 GB on-board memory and provide Wi-Fi and Bluetooth connectivity through a USB port. Wireless connectivity allows data transfer of both web application and measured data from a microcontroller to smart devices remotely. Therefore, in spite of the fact that BBB is the most expensive one among the three microcontrollers reviewed in this section, it is used to reduce the time of developing a low cost, portable smart impedance sensor.

2.5.2 Review on four electrodes AFE design for the AD5933

Typically electrical impedance spectroscope measures impedance with two electrodes. However, Schwan identifies an inherent problem with two electrodes measurements. According to his research, electrode polarization (EP) impedance will be added to the measured impedance value of samples [22, 23]. This added EP impedance significantly degrades the data quality especially at a low frequency region where the majority of important information about the electrode-sample interface is obtained [22,23,29]. In order to avoid this issue, Schwan recommends to implement four electrodes measurements technique [23], and several research have concluded that this technique is more reliable than two electrodes measurements at a low frequency range [30–32].

The EP impedance problem can be resolved by developing an extension circuitry that enables four electrodes measurements. In theory, four electrodes technique is implemented by separating current injecting electrodes and voltage measuring electrodes, then measures the response signal created by the unknown impedance [23]. There are two different approaches to implement four electrode measurements technique, called galvanostatic and potentiostatic [13, 19, 20, 33, 34]. First, galvanostatic method is based on implementing a symmetric current source. It fixes the current by injecting and receiving at the excitation stage then the voltage drop at two inner electrodes is measured. This design has been employed and demonstrated by Margo, Seaone, and Pliquett [19,

20, 33]. They have evaluated developed extension circuits with simple resistor-capacitor networks and deduced that four electrodes sensing successfully eliminated the effect of EP impedance.

As opposed to the galvanostatic method, the potentiostatic technique is based on the voltage feedback mechanism [34]. Rather than directly measuring the voltage drop, this approach holds the voltage between two inner electrodes constant. This measured voltage is then fed back to the inverting input of the injecting buffer amplifier. This forces this buffer amplifier to reapply the excitation signal that is a voltage drop created by samples, as a result, EP impedance caused by current flowing through electrodes is eliminated. Although both of these can accomplish four electrodes measurements technique, the potentiostatic method has not been employed in many studies compared to a galvanostatic method. Additionally, the existing potentiostatic design presented by Pliquett is somewhat intricate involving two AD5933 chips [34]. Therefore, we propose a novel and simple potentiostatic based four electrodes measurements AFE that is operated with BBB microcontroller.

2.5.3 Analog-front-end design for four electrodes measurements

After reviewing two different approaches to implementing four electrodes measurements technique, a novel and simple potentiostatic AFE is presented. The proposed AFE design can be divided into three stages; the AC coupling driving probe, the feedback stage, and the trans-impedance stage. Figure 2.1 describes the simplified diagram of the devised circuitry. Detailed demonstrations on the method of DC bias elimination and selection criteria for electrical compartments follows.

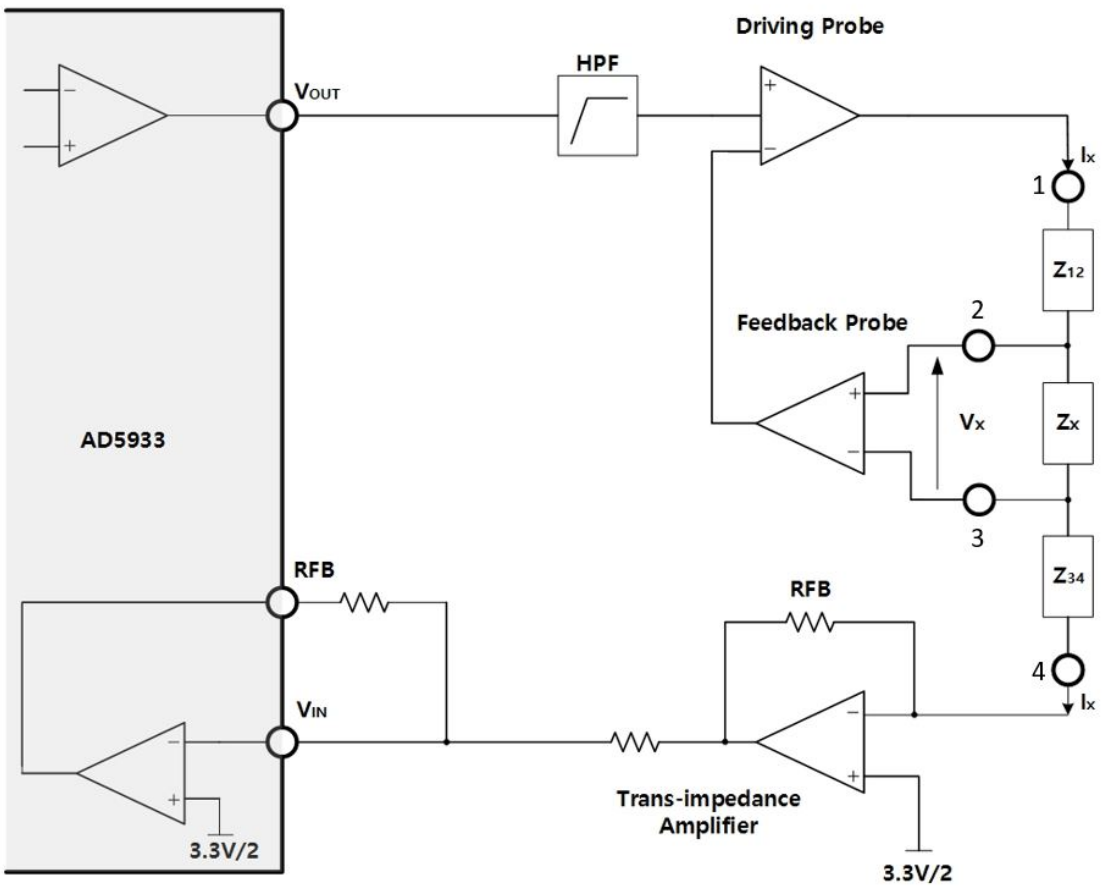

Figure 2.1: Simplified analog-front-end circuit diagram.

1. AC coupling and driving probe

A four electrodes measurements technique applies a known voltage and measures the conduction of sample. However, the DC bias voltage issue pertains to the output excitation signal of the AD5933 has to be conditioned properly before it passes through a buffer amplifier according to the specification sheet [11]. The AD5933 has four possible levels of the excitation voltage at the transmitting stage. When +3.3V power supply is used, the maximum excitation voltage of 1.98Vp-p creates the bias voltage of +1.48V at the transmitting side. On the other hand, the bias voltage

at the receiving side of the AD5933 is fixed at $\frac{V_{DD}}{2}$ which is +1.65V. This potential difference between the transmitting (+1.48V) and the receiving (+1.65V) stages polarizes the sample and leads to inaccuracies in the result [19, 21]. Therefore, a high pass filter to remove any DC signals and a pull-up resistor network to rebias at +1.65V are required before the excitation signal passes through a buffer amplifier.

In this design, a high pass filter is built by connecting a pull up resistor to the power supply voltage along with a capacitor to make the cut off frequency. Since the proposed design aims to utilize a PWM pin of BBB to broaden the sweep frequency range down to 20 Hz, the cut off frequency of a high pass filter should be lower than 20 Hz. Accordingly, a 0.1 uF capacitor and two 100 kΩ resistors are employed to make cut-off frequency at 7.96 Hz. In addition, a pull up resistor network helps the excitation signal to be rebiased at +1.65V which prevents polarization at the receiving stage by centering the signal at the same level all the time. This filtered and rebiased signal is inputted to the non-inverting side of this amplifier, while the inverting side is fed with the voltage drop caused by the sample to achieve the potentiostatic method of four electrodes measurements technique.

Although many commercialized operational amplifiers are suitable for this stage, several requirements have to be met for this particular design. It is suggested by the AD5933 specification that an op amp with very low output impedance, low bias current, low offset voltage, and high common mode rejection ratio (CMRR) should be used to obtain high accuracy impedance data [11]. Therefore, a quad, rail-to-rail input and output, single supply amplifier AD8608 is selected [35]. A quad version is used instead of a single version in order to reduce the layout space of a printed circuit board (PCB) because the feedback stage and the trans-impedance stage also employ this same amplifier. The AD8608 is operated by single supply from +2.7 V to +5.5V, hence +3.3V output pin from BBB is utilized to supply the power to this chip.

2. Voltage measuring feedback probe

A four electrodes measurements technique requires two inner probes to measure the voltage drop of the sample of interest. This is accomplished by implementing a differential amplifier or an instrumentation amplifier. There are a number of requirements for the voltage measuring feedback

amplifier including a high common-mode rejection ratio (CMRR), a high input impedance, and fast slew rate as demonstrated in previous studies. [30, 31, 36]. Because the unknown impedance can be small compared to the whole impedance, the effect of the common-mode voltage can be critical to the accuracy [19]. To reduce the common-mode voltage error, the amplifier should exhibit high CMRR over a wide range of frequency. In addition, the electrode-sample impedance created by the current flowing through metal electrodes can significantly affect the accuracy. This unwanted impedance is reduced by choosing an amplifier with a high input impedance above Tera-ohms. Extremely high input impedance minimizes the amount of current flow at the inner electrodes [30].

In this study, the instrumentation amplifier, the AD8220, is selected for several reasons [37]. First, the AD8220 operates with either a single power supply (+4.5V to +36V) or a dual supply (2.25V to 18V). Therefore, +5V pin of BBB is used as a power source for this chip. Second, the AD8220 maintains the CMRR of 60 dB up to 100 kHz. This indicates that the common-mode voltage error is at least 1000 times smaller than the differential signal of the samples at 100 kHz. In addition, the AD8220 has a very high input impedance of 10 TΩ which satisfies the criteria discussed earlier. Lastly, the AD8220 has sufficiently fast slew rate to prevent the feedback signal to the driving amplifier to be delayed. The AD8220 has the slew rate of $2\frac{V}{us}$ which is faster than $1.2\frac{V}{us}$ of the driving amplifier. Therefore, the AD8220 is appropriate as an instrumentation amplifier to deliver the feedback signal to the inverting input of the driving amplifier.

Note that, the differential voltage signal measured by the AD8220 is supplied by a 5V power source unlike other components that are supplied by +3.3V. As a result, the voltage drop measured at this stage is centered at +2.5V instead of +1.65V. This difference in bias voltages degrades the quality of the data, thus the feedback stage also has to be centered at +1.65V. This issue is resolved by connecting the second AD8608 biased at +1.65V to the reference pin of the AD8220.

3. Trans-impedance amplifier

When the driving stage injects the current signal, the current generates the voltage drop at the inner electrodes, then this current returns to the fourth electrode. This current can be directly received into the AD5933 where it is converted into voltage by the feedback resistor. Nevertheless, the direct return path can limit the dynamic range of device as the AD5933 requires a close match between

the unknown impedance and the feedback resistor [11]. Thus, the proposed design employs a trans-impedance amplifier with adjustable gain setting resistors in order to increase the dynamic range of measurements. The gain of the amplifier can be manually modifiedusing a jumper connected to one of the gain setting feedback resistors. In this design, five resistors, 100 Ω, 500 Ω, 2 kΩ, 10 kΩ, and 20 kΩ, are used. These gain resistors allow the impedance spectroscope to measure a broad range of the unknown impedances.

The current signal of the trans-impedance amplifier is also biased at +1.65V to make signals at all of the stages centered at the same voltage level. This signal is then processed by the AD5933 internally to produce a real and imaginary part of the measured impedance. As the application note of the AD5933 demonstrates, there are several standards for choosing the proper trans-impedance amplifier [21]. It should have a high bandwidth, a low noise input current/voltage, a low offset voltage/bias current, and a high CMRR to minimize the noise effect on the data. As the review of the AD8608 in the driving amplifier stage demonstrated earlier, these requirements are satisfied as well, therefore the third AD8608 is used at this stage [35].A complete circuit schematic for the AFE is created using EagleCAD software and it is presented in Figure 2.3.

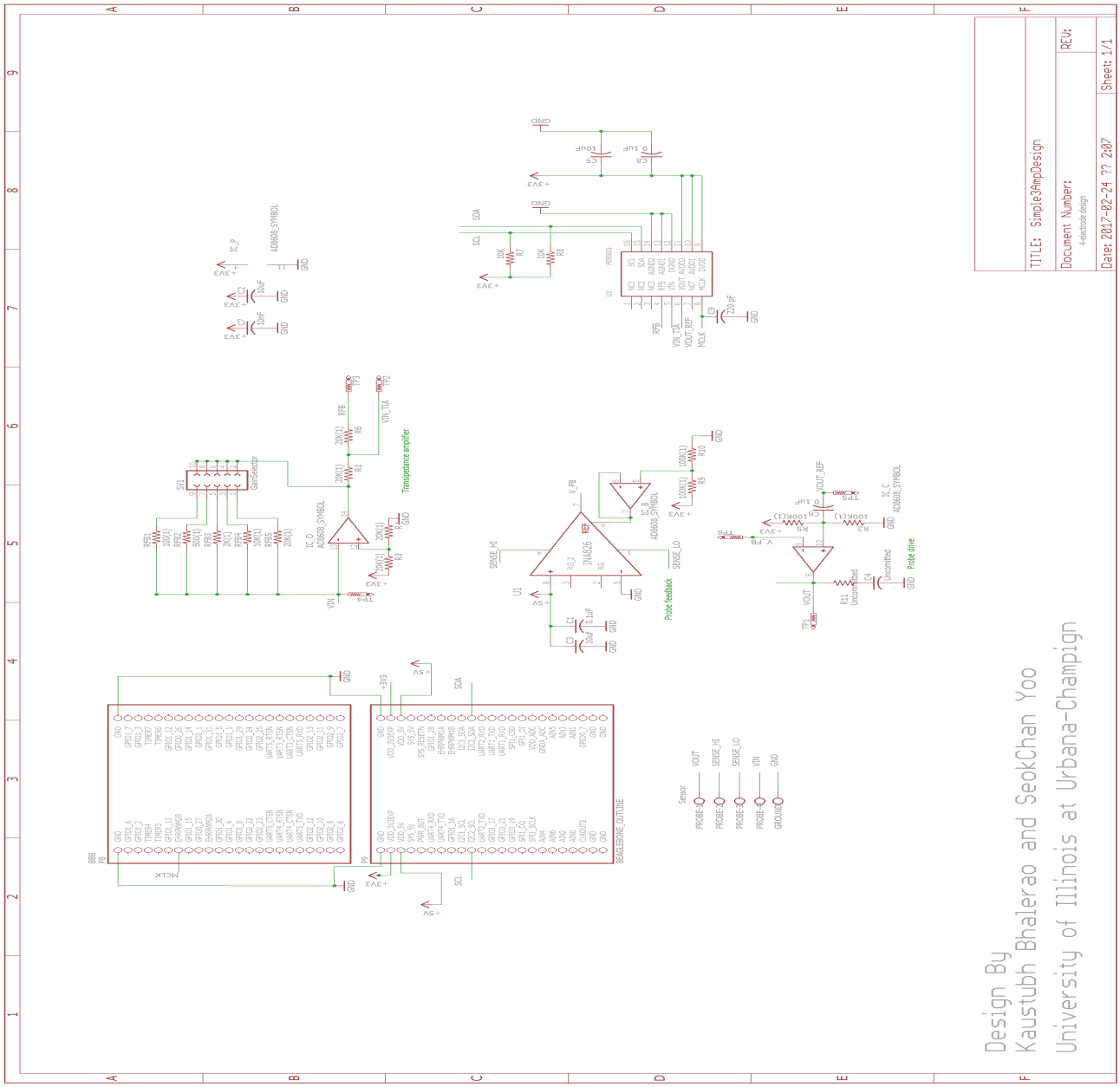

Figure 2.2: Analog-front-end circuit schematic.

2.5.4 Impedance calculation and calibration theory

It is important to understand how the unknown impedance is measured with the developed AFE, therefore a brief description of the impedance calculation process is described. First of all, the output excitation voltage (V_p) is filtered with a high pass filter and rebiased at one half of the supply voltage ($\frac{V_{DD}}{2}$). Then the resultant voltage at the output of the driving amplifier is $V_p + \frac{V_{DD}}{2}$. After correctly compensating for the EP effect by feedbacking the voltage drop measured at two inner electrodes to the driving amplifier, the compensated current signal (I_x) generated by the unknown impedance $Z_{unknown}$ is biased at $\frac{V_{DD}}{2}$, therefore I_x can be expreed by the following Equation 2.1.

$$I_x = \frac{\frac{V_{DD}}{2} + V_p - \frac{V_{DD}}{2}}{Z_{unknown}} = \frac{V_p}{Z_{unknown}} \tag{2.1}$$

The current flowing through the gain setting resistor (R_{FB}) is the same as Ix, thus the output voltage (V_T) at the trans-impedance amplifier can be calculated using the Equation 2.2.

$$V_T = \frac{V_{DD}}{2} - I_x R_{FB} \tag{2.2}$$

At the receiving stage of the programmable gain (PGA) amplifier of the AD5933, the non-inverting side is biased at $\frac{V_{DD}}{2}$ and the inverting side is fed with V_T that is connected to two 20 kΩ resistors. The output voltage at the PGA amplifier (V_{TIA}) is calculated with the Equation 2.3.

$$V_{TIA} = \frac{V_{DD}}{2} + (\frac{V_p}{Z_{unknown}})R_{FB} - \frac{V_{DD}}{2} = (\frac{V_p}{Z_{unknown}})R_{FB} \tag{2.3}$$

As shown above calculations, the impedance measurement is governed by the output excitation voltage, the gain setting feedback resistor, and the unknown impedance. Based on the Equation 2.3 , it is clear that one needs to carefully choose the excitation voltage and the value of a feedback resistor to avoid signal saturation at all stages. The AD5933 has to be calibrated with a known impedance before actual measurements. According to the specification sheet, the gain factor is calculated during the calibration process using known value of a resistor [11]. The accuracy of measured impedance is greatly dependent on how large the unknown impedance range deviates

from the value of a calibration resistor [21]. Therefore, choosing an appropriate value of the calibration resistor that is close to the value of the unknown impedance will lead to more accurate measurements. During the calibration process, the gain factor of the system is calculated with Equation 2.4 [11].

$$GainFactor = V_p \times \frac{R_{FB}}{Z_{unknown}} \times PGAGain \tag{2.4}$$

It is noted that the receiving stage must operate below the power supply with the calculated gain factor. Otherwise, the signal saturates, and the measured data will be inaccurate. As shown in equations above, there are four variables that need to be thoroughly considered. They are the output excitation voltage range, PGA gain, and the value of the gain setting resistor and the calibration resistor. If one of these is too large, then the voltage presented to the ADC input would be saturated. After the gain factor is calculated during the calibration process using the known impedance value, the sample impedance is determined by multiplication of the gain factor and the measured impedance. The best value of calibration resistor is suggested to be one-third of a sum of the maximum and the minmum expected value of the unknown impedance [11].

The impedance spectroscope was tested to measure different values of a resistor to show the dynamic range of the device when it is calibrated using a 100 Ω feedback resistor and a 100 Ω calibration resistor. The tested frequency range was from 1 kHz to 100 kHz. Table **??** presents mean, standard deviation, and coefficient of variation for seven different resistor values measured. As described in this table, mean value and standard deviation denote that measurement up to 470 Ω is very precise. In addition, coefficient of variation is less than 2 % indicating that very small variations exist over a full sweep frequency range. Nevertheless, as the value of measured resistance increases, mean value is far from the actual value, plus standard deviation and coefficient of variation are extremely large, showing 32.165 % coefficient of variation at 10 $k\Omega$ measurement. Therefore, this suggests that the impedance spectroscope can produce very accurate results up to about four times the value of a calibration resistor due to the potentiostatic design.

Measured Resistance (Ω)	Mean	Standard Deviation	Coefficient of Variation
100	99.98	0.1087	0.1087
200	200.32	1.0476	0.5230
470	460.76	8.9367	1.9396
940	895.51	40.716	4.5467
2200	1956.56	209.71	10.718
4400	3645.10	733.93	20.135
10000	6634.83	2134.10	32.165

Table 2.2: 100 Ω feedback resistor and 100 Ω calibration resistor.

2.5.5 PCB layout

The PCB layout of the designed AFE is created using EagleCAD software and illustrated in Figure 2.3. As shown in this figure, PCB is designed to be the same dimension of BBB in order to make the entire system to be more compact. In order to protect the important voltage drop signal caused at two inner electrodes, a guard ring was placed around the connectors and the instrumentation amplifier. During the PCB construction, few capacitors were added as debugging purposes. Firstly, we have discovered that the actual slew rate of the instrumentation amplifier (AD 8220) is not fast enough to follow the slew rate of the buffer amplifier (AD 8608) causing errors at the measurement. As a solution, we have added a 100 pF capacitor in between the feedback line of the instrumentation amplifier and the output voltage line of the buffer amplifier to slow down the slew rate of the buffer amplifier. This technique is known as dominant-pole compensation. Plus, there was a noise found at PWM pin of BBB, and this noise was eliminated by adding a 220 pF capacitor. After fixing these issues, the AFE was worked properly as designed.

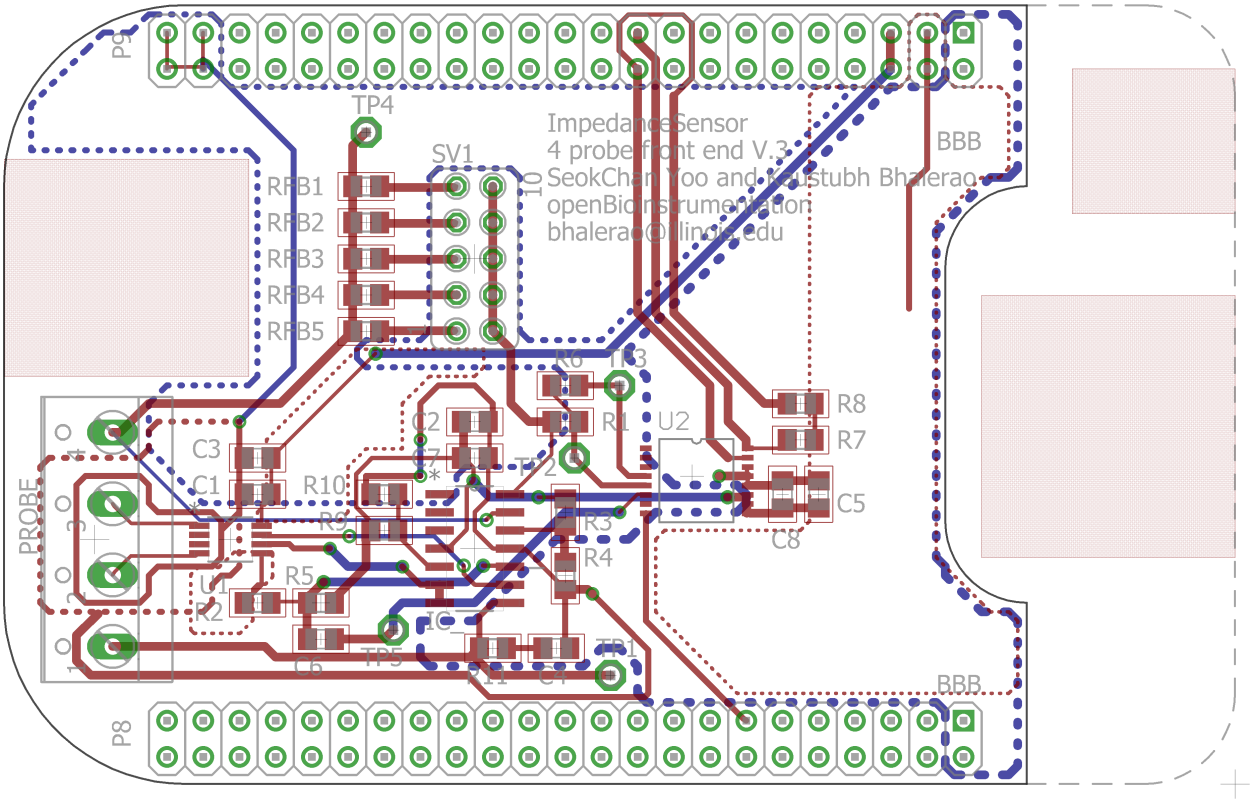

Figure 2.3: PCB layout of Analog-front-end.

2.6 Software Design

2.6.1 Overview of software stack

In this study, a novel web application is developed in order to allow easier interaction between users and the sensor. The developed software can be divided into three blocks; BeagleBone core, server side program, and client side program. Figure 2.4 illustrates the simplified stack diagram of the developed software. The BeagleBone core consists of Linux operating system (OS), Javascript engine, and other necessary Javascript libraries. This core allows BeagleBone core to control the AD5933 chip and retrieve the information from it. The server side program and the client side program form the functionality and appearance of the web application that enable users to communicate and interact with the impedance spectroscope.

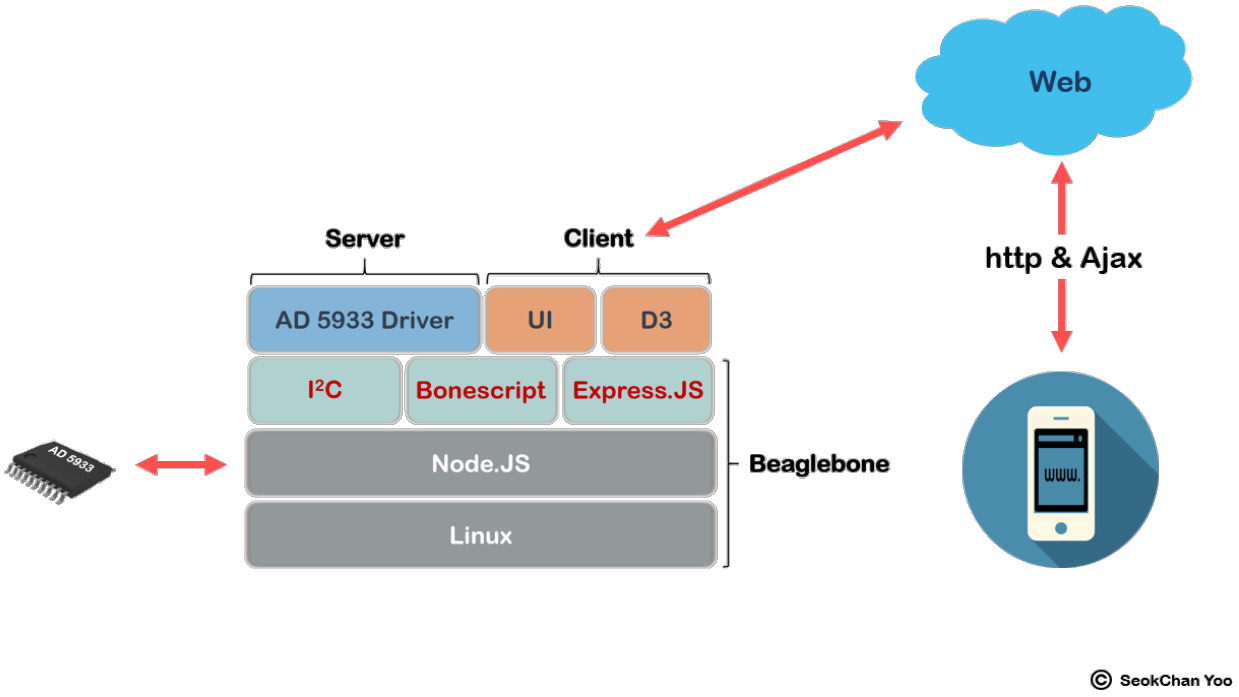

Figure 2.4: Simplified software stack diagram.

The construction of BeagleBone core begins with installing an OS. According to the website of BBB, it is capable of running several different operating systems such as Angstrom Linux, Debian Linux, Ubuntu Linux, and Android [16]. Instead of the default Angstrom Linux, Debian Linux is installed due to its larger supporting community and stability [38]. There are several options of using different programming languages to develop the web-application. Among them, JavaScript engine called Node.js is selected. Node.js is a JavaScript runtime built on the Chrome browser's JavaScript engine, and it uses event-driven, non-blocking input/output model that makes application lightweight and efficient [39]. In addition, Node.js is supported by various libraries which foster easier and faster development of web applications. Therefore, Node.js is considered to be an adequate choice for the web application.

For a BBB to communicate with the AFE and open up a web server for the application, three sets of Javascript libraries are required. First, BoneScript library is downloaded. BoneScript is optimized for BBB and provides several functions for interacting with BBB. Both digital and analog I/O pins of BBB can be easily controlled with BoneScript library. This helps quick development of various electronic systems. Second, I^2C library is installed. I^2C library allows microcontroller to communicate with the system-on-chip devices which are connected via I^2C protocol. The AD5933 is connected to I^2C bus as a slave device under control of a BBB microcontroller, thus I^2C library enables BBB to read and write register addresses of the AD5933. Lastly, Express.js is installed to generate the web server. Express is a light-weighted framework of Node.js which helps programmer to organize web applications without difficulty [40]. Upon establishing BeagleBone core, the server side (back-end) and the client side (front-end) software are programmed to construct the actual web application.

2.6.2 The AD5933 Driver - Back-end program

The AD5933 driver program is synthesized based on the frequency sweep algorithm of the AD5933. Thus it is important to understand the process of frequency sweep [11]. First, when a user requests a web page via the Hypertext Transfer Protocol (HTTP), the driver code allocates register map of the AD5933 and programs frequency sweep parameters into registers. These frequency sweep parameters include start frequency, the number of increments, and frequency increment. After

register configuration, the AD5933 is set into standby mode and waits for the user command. Upon user's request to start frequency sweep, the driver program writes start frequency sweep command. At this stage, the AD5933 begins measuring impedance for designated frequency range and calls for two polls. The first poll verifies whether DFT conversion has been applied to the data or not, and the second poll checks if frequency sweep has been completed. This process continues until the last frequency sweep. After each measurement, the driver code writes command to power down the AD5933 to save the power consumption. Beside of basic configurations, the back-end software includes a function to assign an external clock with a PWM pin provided by BBB to measure the impedance at a range from 20 Hz to 1 kHz. The PWM pin is configured to produce 100 kHz for a low frequency range (20 Hz to 600 Hz), and 1 MHz for a medium frequency range (600 Hz to 6 kHz) which are identified to be the best as stated by the application note [21]. In addition, the back-end software automatically fetches gain factors from the calibration data and multipies them to the measured impedance values to produce correct results.

2.6.3 UI and D3 - Front-end program

User interface (UI) and D3 are programmed for visualization of the front-end program. The design of user interface is based on the Bootstrap layout which is the most popular web framework for developing responsive and mobile friendly application [41]. There are several key features in the front-end program. First, frequency sweep functions are coded and linked to buttons declared in the layout. Upon clicking action, they verify whether the user has typed a file name for the measurement. After each measurement, the measured impedance data are converted into JSON file format and saved on the SD card of BBB for further processing. Second, users can calibrate the system by typing the value of calibration resistor and click the calibrate button. This will run the calibration script and restart the web application at the end of the calibration process. Moreover, the front-end visualizes the measured impedance data into the Bode plot format in real time using the D3 library. A light-weight, fast, and interactive D3 library is used to generate reusable line charts with the interactive mouseover tooltips and the legend [42]. Lastly, users can also look up every data that are saved on the SD card. When users click the data load button, the front-end software will show names of all the data. Upon users click on any data and the replot button, the

second graph is generated automatically. With these simple layout and features, users can easily interact with the impedance spectroscope.

2.7 System Construction

A low-cost, portable, and wireless impedance analyzer system was constructed based on the proposed novel design. All electrical components for the AFE were purchased from Digikey, and Printed Circuit Board (PCB) was ordered from Oshpark where they offer very cheap and reliable PCB. Purchased components are hand-soldered onto the board in the laboratory. List of parts, and the price breakdown are presented in Table 2.3. As demonstrated in this table, the proposed design of impedance spectroscope costs below $100. Thereby, low-cost design criteria have been satisfied without a doubt. Circuit schematic and PCB design of AFE are published at Git repository for free.

The simplified system diagram of a complete system is shown in Figure 2.5. BBB is employed not only to control the AD5933 and the expansion shield but also to provide an external clock signal to the AD5933. Wi-Fi dongle is attached to BBB to provide wireless communication between smart devices and the sensor. The AD5933 is controlled by the I^2C communication protocol, and it collects the impedance data using the expansion shield which allows four electrodes measurements. The actual photo of the manufactured impedance analyzer system and the screenshot of the developed web application are described in Figure 2.6.

Parts name	*Number of parts used*	*Unit price ($)*
AD5933	1	20.27
AD8220	1	6.52
AD8608	1	4.34
Capacitors (0805 SMD, 5% tolerance)	10	~ 0.1
Resistors (0805 SMD, 1% tolerance)	16	~ 0.1
Screw terminal	1	0.89
PCB board	1	5
BeagleBone Black	1	45
Wifi Dongle	1	~ 9
Total cost		~ 94

Table 2.3: List of components and price break down

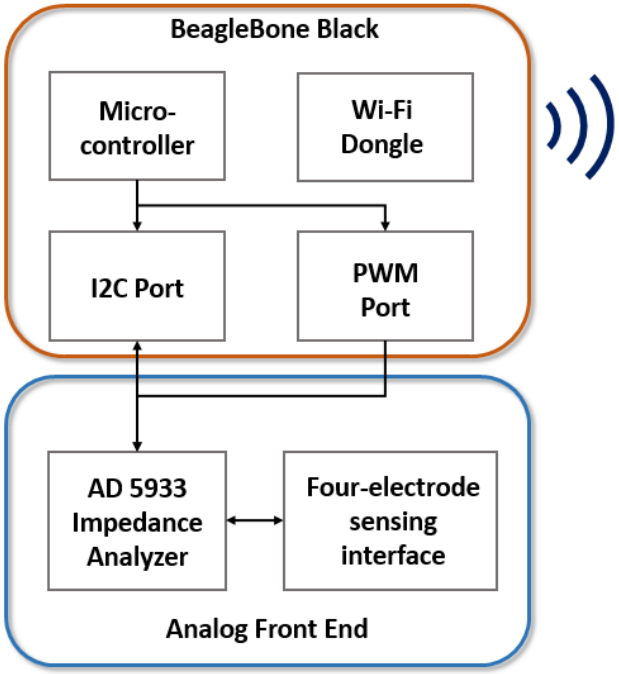

Figure 2.5: The simplified system diagram of the impedance spectrscope.

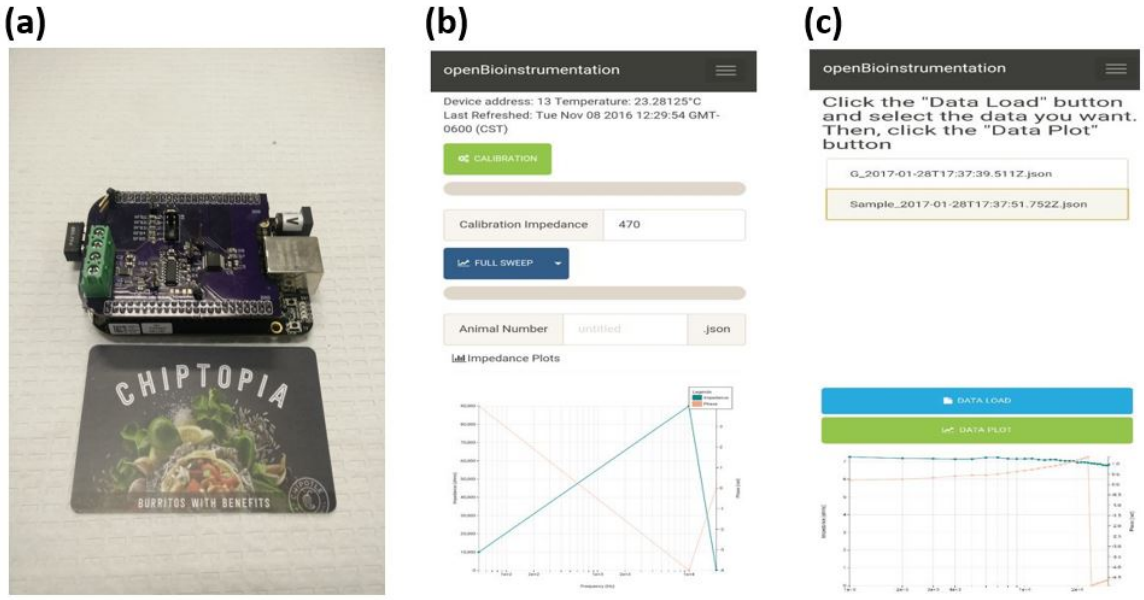

Figure 2.6: (a) The photo of the impedance spectroscope, and the screenshot of the software (b) top part with calibration button, sweep button, and the D3 line chart (c) bottom part with data load button and the second line chart.

2.8 Performance evaluation of the Impedance spectroscope

In this section, the performance of the developed impedance spectroscope was evaluated through three different experiments. Initially, the device was tested with Randles circuit using resistors and capacitors. The measured impedance data was plotted and fitted to theoretical values in order to validate the accuracy of the device. Secondly, the device was tested to monitor corrosion process of copper strip electrodes in acidic solution. During this experiment, the solution was continuously stirred with stir bar to minimize the effect of diffusion and the result data was fitted to Randles circuit model without the diffusion impedance. Lastly, the device was used to disseminate the diluted milk from the full-fat milk. In this experiment, full-fat milk was diluted with tap water and sodium chloride solution from 5 % to 80.63 %. As mentioned above, a stir bar was used to minimize the effect of diffusion. Result plots were generated to show the change of impedance over dilution percentage. After evaluating the performance of the device with three different experiments, it was concluded that the developed impedance spectroscope has a great potential to be employed for various applications.

2.8.1 Randles circuit measurements

Methods

Randles circuit model is the simplest way to simulate an electrochemical system, and it is frequently used to analyze the impedance data. Randles circuit is formed with ideal electrical elements such as resistors and capacitors. In this experiment, the developed impedance spectroscope was used to measure the basic Randles circuit formed with two resistors and a capacitor. A 100 Ω resistor, a 220 Ω resistor, and different values of aluminum electrolytic capacitors (0.47 uF, 1 uF, 4.7 uF, and 47 uF) were connected on the breadboard as shown in Figure 2.7. The device was calibrated with a 100 Ω resistor which is approximately one-third of a sum of 100 and 220. Gain setting resistor (RFB) was set to 100 Ω to allow low impedance measurements. The data was collected over a frequency range from 20 Hz to 100 kHz, and it was plotted along with the theoretical line.

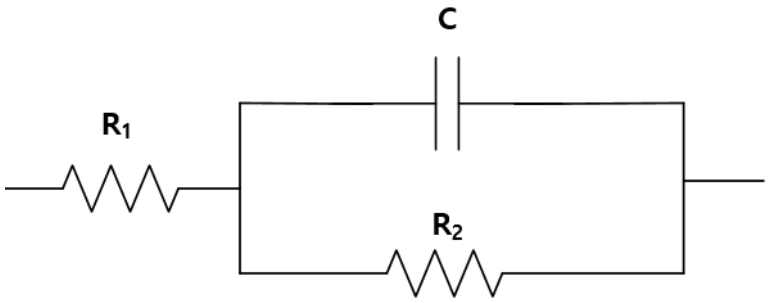

Figure 2.7: Randles circuit model used for device evaluation.

Results and Discussions

In Randles circuit model, the amount of current flow varies between a resistor and a capacitor that are connected in parallel and it depends on both the frequency of the input signal and the value of a capacitor. At a low frequency range, a capacitor has high impedance hence the only small amount of current flows through it. On the other hand, a capacitor has low impedance at a high frequency range where all the current from a first resistor flows directly through the capacitor. The higher value of the capacitor indicates that it can hold more energy and requires more time to be charged. Therefore, increasing the value of the capacitor will affect the impedance and phase curve to be shifted toward the left.

As shown in Figure 2.8, 2.9, 2.10, 2.11, the device properly captured the effect of different capacitor values over a same range of frequency. These figures indicate that the measured impedance data exhibit significant deviation from theoretical values at a low frequency region. In order to visualize these deviations quantitatively, relative errors of the impedance data and the phase data are plotted at seven different frequencies which are shown in Figure 2.12, 2.13,2.14, 2.15 respectively. At a high frequency region, errors of impedance and phase are as small as 1 %, yet impedance errors are as high as 30 % at a frequency below 500 Hz. These large errors at a low frequency range can be explained by understanding internal resistance or leakage resistance observed with aluminum electrolytic capacitors. Real electrolytic capacitors suffer from serious leakage current [43]. Accordingly, electrolytic capacitors are often modeled with a parallel resistor to represent the leakage path for the current. If capacitors are at high quality, this parallel resistance should be exceptionally

high to prevent current from leaking from capacitors. Nevertheless, electrolytic capacitors used in this experiment seem to have low value of parallel resistance that results in leakage current. Based on this speculation, if the more closely fitted plot is to be shown, Randles model must be modified to reflect the effect of the parallel resistance of a capacitor. In this context, the data is not fitted to the modified model since the coefficient of determinations of original data is high enough without modification. Therefore, it is concluded that the developed impedance spectroscope proved its ability to measure both impedance and phase very accurately despite the effect of leakage resistance arising from an electrolytic capacitor.

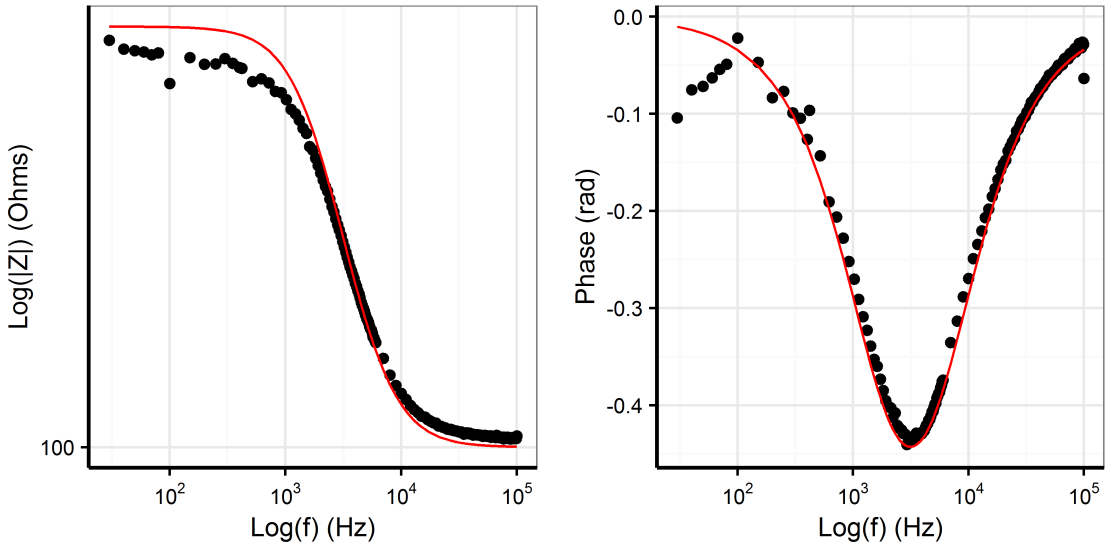

Figure 2.8: Bode plot for the model using a 0.47 uF capacitor along with theoretical line.

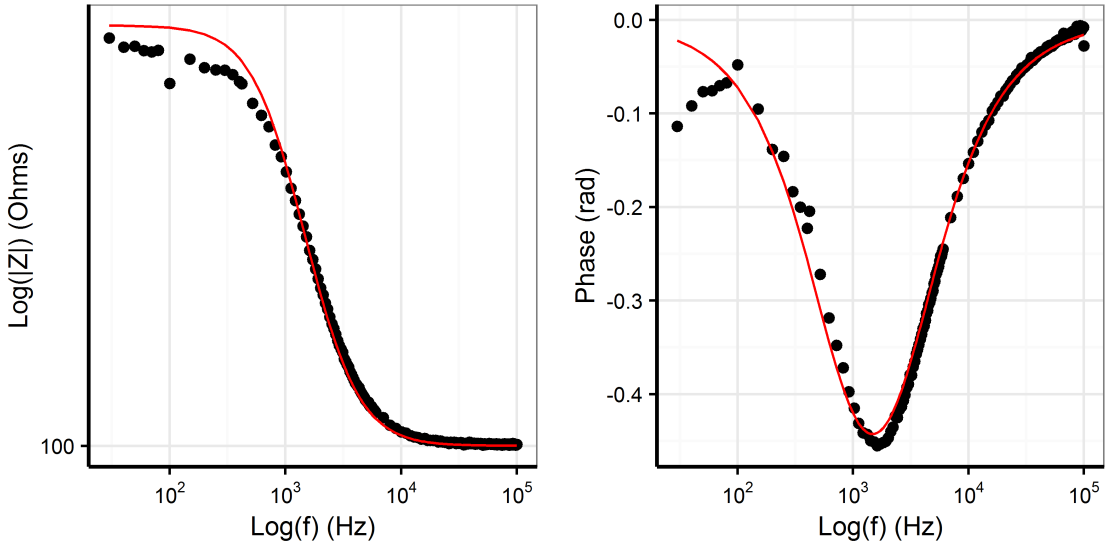

Figure 2.9: Bode plot for the model using a 1 uF capacitor along with theoretical line.

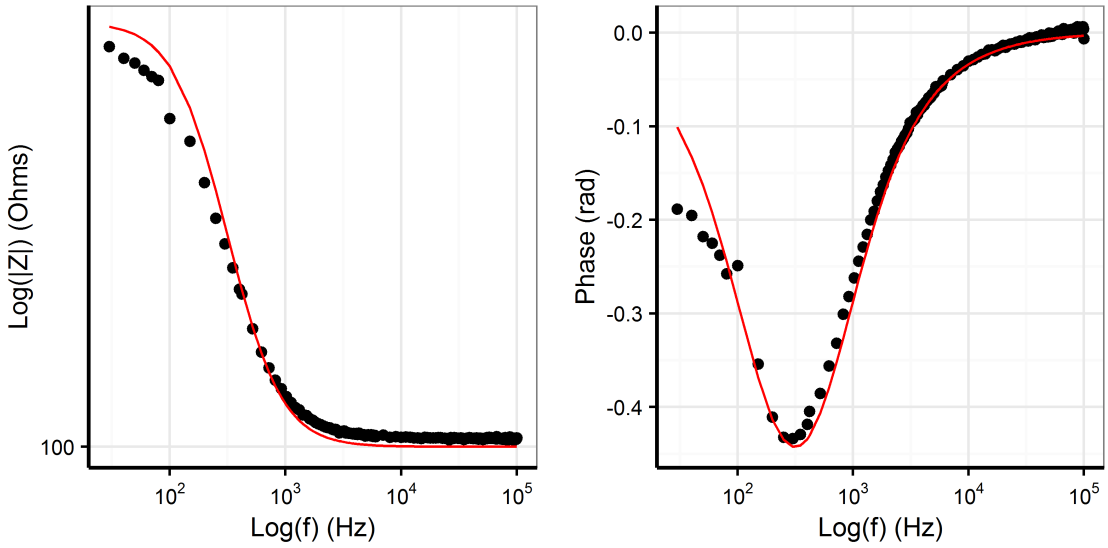

Figure 2.10: Bode plot for the model using a 4.7 uF capacitor along with theoretical line.

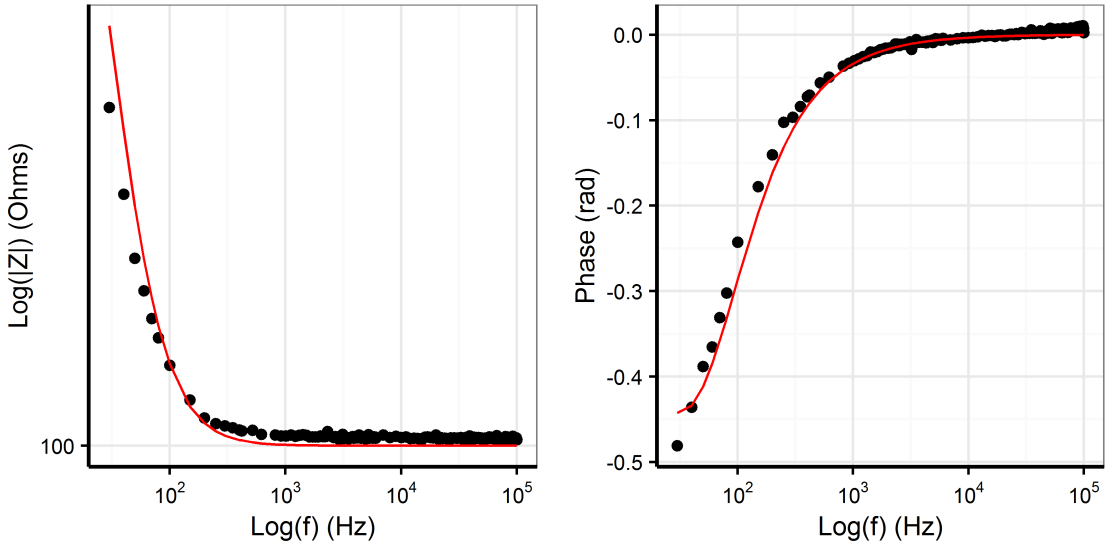

Figure 2.11: Bode plot for the model using a 47 uF capacitor along with theoretical line.

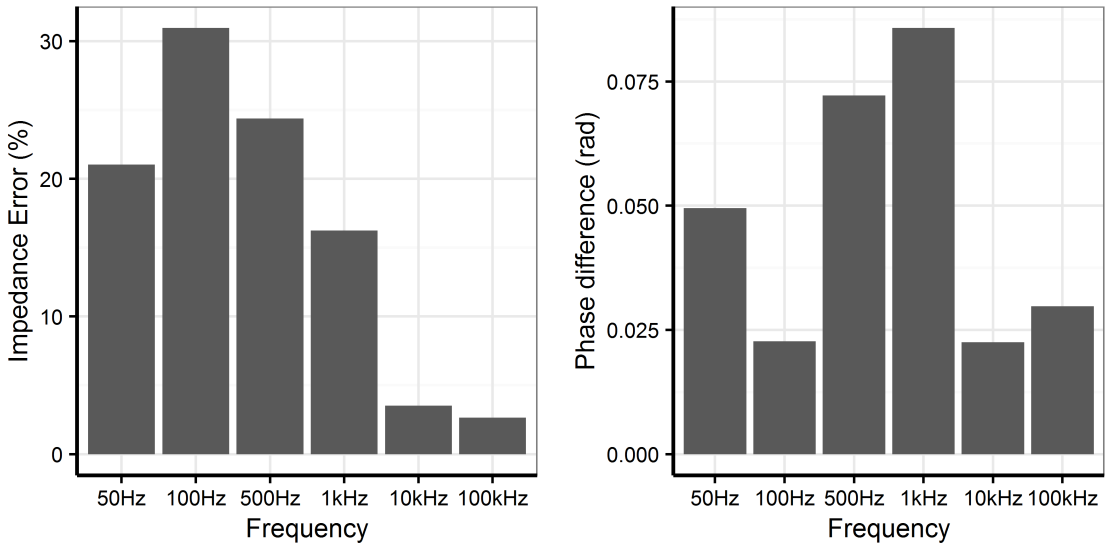

Figure 2.12: Impedance and phase errors at seven frequencies for the model using a 0.47 uF capacitor.

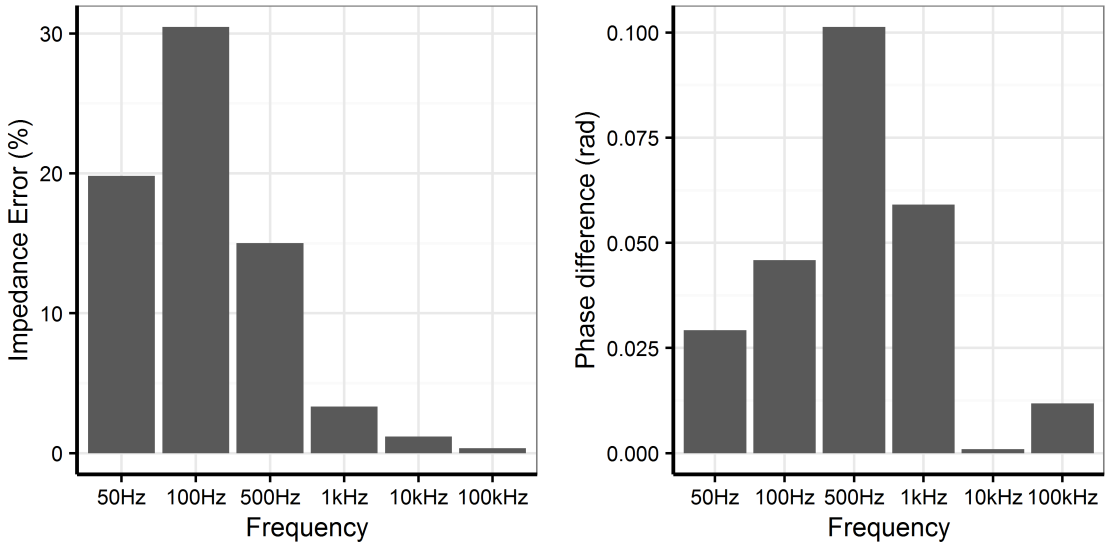

Figure 2.13: Impedance and phase errors at seven frequencies for the model using a 1 uF capacitor.

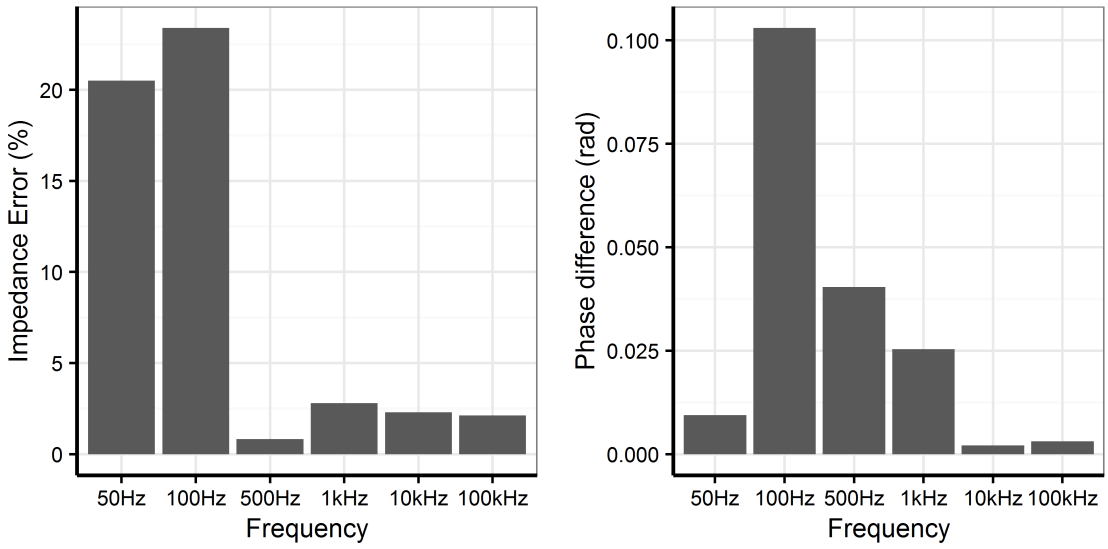

Figure 2.14: Impedance and phase errors at seven frequencies for the model using a 4.7 uF capacitor.

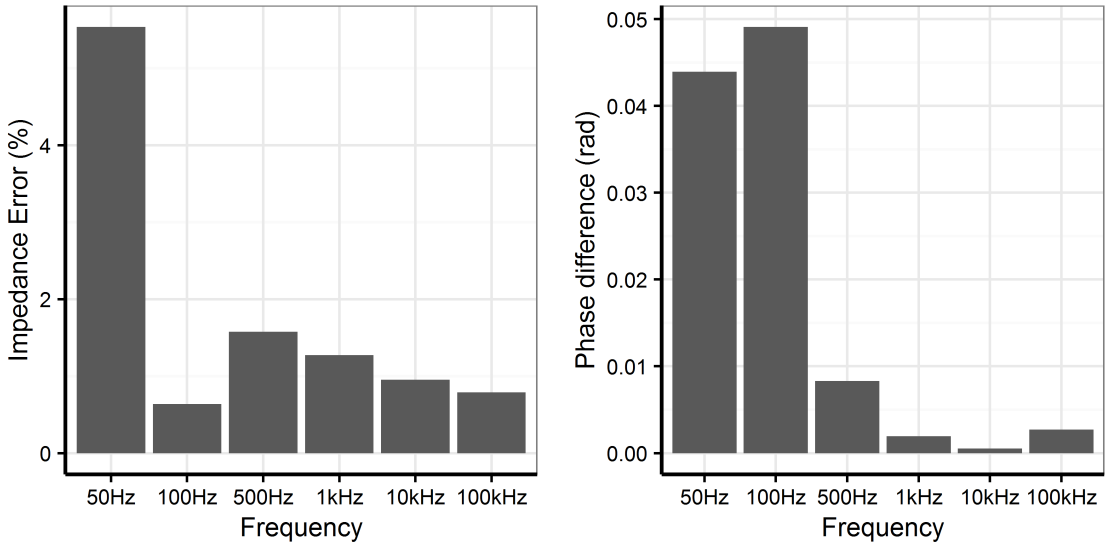

Figure 2.15: Impedance and phase errors at seven frequencies for the model using a 47 uF capacitor.

2.8.2 Corrosion monitoring

Copper exhibits high electrical and thermal conductivities, mechanical properties, as well as excellent corrosion resistance in several media [44–46]. Due to these valuable properties of copper, it is primarily employed in many industrial applications such as heating and cooling systems, electrical power lines, and pipelines. However, copper can still undergo corrosion process, and the resulting corrosion products can adversely affect the reliability of copper. As an example, chloride ions are known to react very aggressively with copper ions by forming a CuCl and soluble chloride complexes (CuCl2-) [44, 45]. Solid copper in chloride solution first loses its electron and becomes a copper ion (Equation 2.5). These copper ions then react with chloride ions to form cuprous chloride (CuCl), and the formed CuCl further reacts with chloride ions to form soluble copper chloride complex ($CuCl^-$) as described in Equation 2.6, 2.7.

$$Cu(s) \rightarrow Cu^+ + e^- \tag{2.5}$$

$$Cu^+ + Cl^- \rightarrow CuCl(ads) + e^- \tag{2.6}$$

$$CuCl(ads) + Cl^- \rightarrow CuCl_2^-(aq) \tag{2.7}$$

These reaction processes imply that chloride ion can corrode the copper and degrade the performance of the copper. Accordingly, the corrosion behavior of copper in chloride ion containing media has been investigated by many researchers [44–46]. In this study, the developed impedance spectroscope was used to monitor corrosion process of the copper electrode in 0.1M Hydrochloric acid (HCl) solution as a function of time. The data was collected over a full range of the frequency from 20 Hz to 100 kHz. The obtained data were fitted to the simiple Randles circuit model in an attempt to estimate electrochemical parameters. These estimated parameters were then used to infer the corrosion process of the copper electrode.

Methods

In this experiment, 100 mL of 0.1M HCl solution was prepared with 10N HCl concentrate from Fischer Scientific. The stock solution was kept at room temperature (25 °C) to minimize the variability of impedance due to temperature change. In order to calibrate the device, approximated resistance value of HCl solution has to be known. Accordingly, the conductivity table of the aqueous solution was used to interpolate the resistance of 0.1M HCl solution which was estimated to be less than 5 Ω [45]. Due to the small value of the expected impedance, the device was calibrated with a 100 Ω resistor and a 100 Ω gain setting resistor to allow measurements of low values of impedance.

The disposable copper electrodes were manufactured for this experiment. Copper foil tape with a width of 6.35 mm was affixed to an insulating polypropylene sheet. In order to create multiple numbers of identical size electrodes, the layout of the electrode was designed with Adobe Illustrator. The spacing between each copper strip was kept at 3 mm. After attaching copper strips on the insulator sheet, pin connector was soldered at each end of the electrode for wire connection. Continuity test was performed with a multimeter between the connector and the end of the electrode to ensure the electrode condition. Figure 2.16-(a) demonstrates the constructed copper electrodes.

Impedance measurements were carried out for five hours to monitor corrosion effect on the copper electrode in HCl solution. Each measurement was performed over a frequency range from 20 Hz to 100 kHz. The developed software automatically measures three times and returns the average value as a result. The electrode was submerged in 100 mL beakers containing 60 mL of 0.1 M HCl solution and it was fixed tightly at the edge of the beaker with a lab support stand. Also, a small stir bar was placed at the center of the beaker and it was rotated at 300 RPM continuously until the end of the experiment. A stir bar was used to minimize the effect of diffusion as well as to promote the speed of the reaction. Each measurements was obtained every 30 minutes.

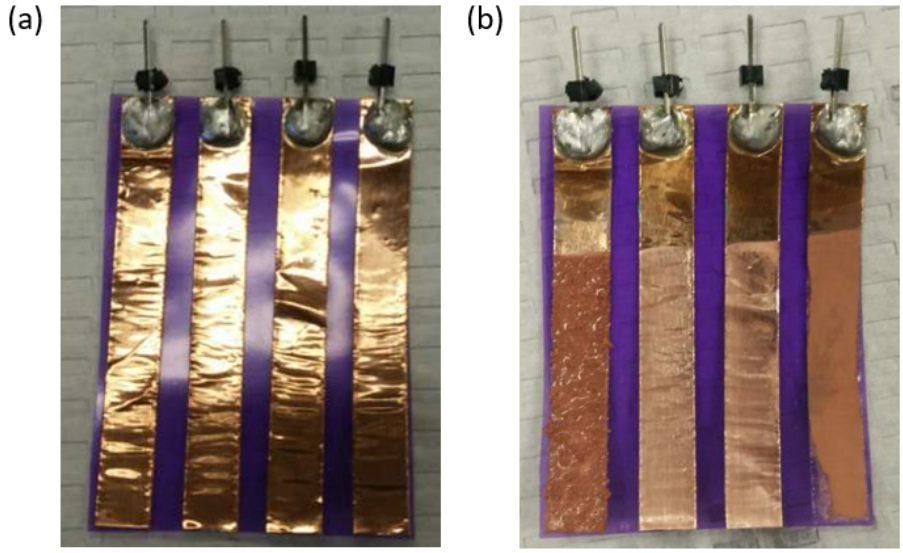

Figure 2.16: (a) Manufactured copper tape electrodes with spacing of 3 mm between each tape. (b) Same electrode after 5 hours of experiment. The anodic part of the electrode (one on the very right) lost portion of its copper. On the otherhand, the cathodic part of the electrode (one on the very left) accumulated copper residues on its surface.

Results and Discussion

As Figure 2.17 illustrates, impedance plots are shifted downward as immersion time increased. Phase plots in Figure 2.18 exhibits flattening trend toward 0 radians as the immersion time increased. In order to identify the underlying electrochemical phenomena of the system, the measured data was fitted to the model composed of electrical elements. Among many choices of the model that can explain corrosion process, the simple Randles circuit model was chosen. Since a stir bar was used to minimize the diffusion effect, Randles model without Warburg impedance was used to estimate three unknown parameters; solution resistance (R_{sol}), charge transfer resistance (R_{ct}), and double layer capacitance (C_{dl}). Their values and the coefficents of determination of the model at each measurement are presented in 2.4. Changes in the charge transfer resistance and double layer capacitance values over time were also plotted in Figure 2.19 to interpret the effect of corrosion on the system.

According to Butler-Volmer equation [1], charge transfer resistance is inversely related to the amount of current exchange during the redox reaction at the electrode surface. The higher value of R_{ct} indicates that only small amount of current flows during the reaction and vice versa. Therefore,

the high value of R_{ct} is expected to be measured at the first measurement, as no reactions are taking place right after submersion of the electrode. As immersion time increases, R_{ct} should decrease to reflect the existence of corrosion reaction of copper. Based on this principle, it is possible to correlate the measured data to observations during the experiment. During first two hours of the experiment, bubbles on the cathode, i.e. current collecting electrode, were observed. HCl solution is acidic, hence it contains the abundant amount of protons. As the impedance spectroscope injects the current from the anode to the cathode, two hydrogen ions aggregate with two electrons to form hydrogen gas at the cathode of which reaction formula is shown in Equation 2.8. In order to balance this reaction, there must be oxidation reaction of copper to release electrons at the anode. As described in Equation 2.5, solid copper at the anode dissolves into the solution by losing an electron. Then, the copper ions react with chloride ions to form copper chloride which was observed by the change of the solution color from transparent to bluish green. In addition to copper oxidation and copper chloride formation, other reactions can take place at the anode. Solid copper usually has a thin layer of copper oxide as a protection against the corrosion. After few minutes of the experiment, immersed parts of all four electrodes became shinier. This obeservation indicates that copper oxides are rapidly degraded and dissolved into the solution as the reaction formula, Equation 2.9, demonstrates.

The deposition of copper at the cathode was not observed during the first two hours of the experiment. By referring to the estimated value of the double layer capacitance as shown in Figure 2.19-(b), it is possible that there was a thick double layer formed by hydrogen ions and solvent molecules during early phase of the reaction. Thus the double layer formation impeded oxidized copper(II) ions to approach toward the surface of the cathode. By the time when the majority of hydrogen ions and chloride ions are consumed, then remaining copper ions dissolved in the solution started to react at the cathode and deposited. This phenomenon can be explained by correlating significant drop of the charge transfer resistance value after 3 hours. The visible copper accumulation on the cathode was observed after 3 hours (2.19-(a)). At the very end of the experiment, copper corrosion was more clearly observed at the anode where a portion of the electrode was dissolved completely. Moreover, the cathode was heavily doped with copper particles as illustrated in Figure 2.16-(b). The overall corrosion processes at the anode are demonstrated

in Equation 2.5, 2.6, 2.7, 2.9. The reaction processes at the cathode is presented in Equation 2.5, and 2.8. These reactions together led charge transfer resistance to decrease down to around 10 Ω. Decreased charge transfer resistance value can be related to increased surface area of the cathode as well as increased current flow for redox reaction of copper. Slightly increased value of solution resistance reveals that corrosion reaction consumed conducting species in the solution. The whole reaction processes during this experiment is depicted in Figure 2.20 as a function of time in y-axis. As well demonstrated by results, it is concluded that the developed impedance spectroscope can be employed to monitor the corrosion process and investigate possible reaction mechanisms.

$$2H^+ + 2e^- \rightarrow H_2(g) \tag{2.8}$$

$$Cu_2O + 2H^+ \rightarrow 2Cu^+ + H_2O \tag{2.9}$$

Immersion time	$R_{sol}(\Omega)$	$R_{ct}(\Omega)$	$C_{dl}(uF)$	R^2
0 min	17.27	54.22	13.1	0.8965
30 min	17.82	23.17	18.1	0.9725
60 min	18.09	37.2	3.55	0.9634
90 min	15.14	23.56	5.82	0.9859
120 min	14.88	16.17	3.87	0.9943
150 min	15.7	16.29	7.51	0.9915
180 min	16.17	10.21	3.47	0.9193
210 min	16.72	9.442	3.72	0.9425
240 min	17.63	9.252	3.36	0.9299
270 min	19.69	14.55	2.96	0.8839
300 min	22.37	11.05	4.19	0.9047

Table 2.4: Values of fitted parameters for all measurements.

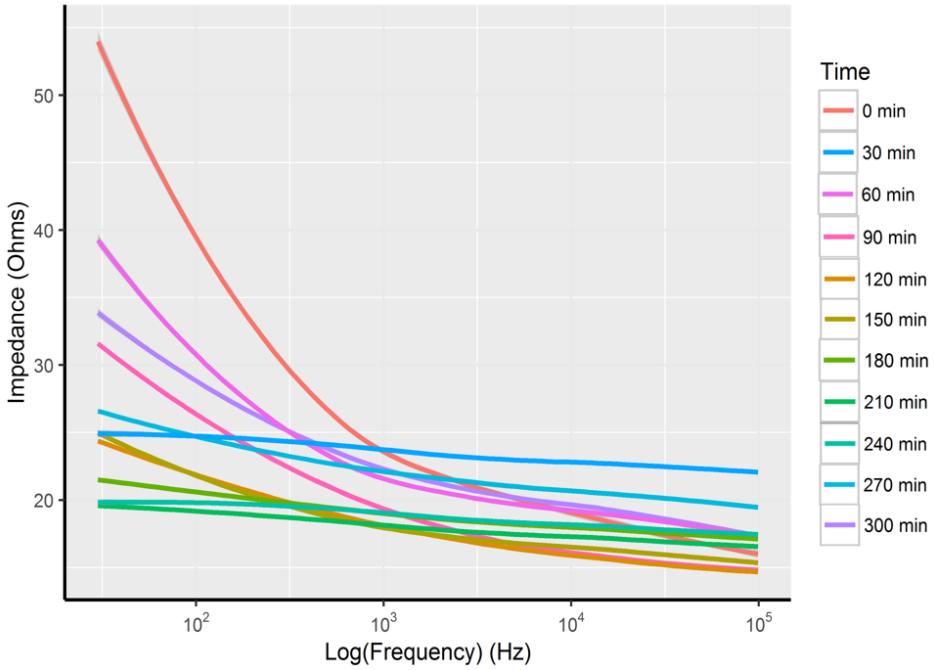

Figure 2.17: Impedance change over five hours.

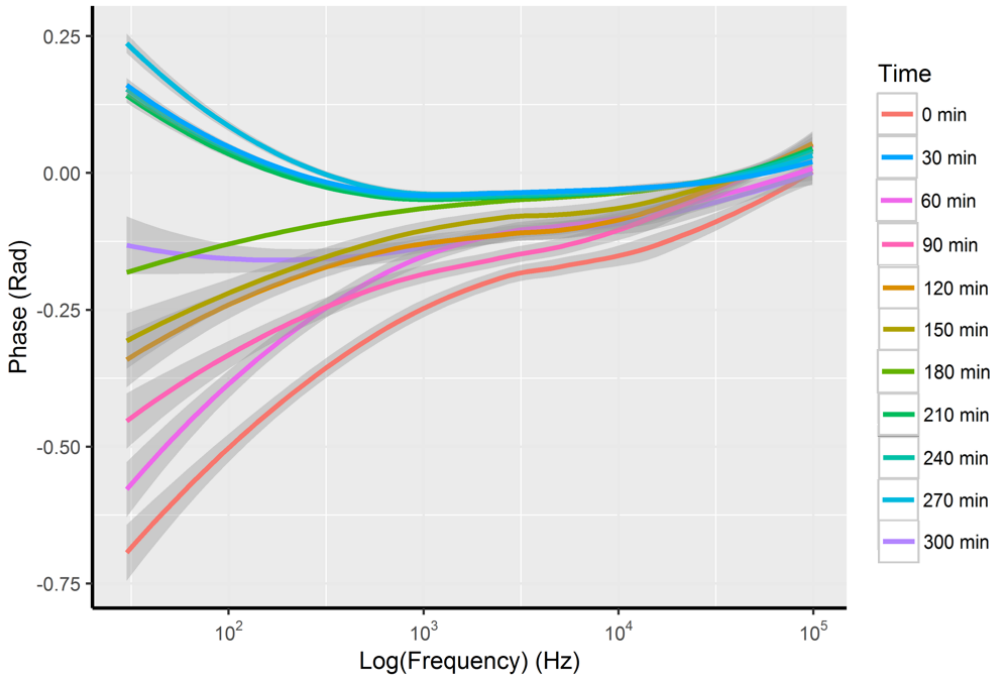

Figure 2.18: Phase change over five hours.

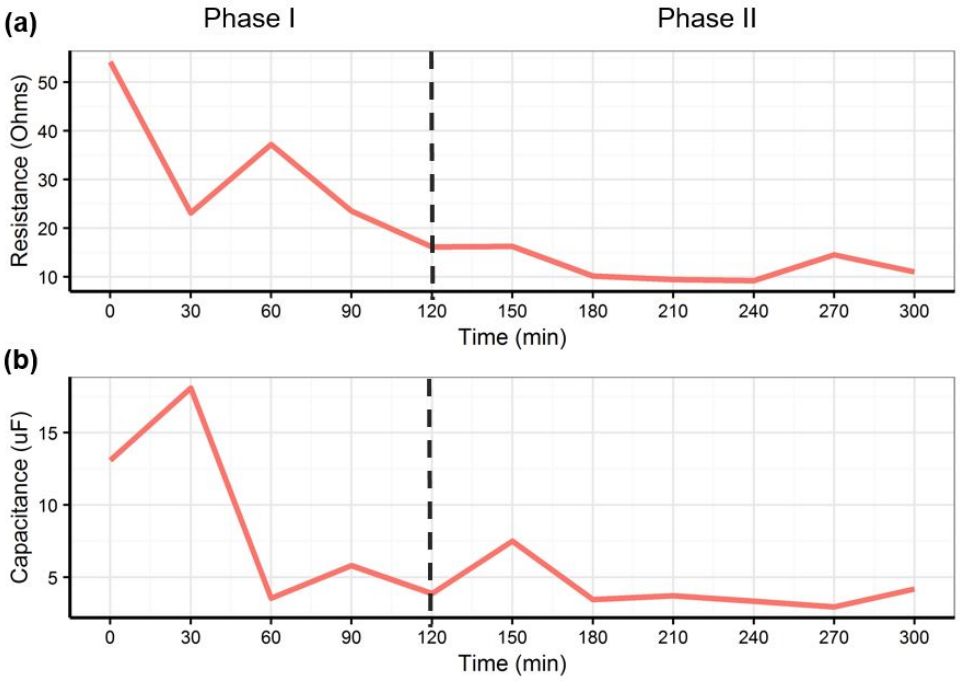

Figure 2.19: Estimated values of (a) charge transfer resistance, and (b) double layer capacitance change over five hours.

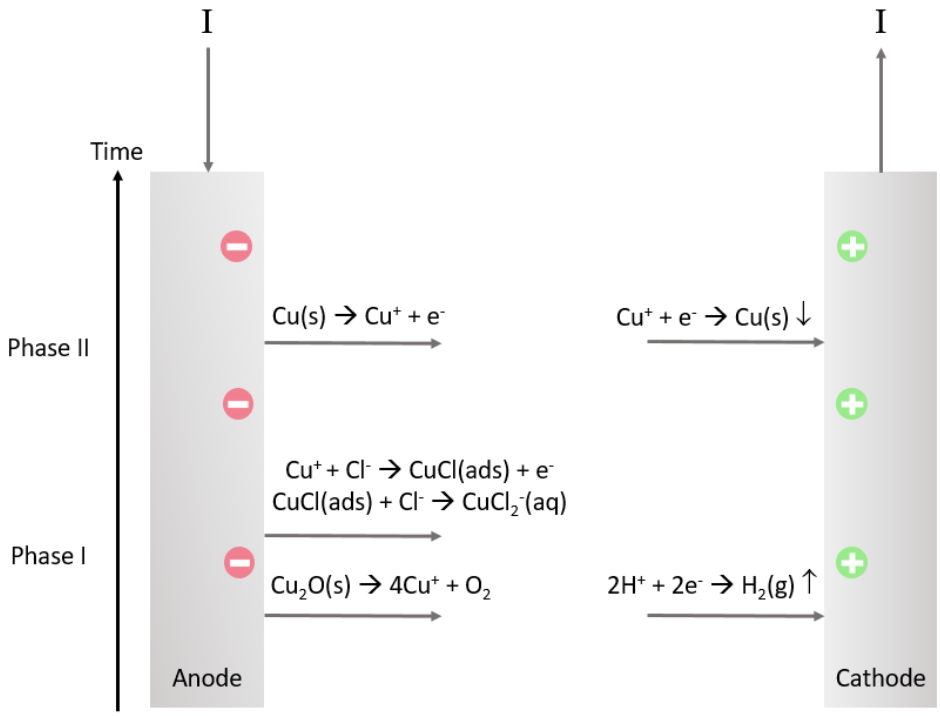

Figure 2.20: Copper corrosion reactions between electrode interface.

2.8.3 Detection of milk adulteration with tap water

Milk is an important agricultural product that supplies quality proteins, fat, carbohydrates, vitamins, and minerals to consumers. Due to its high nutritive value, milk intake has risen around the globe [47, 48]. However, such demand for milk has also contributed to an increase of fraudulent dairy production in developing countries [49]. The most common and simplest form of milk adulteration is mixing of tap water to reach the desired volume of the product [47, 49]. The addition of water reduces the nutritional value of pure milk, putting consumers at a risk of malnutrition [49]. In addition, multiple studies conducted in India found an alarming amount of detrimental contaminants in milk from local vendors. The majority of the tested products contained high volumes of skim milk powder, sugar, detergents, urea, and hydrogen peroxide [48, 50]. Many of the additives have been found to be perilous to human health if consumed in large amounts. For example, high amount of ammonia in urea have been found to contribute to loss of acquired speech and sensory disturbances [48]. It is critical to differentiate pure, wholesome milk from adulterated milk in order to avoid potential health risks.

Over the past few years, several analytical tools have been proposed for the screening of contaminants in the dairy industry. Amongst different analytical tools, liquid and gas chromatography (HPLC, GC) coupled with mass spectrometry (MS), spectroscopic techniques (Raman, NIR, MIR), and electrochemical sensors are used for the detection of milk adulterants [47, 51]. However, most of these proposed measurements is a time-consuming process that is performed in a laboratory environment. Moreover, their instruments are expensive [47, 52]. As there are needs to develop measurement technique that can detect milk adulteration in real-time, researchers proposed the use of EIS for the detection of milk adulteration [52–56].

Milk contains salt ions (e.g. Na^+, K^+, Cl^-) as well as temperature and pH dependent species associated with milk casein micelles, which exhibiting electrical properties [56]. Based on electrical properties, milk adulteration can be detected using EIS. For example, the addition of water with milk causes a decrease in concentration of free ions. This decrease in ion concentration results in a decrease in electrical conductance or an increase in electrical impedance [54]. Due to the change in concentration of conducting ions, EIS can measure the change in impedance values among samples. Multiple studies have successfully shown that EIS has a potential to detect diluted milk

and synthetic milk by analyzing impedance or conductance values [52–55, 57]. By assuming the water dilution with milk samples affect electrical properties, the goal of this thesis is to test the developd impedance spectroscope to investigate the change of impedance when different amount of tap water and a standard ionic solution is mixed with commercial full-fat milk.

Method

A titration-like experiment was performed in order to observe the effect of water dilution to a pure milk sample. Since tap water does not contain a consistent amount of conducting ions, a standard sodium chloride ionic solution with known impedance value was also used to be mixed with second milk sample. The range of dilution percentage was calculated to be from 5.00% to 80.63%. For the preparation of a milk sample, a fresh full-fat milk by Prairie Farms was purchased from the local market and stored at room temperature (25°C). From a fresh milk bottle, 25 mL was pipetted into a 150 mL beaker. Tap water was collected from the lab sink, and a 0.1% sodium chloride solution in deionized water was prepared and stored at room temperature. The impedance value of a tap water and a standard solution was approximately 1 $k\Omega$ and 2 $k\Omega$ accordingly. During the entire experiment, a stir bar was placed in the beaker and rotated at 300 RPM to mix milk and adulterants homogeneously. Impedance measurements in a frequency range of 20 Hz to 100 kHz were obtained using the developed impedance spectroscope. The electrode was manufactured using gold pin headers and was encapsulated with 3D printed PLA (PolyLactic Acid) case in an attempt to prevent liquid penetration into wires. The electrode was thoroughly rinsed with 70% ethanol and deionized water before the start of the experiment. Then, the electrode was immersed in the beaker for measurements. Adulterants were added every 3 minutes interval between each measurement.

Results and Discussions

Impedance and phase plots of adulterated milk with tap water and sodium chloride solution are shown in Figure 2.21, 2.22, 2.24, 2.25. These plots contain all 34 data together to demonstrate the effect of increasing dilution percentage. As their legend denotes, yellow color indicates lower dilution percentage starting from 0% and red color indicates higher dilution percentage up to

80.63%. According to these plots, impedance spectrum of two adulterants exhibits significant change in impedance values as dilution percentage increases. The impedance of a pure full-fat milk sample is approximately 120Ω, and the impedance of 80% diluted sample is at least two times larger than the original impedance. This increase in impedance value with higher dilution percentage can be explained by the fact that tap water and sodium chloride solution decrease the concentration of conductive ions in the sample, thus increasing the impedance value over a range of frequency. These trends are confirmed by the results presented by previous studies [54–56]. On the other hand, all phase spectrum of both of adulterants highly overlap each other and do not clearly reflect the change in dilution percentage.

In order to quantify how much of impedance changes at each dilution stage, data at 120 Hz, 1 kHz, 10 kHz, and 50 kHz are extracted from impedance spectrum. As illustrated in Figure 2.23, 2.26, the change of impedance value steeply increases after 60% dilution which reproduces exponential growth behavior. It is worth noting that there is a difference between tap water and sodium chloride solution. Milk adulterated with tap water showed the higher change of impedance at lower frequencies, however this is not the case with milk contaminated with sodium chloride solution. This might be explained by the fact that milk is much more complex liquid medium that is consisted of vitamins, fat, carbohydrates, milk casein, as well as minerals. Various components together casuses impedance behavior of milk to be more complex. Consequently, the developed impedance spectroscope validates its potential to be used as the detection tool of diluted milk by observing the change in impedance with careful statistical analysis.

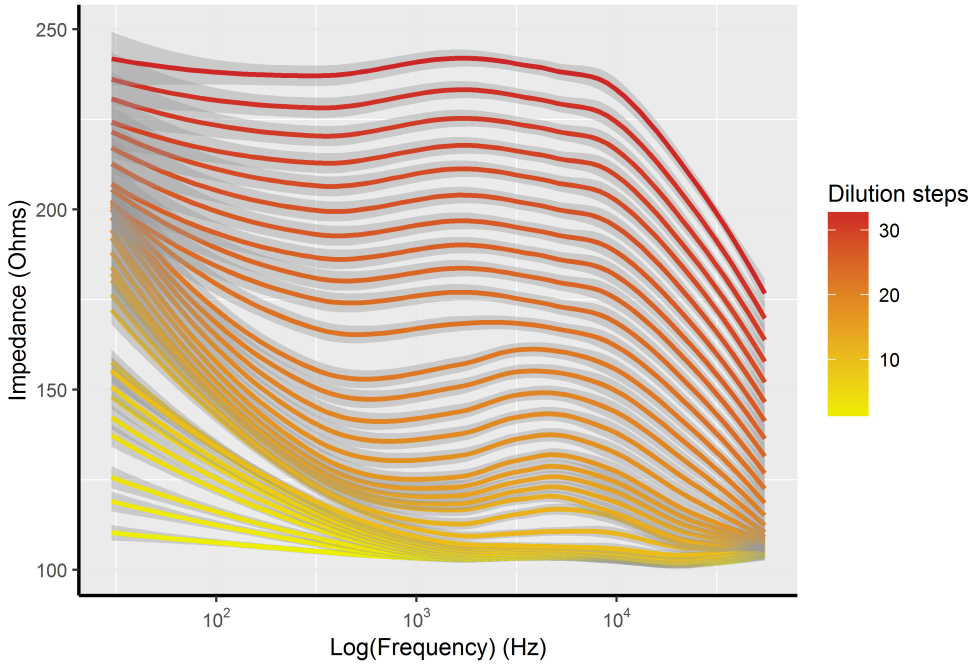

Figure 2.21: Impedance spectrum change over dilution with tap water

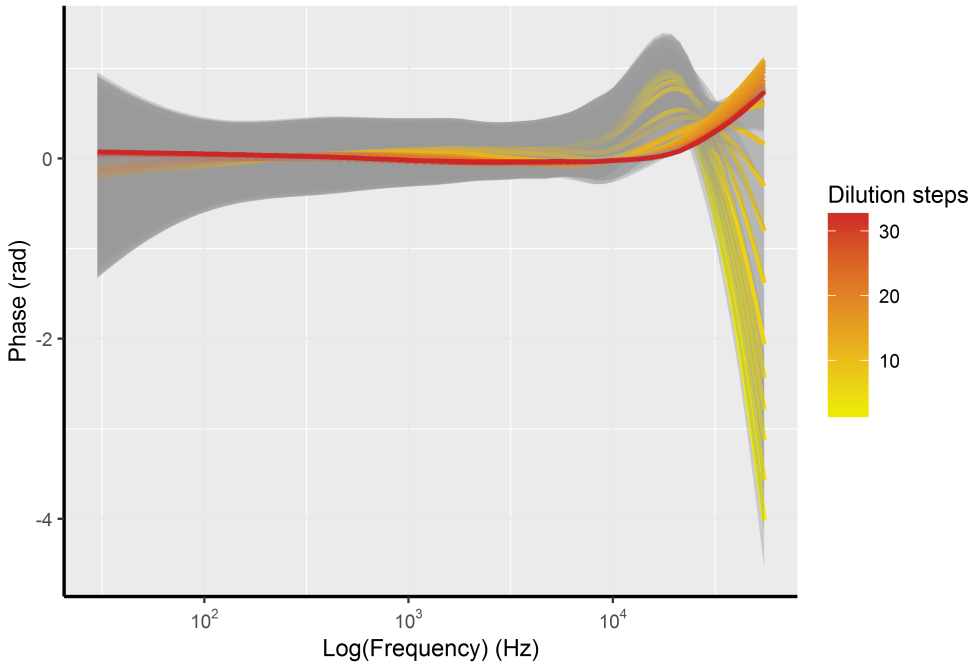

Figure 2.22: Phase spectrum change over dilution with tap water

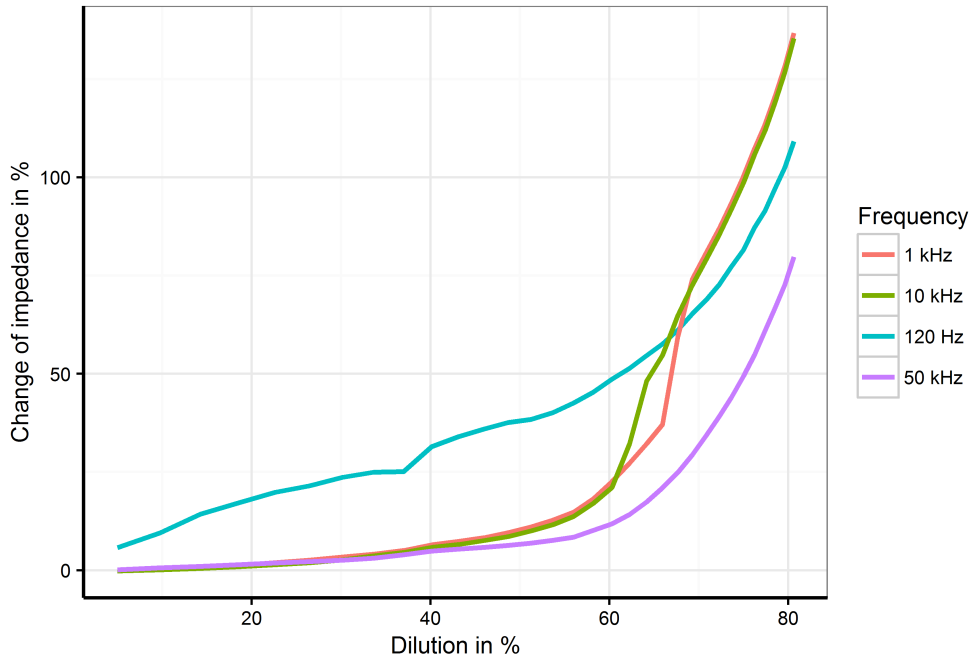

Figure 2.23: Change of impedance in percentage over dilution with tap water. Note that each of graph corresponds to different frequencies

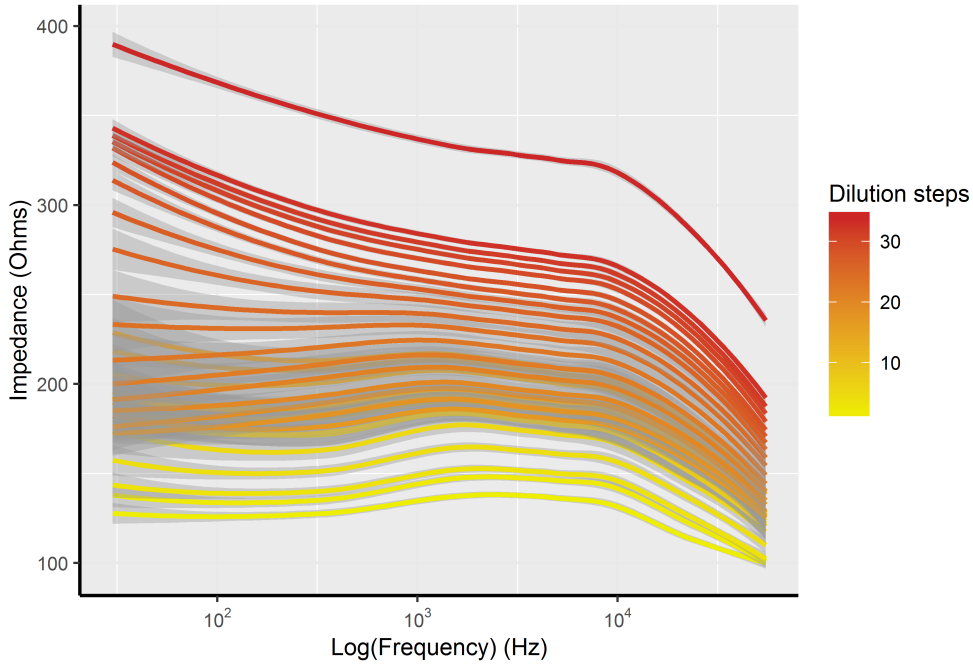

Figure 2.24: Impedance spectrum change over dilution with sodium chloride solution

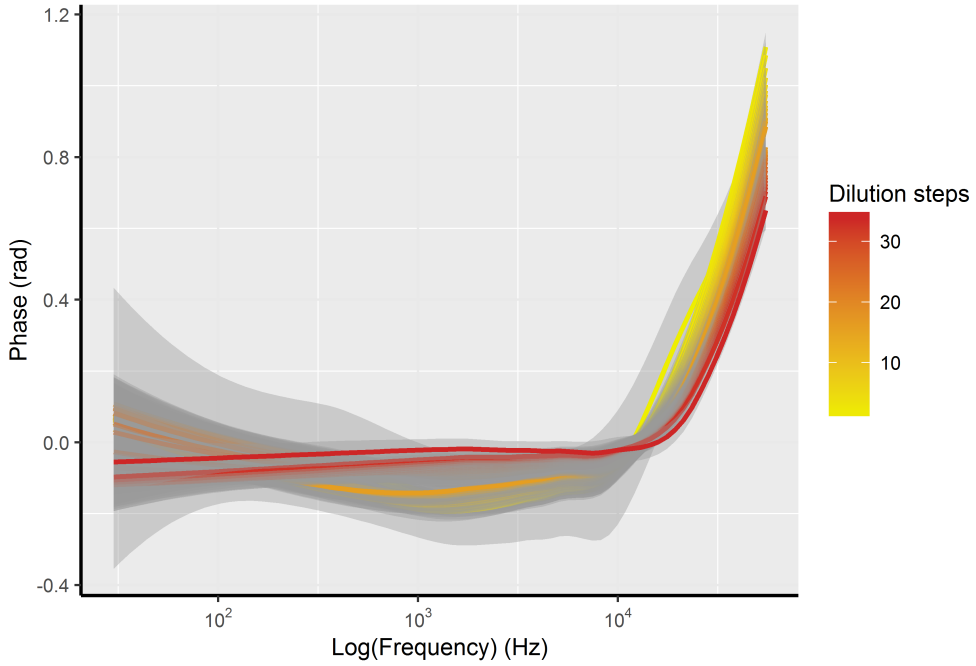

Figure 2.25: Phase spectrum change over dilution with sodium chloride solution

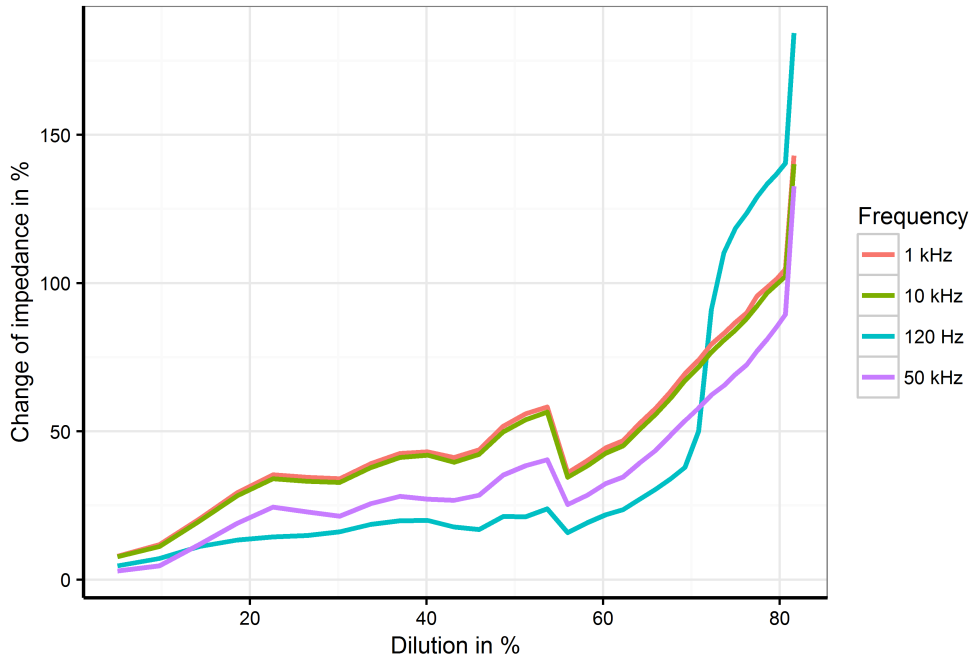

Figure 2.26: Change of impedance in percentage over dilution with sodium chloride solution. Note that each of graph corresponds to different frequencies.

2.9 Conclusion and future work

A low-cost, portable impedance spectroscope design proposed in this study satisfies the design criteria demonstrated in the earlier section. The total estimated cost of the complete impedance spectroscope is less than $100 which is at least ten times cheaper than commercialized products. The proposed impedance spectroscope system complies the portability and wireless requirements by implementing a single board microcontroller BeagleBone Black, a novel AFE to enable four electrodes measurements technique, and a Wi-Fi dongle. A commercial +5V battery can operate the complete system without any defects. In the end, a user-friendly web application is developed to promote the operation by non-experts.

For the development of AFE, the AD5933 is used as the main core of running impedance measurement. The AD5933 chip has numerous advantages to be employed when designing portable impedance measurement system. Nevertheless, the AD5933 suffers from few issue which directly affects the accuracy and the quality of the measured impedance data. In order to compensate these issues, a novel and simple AFE design are presented in this study. The developed impedance spectroscope was tested through three different experiments to evaluate its performance. According to results demonstrated above, the developed spectroscope can produce very accurate data and is capable of monitoring corrosion process or detecting diluted milk. These results proved its potential to be used for various applications as well. Although the interpretation of the impedance data requires further data processing such as fitting to the equivalent circuit model, the proposed system can generate significant data that includes essential electrochemical information.

In the future, the proposed system can be further miniaturized by employing an Adafruit Feather 32u4 microcontroller. This microcontroller conforms features of Arduino, but it is much smaller than Arduino Uno, and it includes Bluetooth chip for wireless communication. The software for this new design will operate differently from the current version because this microcontroller can not run an operating system to open up the web application. Instead, users will be in the middle of the impedance spectroscope and the web application as shown in Figure 2.27. In a nutshell, users request for measurement and the sensor returns the impedance data. Then, the data is automatically uploaded to the web application hub to be processed, and the result is finally shown to users. Based on the need of users, artificial neural network (ANN) algorithm can also be

implemented into the web application for the classification task.

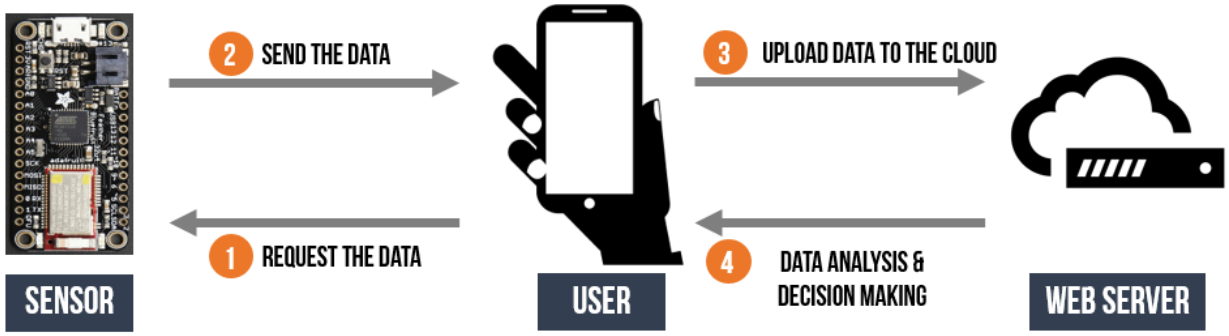

Figure 2.27: Future design of the hardware and the software structure.

2.10 References

[1] V. F. Lvovich, *Impedance spectroscopy: applications to electrochemical and dielectric phenomena*. NJ: Wiley, 2012.

[2] E. Barsoukov and J. R. Macdonald, *Impedance spectroscopy: theory, experiment, and applicatios*. NJ: Wiley, 2005.

[3] "Markets and markets," (Date last accessed 21-January-2017). [Online]. Available: http://www.marketsandmarkets.com/PressReleases/smart-sensor.asp

[4] G. W. Hunter et al., "Smart sensor systems," *The Electrochemical Society Interface*, pp. 29–34, 2010.

[5] H. Gao et al., "Design and tests of a smartphones-based mult-lead ecg monitoring system," presented at the 35th Annual International Conference of the IEEE EMBS, July, 2013.

[6] J. M. Azzarelli et al., "Wireless gas detection with a smartphone via rf communication," *PNAS*, vol. 111, no. 51, pp. 18 162–18 166, 2014.

[7] D.Fisher, "Rapid deployment of internet-connected environmental monitoring devices," *Advances in internet of things*, vol. 4, pp. 46–54, 2014.

[8] M. K. Bhanarkar and P. M. Korake, "Soil salinity and moisture measurement system for grapes field by wireless sensor network," *Cogent Engineering*, vol. 3, no. 1, 2016.

[9] B. Sainz et al., "A novel low-cost sensor prototype for monitoring temperature during wine fermentation in tanks," *Sensors*, vol. 13, no. 3, pp. 2848–2861, 2013.

[10] S. F. D. Gennaro et al., "An open-source and low-cost monitoring system for precision enology," *Sensors*, vol. 14, pp. 23 388–23 397, 2014.

[11] A. Devices, "1 msps, 12-bit impedance converter, network analyzer rev.e," 2013, (Date last accessed 24-September-2016). [Online]. Available: http://www.analog.com/media/en/technical-documentation/data-sheets/AD5933.pdf

[12] P. Kurzeweil and H. J. Fischle, "A new monitring method for electrochemical aggregates by impedance spectroscopy," *Journal of Power Sources*, vol. 127, pp. 331–340, 2004.

[13] J. Ferreira et al., "Ad5933-based electrical bioimpedance spectrometer towards textile-enabled applications," presented at the 2011 Annual International Conference of the IEEE Engineering in Medicine and Biology Society, August, 2011, pp. 3282–3285.

[14] Y. Yang et al., "Design and preliminary evaluation of a portable device for the measurement of bioimpedance spectroscopy," *Physiolgical Measurement*, vol. 27, no. 12, pp. 1293–1310, 2006.

[15] S. Corbellini and A. Vallan, "Arduino-based portable system for bioelectrical impedance measurement," presented at the 2014 IEEE International Symposium on Medical Measurements and Applications, June, 2014, pp. 1–5.

[16] "Beaglebone black," (Date last accessed 21-January-2017). [Online]. Available: https://beagleboard.org/black

[17] "Arduino uno," (Date last accessed 21-January-2017). [Online]. Available: https://www.arduino.cc/en/Main/ArduinoBoardUno

[18] "Raspberry pi 2 model b," (Date last accessed 21-January-2017). [Online]. Available: https://www.raspberrypi.org/products/raspberry-pi-2-model-b/

[19] C. Margo et al., "A four-electrode low frequency impedance spectroscopy measurement system using ad5933 measurement chip," *Physiolgical Measurement*, vol. 34, no. 4, pp. 391–405, 2013.

[20] F. Seoane et al., "An analog front-end enables electrical impedance spectroscopy system on-chip for biomedical applications," *Physiolgical Measurement*, vol. 29, no. 6, pp. 267–278, 2008.

[21] "High accuracy impedance measurements using 12-bit impeedance converters," (Date last accessed 21-January-2017). [Online]. Available: http://www.analog.com/media/en/reference-design-documentation/reference-designs/CN0217.pdf

[22] H. P. Schwan, "Alternating current electrode polarization," *BioPhysik*, vol. 3, pp. 181–201, 1966.

[23] H. P. Schwan, "Electrode polarization impedance and measurements in biological materials," *Annals of the New York Academy of Science*, vol. 148, pp. 191–209, 1968.

[24] D. K. Kamat et al., "Blood glucose measurement using bioimpedance technique," *Advances in Electronics*, vol. 2014, pp. 1–5, 2014.

[25] F. Noveletto et al., "Low-cost body impedance analyzer for healthcare applications," presented at the II Latin American Conference on Bioimpedance, vol. 54, Jan, 2016, pp. 56–59.

[26] D. Zhang et al., "Protein detecting with smartphone-controlled electrochemical impedance spectroscopy for point-of-care applications," *Sensors and Actuators B*, vol. 222, pp. 994–1002, 2016.

[27] D. Zhang et al., "Smartphone-based portable biosensing system using impedance measurement with printed electrodes for 2,4,6-trinitrotoluene (tnt) detection," *Biosensors and Bioelectronics*, vol. 70, pp. 81–88, 2015.

[28] J. Ding et al., "A portable pesticide residues detection instrument based on impedance immunosensor," *Sensors and Transducers*, vol. 172, no. 6, pp. 27–33, 2014.

[29] V. F. Lvovich and M. F. Smeichowski, "Ac impedance characterization of highly resistive media using four-electrode electrochemicial cells," *ECS Transactions*, vol. 25, no. 32, pp. 1–25, 2010.

[30] Z. Moron, "Considerations on the accuracy of measurements of electrical conductivity of liquids," in *XVIII IMEKO World Congress*, Brazil, 2006.

[31] D. Pelc et al., "Four-contact impedance spectroscopy of conductive liquid samples," *Review of Scientific Instruments*, vol. 82, no. 7, pp. 073 905–073 907, 2011.

[32] Z. Chang et al., "A comparison of two- and four-electrode techniques to characterize blood impedance for the frequency range of 100 hz to 100 mhz," *IEEE Transactions on Biomedical Engineering*, vol. 55, no. 3, pp. 1240–1247, 2008.

[33] C. Margo et al., "Four electrode embedded bioimpedance measurement system," *IEEE: Faible Tension Fable Consommation*, pp. 1–4, 2013.

[34] U. Pliquett and A. Barthel, "Interfacing the ad5933 for bio-impedance measurements with front ends providing galvanostatic or potentiostatic excitation," *Journal of Physics: Conference Series*, vol. 407, pp. 1–4, 2012.

[35] A. Devices, "Precision, low noise, cmos, rail-to-rail, input/output operational amplifiers," 2013, (Date last accessed 24-September-2016). [Online]. Available: http://www.analog.com/media/en/technical-documentation/data-sheets/AD8605_8606_8608.pdf

[36] H. P. Schwan, "Four-electrode null techniques for impedance measurement with high resolution," *The Review of Scientific Instruments*, vol. 39, no. 4, 1968.

[37] A. Devices, "Jfet input instrumentation amplifier with," 2013, (Date last accessed 24-September-2016). [Online]. Available: http://www.analog.com/media/en/technical-documentation/data-sheets/AD8605_8606_8608.pdf

[38] "debian," (Date last accessed 21-January-2017). [Online]. Available: https://www.debian.org/

[39] "Node.js," (Date last accessed 21-January-2017). [Online]. Available: https://nodejs.org/en/

[40] "Express.js," (Date last accessed 21-January-2017). [Online]. Available: http://expressjs.com/

[41] "Bootstrap3," (Date last accessed 21-January-2017). [Online]. Available: http://getbootstrap.com/

[42] "D3.js," (Date last accessed 21-January-2017). [Online]. Available: https://d3js.org/

[43] "Leakage current properties of modern electrolytic capacitors," 2001, (Date last accessed 19-October-2016). [Online]. Available: http://www.tadiranbatteries.de/pdf/applications/leakage-current-properties-of-modern-electrolytic-capacitors.pdf

[44] M. M. Al-Abdallah et al., "Corrosion behavior of copper in chloride media," *The Open Corrosion Journal*, vol. 2, pp. 71–76, 2009.

[45] E. M. Sherif, "Corrosion behavior of copper in 0.50m hydrochloric acid pickling solutions and its inhibition by 3-amino-1,2,4-triazole and 3-amino-5-mercapto-1,2,4-triazole," *International Journal of Electrochemical Sciences*, vol. 2, pp. 1884–1897, 2012.

[46] Z. Li et al., "Inhibition of the corrosion of copper in a sodium chloride solution using 4-((4-dodecylphenylimino)methyl)phenol," *International Journal of Electrochemical Sciences*, vol. 8, pp. 6513–6523, 2013.

[47] P. Amrita et al., "Detection of adulteration in milk: A review," *International Journal of Dairy Technology*, vol. 70, no. 1, pp. 23–42, 2017.

[48] J. K. Swathi and N. Kauser, "A study on adulteration of milk and milk products from local vendors," *Internationl Journal of Biomedical and Advance Research*, vol. 6, no. 9, pp. 678–681, 2015.

[49] H. Caroline et al., "Impacts of milk fraud on food safety and nutrition with special emphasis on developing countries," *Comprehensive Reviews in Food Science and Food Safety*, vol. 15, no. 1, pp. 130–142, 2016.

[50] S. Hemanth and M. Sukumaran, "Milk adulteration in hyderabad, india - a comparative study on the levels of different adulterants present in milk," *Journal of Chromatograph Separation Techniques*, vol. 5, no. 1, pp. 1–3, 2014.

[51] C. F. Nascimento et al., "Recent advances on determination of milk adulterants," *Food Chemistry*, vol. 221, pp. 1232–1244, 2017.

[52] A. Sadat et al., "Determining the adulteration of natural milk with synthetic milk using ac conductance measurement," *Journal of Food Engineering*, vol. 77, pp. 472–477, 2006.

[53] G. Durante et al., "Electrical impeedance sensor for real-time detection of bovine milk adulteration," *IEEE Sensors Journal*, vol. 16, no. 4, pp. 861–865, 2016.

[54] J. K. Banach et al., "Possibilities of using electrical parameters of milk for assessing its adulteration with water," *Internationl Journal of Food Properties*, vol. 15, pp. 274–280, 2012.

[55] P. Bertemes-Filho et al., "Bioelectrical impedance analysis for bovine milk: preliminary results," *Journal of Physics: Conference Series 224*, 2010.

[56] M. Henningsson et al., "The electrical conductivity of milk - the effect of dilution and temperature," *Internationl Journal of Food Properties*, vol. 8, pp. 15–22, 2005.

[57] A. Abedelkafi et al., "Impedance investigation of milk dilution," *Journal of Food Engineering*, vol. 77, pp. 472–477, 2006.

Chapter 3

Characterization of the Estrous Cycle in Sows using Impedance Spectroscopy

3.1 Abstract

This chapter describes an application of impedance spectroscopy for characterizing the estrous cycle in sows. Traditionally, estrus in sows has been detected by observing the sow's behavioral response. In order to assist the swine breeding process, we propose to employ a low-cost, portable impedance spectroscope to find the relationship between vaginal tissue impedance and the phase of the estrous cycle in order to aid detecting estrus. Impedance spectra of ten sows were obtained over the estrous cycle. Secondly, ten pregnant sows were scanned to investigate the relationship between the change of impedance and time of farrowing. Lastly, the developed impedance spectroscope was deployed to collect estrous cycle data on a large scale farm. The last experiment took place at a breeding research farm operated by JBS United. Results showed that tissue impedance sharply increases about 20 Ω and decreases about 50 Ω days before the estrus onset or farrowing. Unfortunately, the third experiment was stopped on the second day due to failure of the system in the field. Even though the device needs further modification to be more robust for field applications, the impedance spectroscope was able to repeatedly capture characteristic trends in impedance spectra over the estrous cycle. Therefore, it shows its potential to be used as a decision-making tool to optimize artificial insemination in swine breeding operations.

3.2 Background and Objectives

As pork consumption increases worldwide, increasing the efficiency of reproductive technologies is an integral part of the management process in pork production [1]. Reproductive efficiency is a primary factor that influences profitability of farmers [2,3]. Farmers profitability is maximized by

producing the greatest numbers of pigs/sow/year, and ideally, sows have the potential to farrow at max 2.6 times/year which results in approximately 52 pigs weaned/mated sow/year [4]. Nevertheless, it is difficult to achieve the maximum litter production, since the reproductive success is predominantly affected by environmental and management factors such as season, nutrition, and disease [2, 4]. There are various management processes to increase reproductive efficiencies such as genetic selection, disease control, and artificial insemination. Among them, detection of estrus in sows is an important process, since failure to detect estrus accurately has the greatest influence on farrowing rate and litter size [2–4]. Currenlty, estrus in sows is determined by exposing them to a sexually mature boar while technicians apply back pressure to inspect standing response of sows [2]. This method is proven to be highly accurate when sows are exposed to sight, sound, and smell of a sexually active boar. However, controlling a boar is labor intensive requiring one to two people, therefore our tool aims to reduce that labor. Also animals not showing behavioral estrus could nevertheless still conceive and become pregnant. It is critical to have another decision-making tool to determine the time of estrus. We developed a low-cost, portable impedance spectroscope, which was deployed at a swine research center in Urbana-Champaign to collect the vaginal impedance spectra from sows in order to detect estrus and the time of farrowing.

3.3 Estrous cycle of sows and its correlation to electrical impedance

3.3.1 Estrous cycle of sows and hormonal changes

The typical estrous cycle for sows is known to span 21 days [5–7]. During the cycle, there are three distinct phases, namely the estrus, luteal phase, and follicular phase. Figure 3.1 represents the estrous cycle of sows with three different phases.

Each of these phases correlates with recognizable hormonal changes. Starting from estrus, this period spans 1-2days for gilts and 2-3 days for weaned sows [5]. At the end of the estrus phase, sows ovulate and enter the luteal phase after ovulation. The luteal phase persists about 12-14 days and ovaries produce progesterone (P4) to facilitate conception and restrict follicular development as well as to prevent the subsequent onset of estrus in pregnant sows [7]. The P4 level gradually

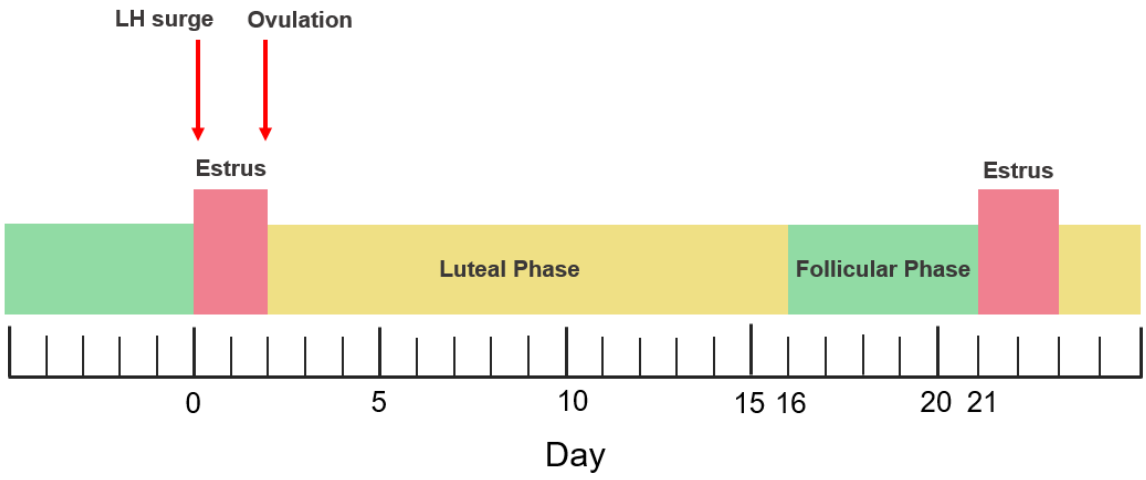

Figure 3.1: Normal estrus cycle for swine [7].

increases and reaches its peak 8-9 days after ovulation. In non-pregnant sows, the prostaglandin (PGF-α) production by uterus, the corpora lutea regresses and terminates progesterone production to allow the animal to cycle once more [7].

After the luteal phase, the follicular phase commences and lasts for 4-6 days. Small to medium sized follicles continue to grow and become much larger sized follicles in response to FSH production which reaches its peak on 2-3 days after the onset of behavioral estrus [6]. During the estrus phase, LH is secreted to trigger ovulation of fertile eggs within 2-3 days. Because progesterone production is prohibited by PGF-α, other hormones such as gonadotropin-releasing hormone (GnRH), luteinizing hormone (LH), and follicle-stimulating hormone (FSH) are secreted [6, 7]. These hormones foster oestradiol production that stimulates behavioral estrus such as the standing response in the presence of a boar, swollen and redden vulvar area, and mucus production [5, 7]. After ovulation of fertile eggs, the estrous cycle continues to repeat.

When sows are successfully mated, they enter the gestation period for 114-115 days. During gestation, progesterone levels reach its peak by day 12 and gradually decrease by day 104 [6]. Additionally, prolactin level increases significantly in late pregnancy and remains high until the early lactation period. After farowing, lactation lasts for three weeks or until pigs are weaned. When the litter is removed, sows will show estrus and ovulation within 5-6 days; and the estrous cycle restarts [5, 6]. It is worth noting that gilts are denoted as parity zero, as they had no litter

production to avoid any confusion regarding the parity of sows. When sows produce litters for the first time, they are denoted as parity one sows.

3.3.2 Changes in vaginal impedance during the estrous cycle

There are several auxiliary diagnostic instruments available for monitoring the estrous cycle of domestic animals. One approach of keeping track of the estrous cycle is to monitor the change of vaginal impedance. Throughout several decades, many researchers have demonstrated cyclic changes of vaginal impedance in sows [8–16], cows [17–26], ewes [27–29], rats [30–33], and buffalo [34]. In these domestic animals, vaginal impedance is measured to be lowest during the follicular phase and the highest during the luteal phase of the estrous cycle [10,16]. According to the extensive research on sows by Peter Rezac, he concluded that it is feasible to use the vaginal impedance of sows as an indicator of the timing of preovulatory LH peak [16].

There is a possible theory to account for these cyclic changes of vaginal impedance. During the estrous cycle, physiological structure and function of the vagina change. These histological and histochemical changes related to ovarian follicular growth and corpus luteum formation and regression are accompanied by an alteration in its passive electrical properties [16]. At the onset of estrus, researchers have discovered that the volume of vaginal mucus increases along with an increase of sodium chloride content [8,12,20].When the amount ions in mucus increases, the increase of electrical conductivity is expected. Since the electrical conductivity is inversely related to the impedance, this increase of ions will cause the impedance to decrease. In addition to the electrolyte change, several studies have deduced that increased hydration and congestion of blood vessels can also alter the vaginal impedance values [21, 27, 34].

In addition to hypotheses related to the vaginal impedance change, there have been rigorous attempts to find the relationship between different hormones and the vaginal impedance. As the level of plasma progesterone, estradiol, and LH fluctuate over the estrous cycle, the change in vaginal impedance is correlated to cyclical hormonal changes [9, 10, 15–18, 24–26, 28, 29, 34]. According to these data, it is argued that the LH peak at the onset of estrus is highly correlated to the lowest value of vaginal impedance in sows [9, 10, 15, 16] and similar patterns are also observed in other domestic animals as well [24, 26]. While the mechanism behind impedance changes remains unelucidated,

detecting these changes may provide useful information for determining estrus timing in the swine breeding process.

3.3.3 Instruments comparison and design criteria

Table 3.1 summarizes the various electrical instruments used for animal fertility application. As shown, the majority of instruments measure the impedance rather than the pure resistance. The advantage of obtaining the impedance spectrum is the fact that it can provide rich information about the object of interest by measuring the property of the resistance as well as the ability to modulate the availability of electrical energy [35,36]. Although impedance data can provide a more comprehensive information, instruments used in previous research are limited in two aspects.

Animal of Interest	Instrument Type	Frequency Range	Citation
Cattle	Two electrodes, Ohmeter	DC	D.Schams, I. Tasal, W.Leidl [18, 22, 26]
	Two electrodes, Impedance	40 kHz	G. S. Lewis [19]
	Two electrodes, Impedance	5 - 100 kHz	R.Marshall [20]
	Four electrodes, Impedance	350 Hz	P.D.Carter [23]
Ewe	Two electrodes, Impedance	Not specified	P.M.Barlewski [28]
	Two electrodes, Impedance*	10 Hz - 100 kHz	L. Adam [27]
Sow	Two electrodes, Ohmeter	DC	L.Dusza, S. Yamauchi [9, 10]
	Four electrodes, Impedance	5.7 kHz	P.Rezac [13–16]
Rat	Two electrodes, Ohmeter	DC	S.D.Ramos [33]
	Two electrodes, Impedance	1 kHz	C.Taradach, L.Bartos [30, 32]

Table 3.1: Comparison of instruments used for animal fertility detection. * Note that two electrodes measurement data were corrected numerically to compensate electrode polarization impedance.

First, the range of frequency measured is limited. Capacitive and inductive properties depend on the frequency of the input signal. Accordingly, a narrower range may be unable to capture these properties [36]. For example, Lewis measured the impedance value only at 40 kHz for cattle [19] and Rezac acquired the data only at 5.7 kHz for sows [13–16]. If the impedance is measured at a single frequency, it is impossible to capture the effect of capacitive and inductive properties in an attempt to model the system of interest. Hence, it is recommended to measure the impedance over a range of frequencies. Only few instruments used in these studies were capable of obtaining the data at a wide range of frequency [20, 27]. Nonetheless, these instruments are expensive and bulky

which may not be suitable for field tests of stock animals. Also no rationale was provided for the choice of frequency.

Furthermore, most of instruments presented in this table measure the impedance with the two electrodes measurement technique. There is a huge drawback for this technique. When two electrode are employed, the impedance data contain the electrode polarization impedance coming from the electrode plus the impedance of the sample as Schwan demonstrated extensively [37]. Due to this electrode polarization effect, the data can be signficantly erroneous. To compensate the electrode polarization (EP) impedance, Schwan strongly suggests using a four electrodes measurement technique which separates the current flowing to the electrodes and the voltage flowing back to the electrodes [38]. The recommended materials for the electrode are gold and platinum which are known to be less prone to the EP effect [39]. Even though it is possible to numerically correct the electrode polarization effect as Adam described in his research, it is much easier to use a four electrodes technique which does not require arduous post-processing of the data [27]. Therefore, this study aims to develop a portable, inexpensive, and robust impedance spectroscope that can quickly obtain the impedance data over a wide range of frequency using a four electrodes measurement technique.

3.4 Instrument Design

3.4.1 Electrical impedance spectroscope

A portable, inexpensive, and robust electrical impedance spectroscope was designed and developed during this study. The impedance spectroscope was manufactured based on the AD5933 chip that allows impedance measurement in a portable system. To accomplish portability requirement, a single board microcontroller called BeagleBone Black (Texas Instruments) was used as a computing core which allows communication between the AD5933 and users. Wi-Fi dongle was attached to the microcontroller to enable wireless communication capability. The AD5933 is a very powerful chip that can measure impedance at a frequency range from 1 kHz up to 100 kHz. However, this chip performs two electrodes measurement technique instead of four by default, and this setup can cause erroneous EP effects that deteriorate the quality of data [37]. Therefore, a novel analog front

end (AFE) to enable four electrodes measurement technique was developed. The total estimated cost of the device is less than $100 including a microcontroller unit and the AFE.

The customized web application software was programmed on a microcontroller to create front-end user interface that receives users request from smart devices. The application software was developed based on Javascript engine called, Node.js. In order to simplify instrument operation, web application adopts user-friendly user interface (UI) based on Bootstrap UI template. The web application is also capable of displaying the new impedance data in real time as well as the saved data. Although the application also lets users to calibrate the system and to modify the sweep frequency range, these features need to be handled with a caution as described in the software.

3.4.2 Probe design

Based on the cylindrical electrode design presented for cattle and rats [19–22, 30], the electrode probe was constructed using four gold rings and PVC rod pipe. Gold rings were used as the electrode to minimize electrode polarization (EP) [39]. An inexpensive PVC pipe was chosen as a structural material for the electrode, and the handle is assembled with 3D printed PLA (Poly-lactic acid) material. The designs were coined and manufactured by the undergraduate student, Benjamin Thompson and the professor, Kaustubh Bhalerao. The detailed diagram of the gold ring probe is shown in the Figure 3.2.

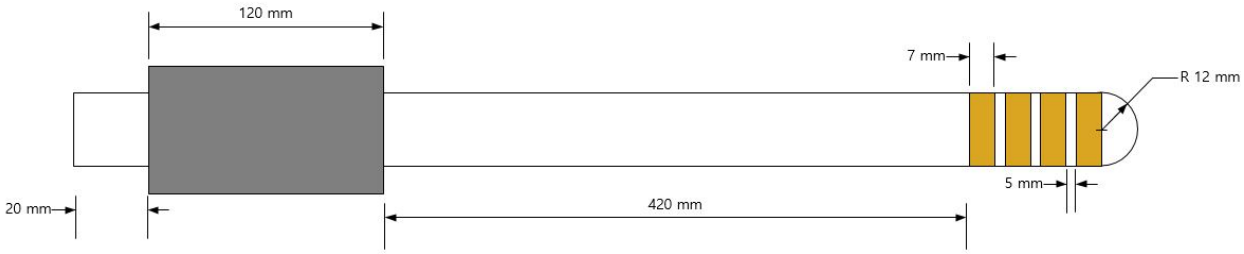

Figure 3.2: Four electrodes probe design with dimensions.

3.5 Materials and Methods

3.5.1 Instrument set up

The frequency increment was set to 1 kHz, so 100 data points in total were obtained. The AD5933 chip requires a calibration step before actual measurements, and it is critical to know the estimated value of unknown sample impedance. According to previous research [11–16], values of vaginal electrical impedance (or resistance) are reported to be approximately less than 200 Ω. Few other studies reported values to be in between 200 and 500 Ω [9,10], therefore the impedance spectroscope was calibrated with a 100 Ω resistor which permits measurement up to 500 Ω. Note that the instrument injects 200 mV_{p-p} of a small excitation voltage to the sample not only to measure low impedance but also to minimize damaging reproductive tissues.

3.5.2 Sanitary Solution and Lubricant

In this study, the same probe was used to collect the impedance data during all experiments. Because the probe is inserted inside of the vaginal tract, it has to be disinfected before each measurement in order to prevent contamination between sows. According to previous research, there are several options of sterile solution for the probe [8,17,18]. Instead of using 70% alcohol or diluted Chlorhexidine, diluted Povidone-Iodine solution was used in this study. The Iodine solution is extremely diluted to prevent soft reproductive tissues from being damaged which may affect the fertility of sows. During the experiment, the probe was disinfected by first being submerged into the dilluted Povidone-Iodine disinfectant (10 %), and was thoroughly rinsed with the tap water solution. Then, the probe was wiped with a paper towel to eliminate any residue on the probe. Repeated measurements without lubricant could cause bleeding of reproductive tissues due to the friction between the probe and tissues. As a means to prevent any damage to these tissues, a lubricant (First Priority) was used to reduce the friction between reproductive tissues and the probe before inserting the probe.

3.5.3 Experimental design

In the first experiment, impedance measurements were recorded once a day to determine if the change of electrical impedance would reflect the time of estrus in sows. The day of estrus (Day 0) was checked by observing the standing response of sows in the presence of a sexually mature boar. The probe was disinfected with the diluted Iodine solution and the deionized water solution in between each measurement. After the disinfection process, the probe was lubricated; then it was inserted into the vaginal tract of each sow. The data were collected two more days after the day of estrus was detected to illustrate the change in impedance after the estrus onset.

A second experiment was conducted to check if the impedance spectroscope could capture the timing of farrowing. The same standardized measurement procedure from the first experiment was performed for ten pregnant sows who were expected to give birth to piglets within eight days. Electrical impedance measurements were taken once a day over eight days, and the day of farrowing was denoted as Day 0 as well. The data from first and second experiments were collected by colleagues, Audrey Walker and Lidia Sbaraini Arend under Professor Robert Knox's instruction.

A third experiment was carried out to collect the impedance data on a larger scale with the aid of JBS United company. The aim of this experiment was the same as the first experiment, but ninety-two weaned sows were measured during this experiment. Instead of checking the day of estrus daily, this experiment was planned to record impedance data for a complete estrous cycle. Note that the impedance spectroscopy was reprogrammed to measure at a range between 1 kHz and 30 kHz in order to speed up measurement process. JBS researchers were trained to execute the standardized procedure to keep the consistency of all experiments.

3.6 Results

3.6.1 Experiment 1

The impedance spectrum throughout the estrous cycle of ten sows, and the change of impedance value during the estrous cycle at five different frequencies (1 kHz, 2 kHz, 5 kHz, 10 kHz, and 20 kHz) are presented in Figures 3.3, and 3.4 respectively. As shown in these figures, the last day measurement for sow number 116 and the fourth-day measurement for sow number 15 were not

taken during the actual experiment. Although there are two missing data points, the impedance spectrum increased four days before the beginning of estrus and decreased two days before the onset of estrus. In order to clarify these changes, the average values of vaginal impedance during the estrous cycle at five different frequencies was plotted in log-log scale and is shown in Figure 3.5. The change of average impedance between Day -4 and Day -2 is 163.42 Ω with standard deviation of 53.30. This indicates that impedance trend of reaching nadir can be easily recognizable. High standard deviation can be accounted for the fact that all sows have different vaginal mucus contents from one other. It is also worth noting that Figure 3.5 contains shadowed region to represent 95 % confidence level interval for a smoothly fitted curve.

According to the plot shown in Figure 3.5, the impedance value increased sharply four days before the onset of estrus, then the lowest impedance value was reached two days before the beginning of the estrus. After estrus, the impedance value gradually increased and did not seem to reach the highest value observed at four days before the estrus. The change in impedance value is more distinguishable at a lower frequency as illustrated in Figure 3.5. This change in impedance spectrum follows the trend observed from previous research. Peter et al. [13–16] reported that there was the marked decrease in vaginal impedance in all sows during proestrous and the lowest value was measured 1-2 days before estrus onset. In addition, experiments using Draminski's resistance sensor showed that the lowest value of vaginal resistance was achieved 1-2 days before estrus onset [9, 10]. Based on these findings, it is evident that our results are congruent with their data.

Even though there had been extensive research efforts to find the relationship between the vaginal impedance and the estrous cycle, factors that influence the change in impedance spectrum are still poorly comprehended. Peter and Dusza [9, 15] inferred that a sudden decrease in vaginal impedance might be related to the change of physiological structure and function of the vagina induced by the LH peak and plasma estradiol secretion. Because impedance measurements reflect not only vaginal mucus but also vaginal vestibule tissues, one can only speculate that the decrease in impedance value accounts for the increase in sodium chloride concentration in vaginal mucus and hydration of the vaginal vestibule tissues. Regardless of the difficulty of defining the exact causes of the change in vaginal impedance, a high correlation between the lowest vaginal impedance and LH

peak from Peter's research suggests that the impedance spectrum can be used as a supplementary indicator for predicting the onset of estrus one or two days after the lowest value has been measured.

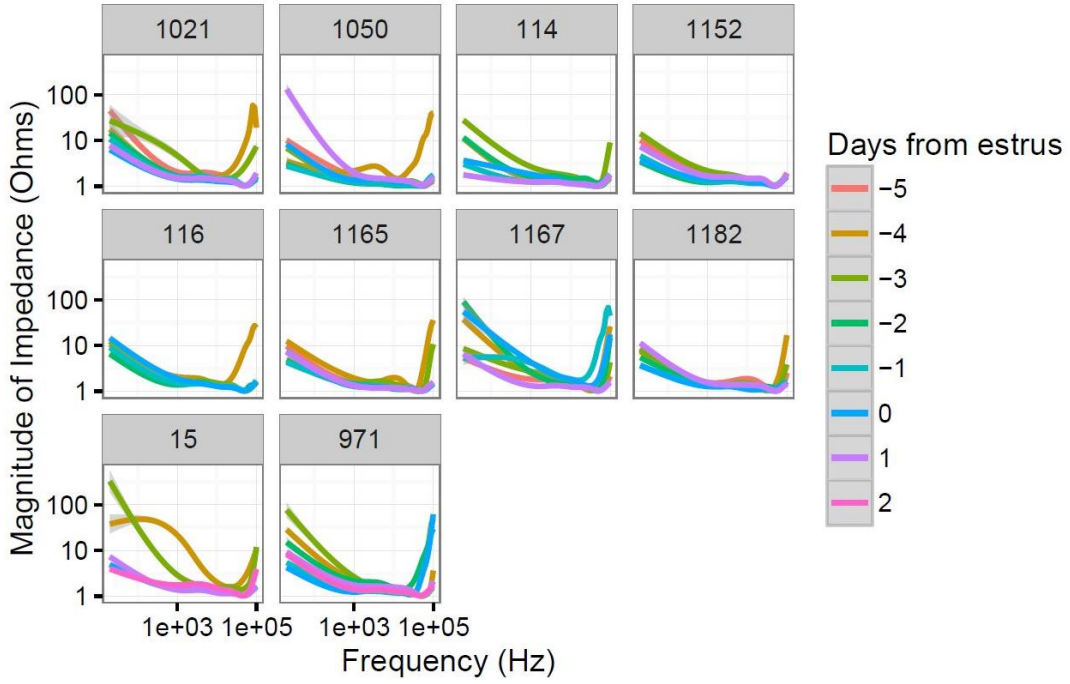

Figure 3.3: Impedance spectrum of ten sows over eight days following weans.

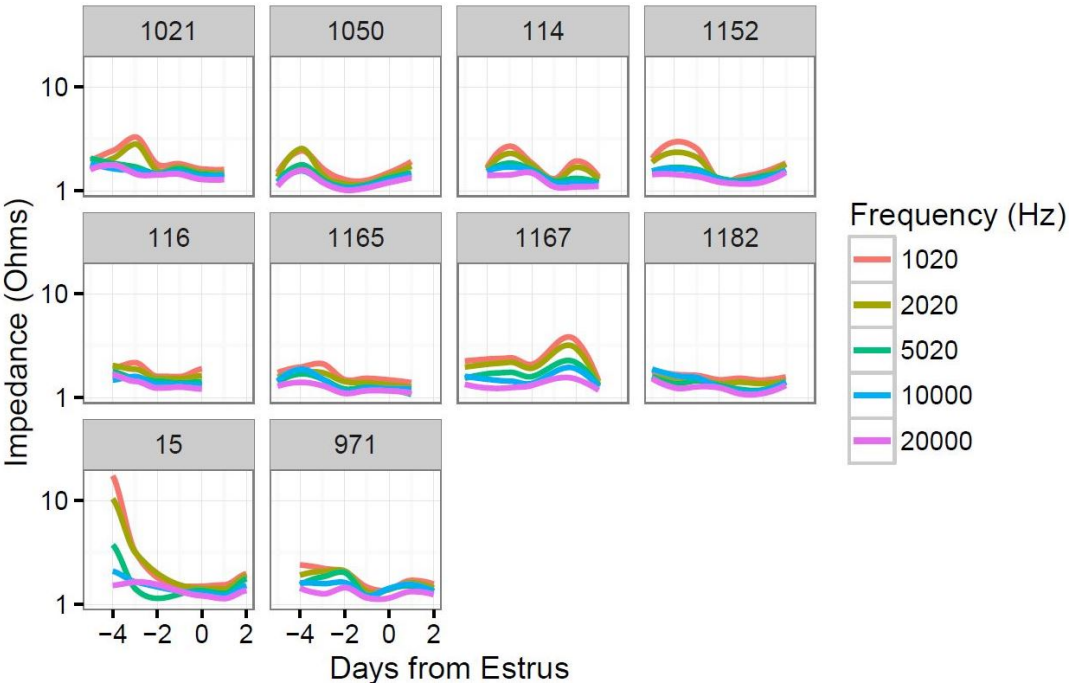

Figure 3.4: Change of impedance value during the estrous cycle at five different frequencies.

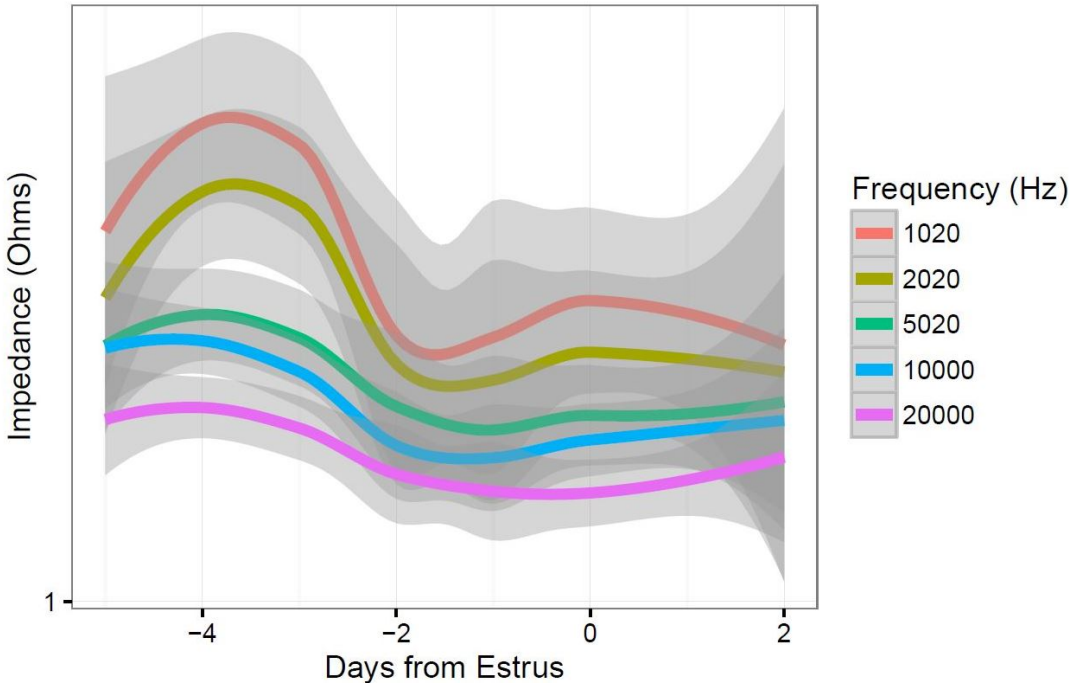

Figure 3.5: Impedance increases sharply and reaches the peak four days before the onset of estrus. Then, the nadir of impedance value is achieved approximately two days before the onset of estrus. Lower frequency data showed much sharp change of impedance compared to higher frequency data. Shadowed region represents 95 % confidence interval. Note that the change of average impedance value between Day -4 and Day -2 is 163.42 ± 53.30.

3.6.2 Experiment 2

The vaginal impedance of ten pregnant sows was measured roughly a week before they gave birth to a litter of pigs. The impedance spectrum throughout eight days and the change of impedance value during the measurement cycle at five different frequencies (1 kHz, 2 kHz, 5 kHz, 10 kHz, and 20 kHz) are presented in Figure 3.6, 3.7 correspondingly. As illustrated in Figure 3.7, it is seen that there is slight increase in impedance two days before farrowing and the impedance continues to decrease after the day of farrowing. As a means to visualize these changes, the average values of vaginal impedance are plotted in log-log scale at five different frequencies as illustrated in Figure 3.8. According to results, the change of average impedance between Day -4 and Day -2 is 72.26 Ω with standard deviation of 8.32. This suggests that impedance value rises slightly two days before the farrowing day and its decreasing trend persists until two days after farrowing, but the change of impedance is not as dramatic as compared to the results from the estrus experiment.

Similar to this experiment, Tasal et al. [18] compared the electrical resistance of vaginal mucus between pregnant and non-pregnant cattle to detect early pregnancy. Based on their findings, Tasal concluded that the electrical resistance may be used to predict ovarian status and stages of estrus due to the higher resistance value in pregnant cattle compared to non-pregnant cattle [18]. However, there is currently no other research conducted on sows to monitor the farrowing time using impedance spectroscopy, and it is still unclear whether the increase in impedance two days before farrowing day is caused by the change of physiological structure and function of the vagina. Therefore, further studies will be necessary to identify the correlation between vaginal impedance and hormonal changes as well as to obtain more data from large numbers of sows to corroborate the results demonstrated in this study.

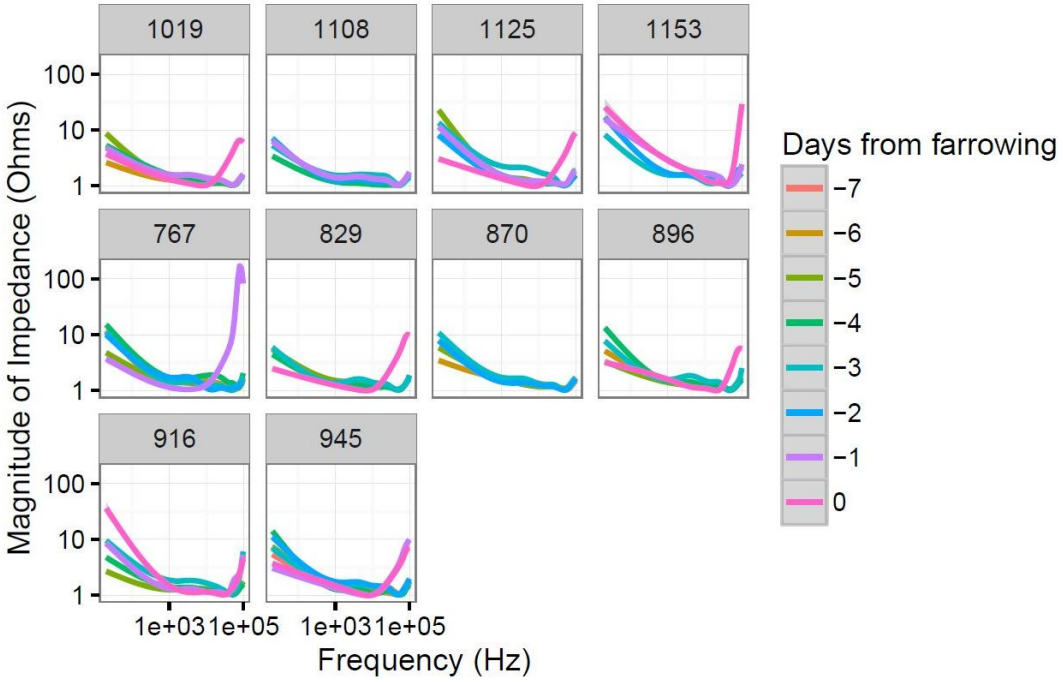

Figure 3.6: Impedance spectrum of ten sows for the farrowing experiment.

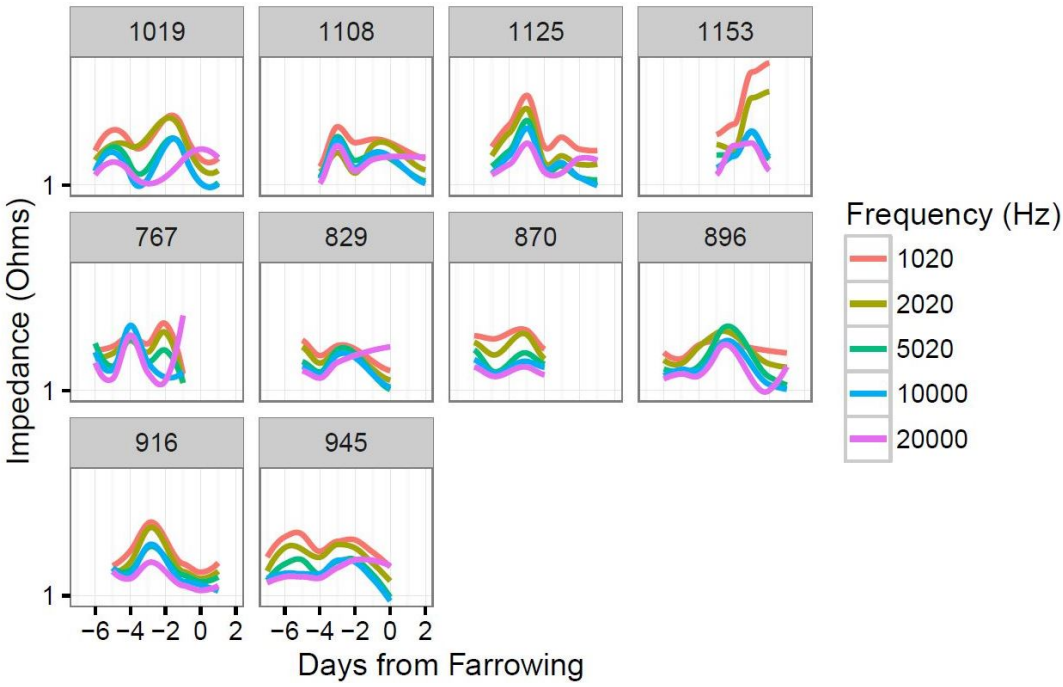

Figure 3.7: Change of impedance value for the farrowing experiment at five different frequencies.

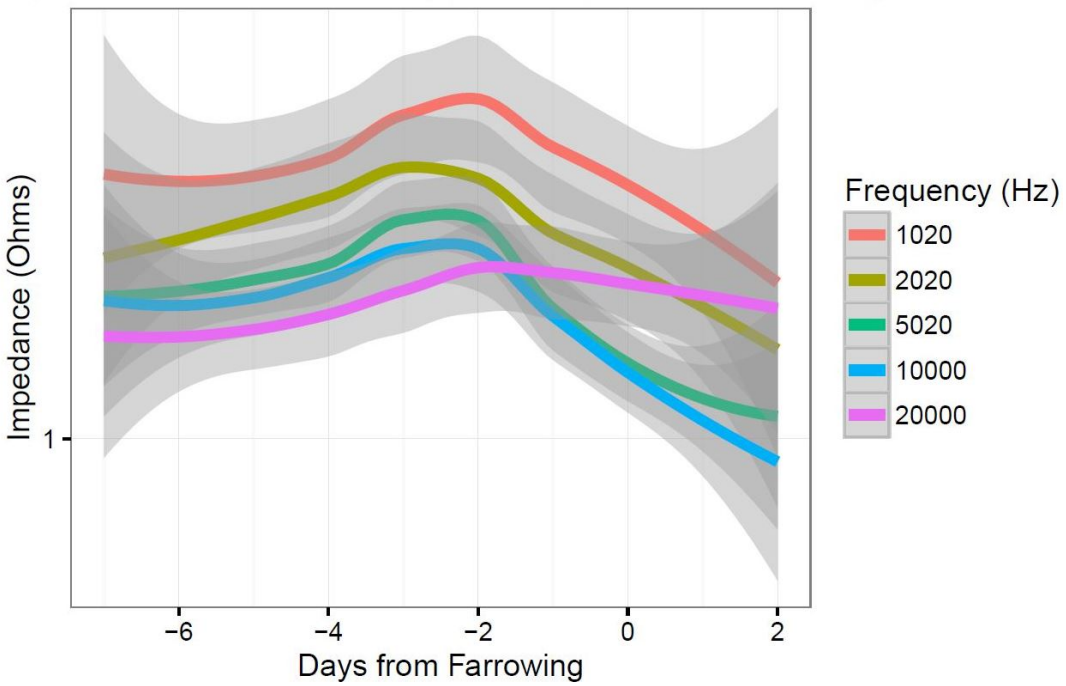

Figure 3.8: Impedance increases sharply until two days before farrowing. Lower frequency data showed much sharp change of impedance compared to higher frequency data. Shadowed region represents 95 % confidence interval. Note that the change of average impedance value between Day -4 and Day -2 is 72.26 ± 8.32.

3.6.3 Experiment 3

Unlike other domesticated animals, sows return to estrus a 3 days after weaning, hence estimating weaning to estrus interval (WEI) is an essential activity of managing the fertility of sows. Failure to breed at next estrus will delay pig production and increase costs. According to Poleze's statistical analysis on 15,600 breeding records from Brazilian farm, 70 % of parity 1 sows and 82.5 % of higher parity sows returned to estrus within 3-5 days [40]. Even though weaned sows may return to estrus any time within 21 days, statistical data suggests that the majority of weaned sows, 77.8 % including parity 1 and greater, exhibit estrus within 3-5 days [40]. As demonstrated in the previous study, many breeding farms expect to observe estrus from weaned sows between three and five days postweaning.

In this experiment, the developed portable impedance spectroscope was deployed at the research farm owned by JBS United to collect the data from 92 weaned sows. The research began on the day after weaning and was planned to be continued until the start of second estrus onset, however, this experiment was halted due to the device breakdown on the second day. Based on the records kept by JBS researchers, smooth impedance spectrum was obtained at first measurement for 59 sows (64.1 %), second measurement for 23 sows (25 %), third measurement for 8 sows (8.7 %), and fourth measurement for 2 sows (2.2 %). The variability of impedance value was less than 5 Ω. Possible causes of this variation are due to the movement of animals during measurement and electrode contact failure inside the vaginal tract. Since impedance spectroscope has an advantage of producing the whole spectrum over a range of frequency, a small variation in impedance value can be leveraged by analyzing the entire spectrum. Averaged impedance and phase spectrum from 92 sows on the first day after weaning are presented in Figure 3.9, 3.12 respectively. Based on these figures, impedance and phase values from 92 sows on the first day after weaning do not significantly vary and stay consistent over a sweep frequency range. This suggests that even though individual sows can show different impedance values, it may be possible to identify estrous cycle of sows due to very small variations.

In order to identify characteristics of the vaginal impedance, the data was fitted to a model with a resistor and a capacitor in series. A resistor represents the vaginal mucus impedance, and a capacitor denotes the double layer capacitance formed at the electrode-sample interface. Because

a simple RC series model failed to fit the phase data closely due to the inductive behavior is seen at a high frequency range above 10 kHz, multiple attempts using more complex models were made to fit the both data. Nevertheless, complex models either produced similar results or failed to converge to local minima when Gauss-Newton's nonlinear least squares algorithm was applied. As a result, a new element that can properly explicate the phase spectra has to be devised and added to a simple RC series model in the future.

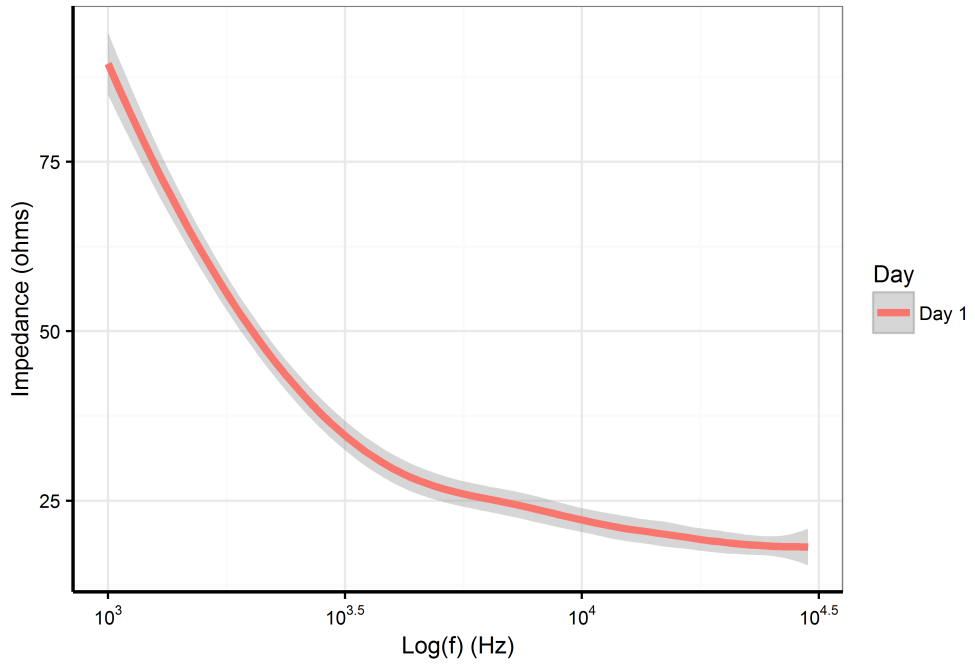

Figure 3.9: Averaged impedance spectrum from 92 sows on the first day after weaning.

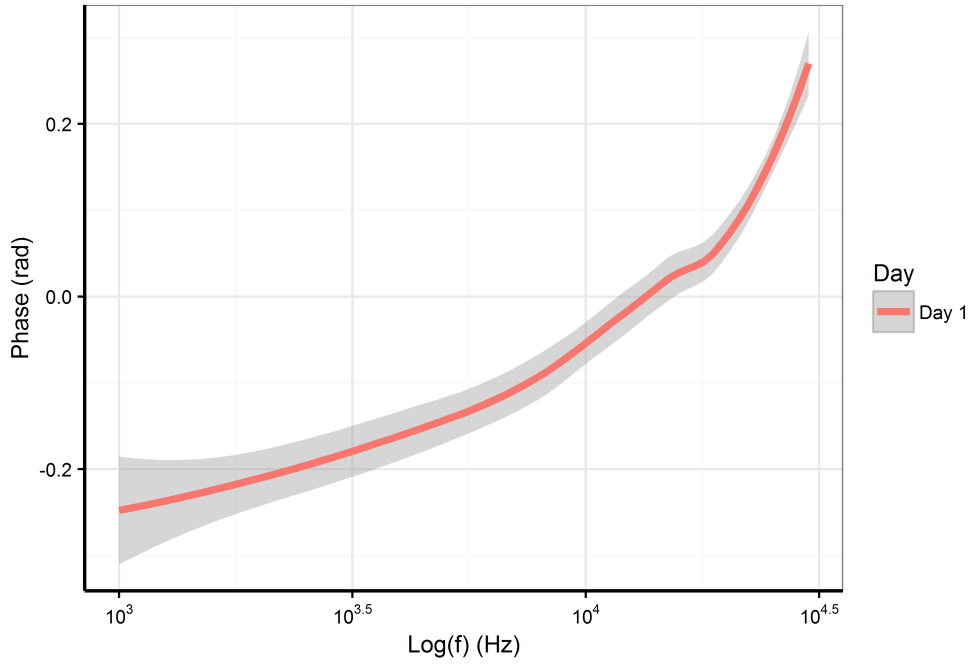

Figure 3.10: Averaged phase spectrum from 92 sows on the first day after weaning.

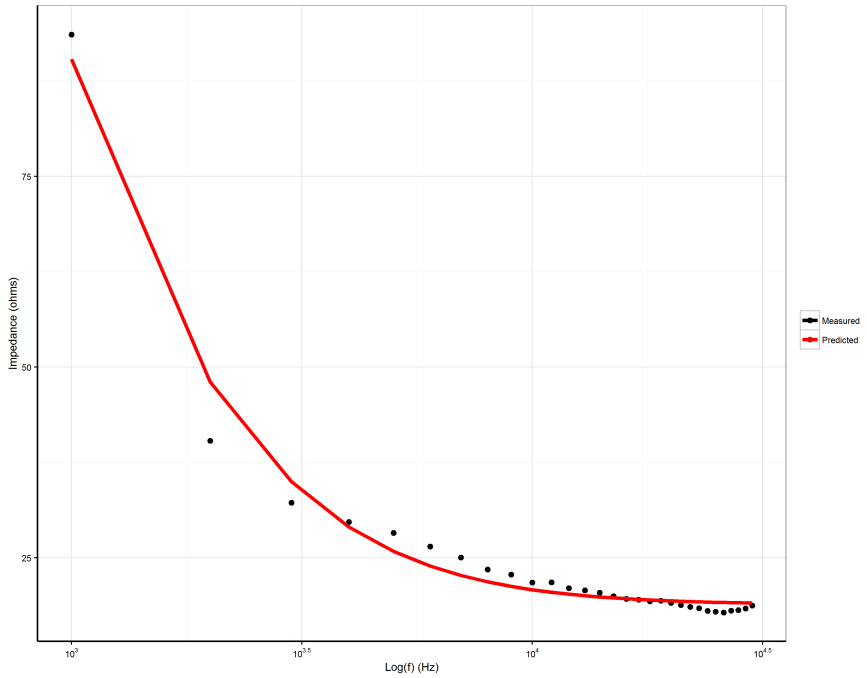

Figure 3.11: Averaged impedance data fitted to reproductive tissue model. Measured data is well explained by the proposed model.

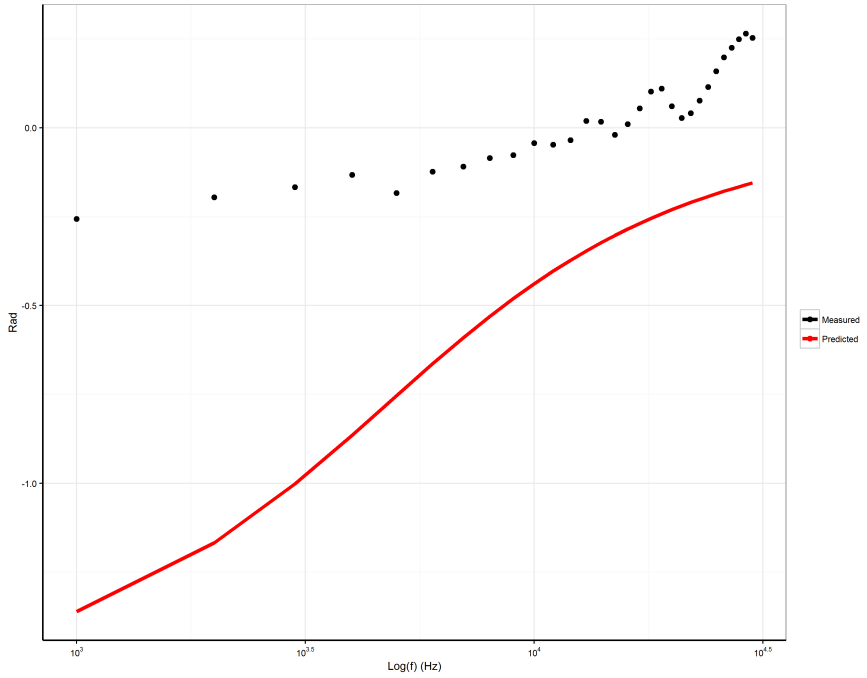

Figure 3.12: Averaged impedance data fitted to reproductive tissue model. Measured data can not be explained by the proposed model due to inductive behaviors at a high frequency range.

3.7 The cause of device failure and the solution

JBS researchers reported the failure of the system in the field and stopped the experiment. According to their report, the device produced open circuit results randomly on the first day then it stopped producing good results after few measurements on the second day. A similar issue was also reported by colleagues who attempted to collect more data at a swine research center in Urbana-Champaign after the changes were made on the electrode design and the AFE. Because the problem was not reproducible at all, we have tried several steps to solve the problem.

Firstly, the wire of the electrode was replaced to be more thick and robust. The connection between the electrode and the system has to be intact during measurements since losing a contact directly produces open circuit results. Also, strain relief was added to the wire in order to prevent the cables breaking away from the connector on the board. Regardless of these changes, the same problem was observed in the field. Secondly, the old version microcontroller was swapped with the newer version of the microcontroller to check if any unexpected errors were produced by it. Even though the microcontroller, the operating system, and the software were upgraded to new version, this modification did not solve the problem.

At last, the quality of the portable battery was tested and specification sheets for all electrical components used on the AFE were reviewed. The portable battery was tested with a multimeter to ensure that it provides stable 5V supply to the microcontroller, since failure to do so can cause problems on the AFE. According to results, the portable battery was unable to produce steady 5V power below room temperature. At room temperature, the battery provided at least 4.91V steadily, however, when it was stored at 4 $^{\circ}C$, the power from the battery fluctuated between 4.73V and 4.85V. Moreover, when measurements begin, the voltage dropped further below 4.5V shortly and came back to 4.8V which can potentially cause malfunction on the AFE. Therefore, the cheap, poor quality portable battery was switched to the more robust and higher capacity one by Anker.

In addition, another problem on the AFE design was found after reviewing specification sheets on electrical components. When the electrode was redesigned, there was a small modification on the AFE by replacing the instrumentational amplifier chip from the INA 826 to the AD 8220 as the latter one has a slightly better performance. After this little modification, colleagues continuously reported that the device in-field produced open circuit impedance data randomly. This open circuit

data was produced by the AD 8220 which has a better performance but strictly requires 4.5V power supply, whereas the old one, INA 826, only requires 3V power supply. Therefore, as a compensation of performance, the robustness of the deivce reduced after the modification. Based on what we have tested, we concluded that the failure of the device in-field was due to both the poor quality battery and the new version of the amplifier chip. The device works properly without failure after replacing the battery and the amplifier chip.

3.8 Discussion and Future work

The preceeding results from three experiments showed that impedance spectroscopy can be used to characterize the estrous cycle or farrowing time of sows. Our results demonstate that the vaginal impedance sharply decreases and reaches the nadir, and these results corroborate previous studies. Results for detecting farrowing time also suggests that the vaginal impedance decreases two days before the farrowing day. Regardless of rigorous research attempts, it is still unclear what casuses the vaginal impedance to reduce a few days before either estrus or farrowing, but the change in impedance value can be correlated to hormonal changes occurring during the estrous cycle.

During the third experiment, the device failed to operate properly in the field. As demonstrated eariler, the problem was due to an unstable power source from the low quality portable battery and an instrumentational amplifier modification on the extension circuit. By employing a high quality portable battery and changing a new version of amplifier back to an old one, we were able to fix the problem of device failure in-field.

Future work will improve the hardware design to reduce the cost further and to increase robustness of the impedance spectroscope. Instead of using a Wi-Fi connection, the next version will use Bluetooth technology provided by finger-sized microcontroller platform called Adafruit Feather 32u4. After the development of a newer device, we aim to continue collecting impedance spectra from a large number of sows using multiple devices to validate the capability of impedance spectrsocope as a decision-making tool to optimize artificial insemination in swine breeding operations.

3.9 References

[1] R. E. Taylor and T. G. Field, *Scientific farm animal production : an introduction to animal science*. NJ: Prentice Hall, 2001.

[2] G. C. Lamb and N. DiLorenzo, *Current and future reproductive technologies and world food production*. NY: Springer Science and Business Media, 2014.

[3] R. V. Knox et al., "An analysis of survey data by size of the breeding herd for the reproductive management practices of north american sow farms," *American Society of Animal Science*, vol. 91, pp. 433–445, 2013.

[4] R. R. Kraeling and S. K. Webel, "Current strategies for reproductive management of gilts and sows in north america," *Journal of Animal Science and Biotechnology*, vol. 6, no. 3, pp. 1–14, 2015.

[5] N. M. Soede et al., "Reproductive cycles in pigs," *Animal Reproduction Science*, vol. 124, pp. 251–258, 2011.

[6] L. L. Anderson, "Reproductive biology of pigs," *Animal Industry Reports*, vol. 655, no. 66, pp. 1–8, 2009.

[7] R. N. Kirkwood, "Pharmacological intervention in swine reproduction," *Swine Health*, vol. 7, no. 1, pp. 29–35, 1997.

[8] J. P. Charuest et al., "Postweaning vaginal mucus conductivity and breeding performance at artificial inseminaion in swine," *Canadian Journal of Animal Science*, vol. 70, pp. 451–457, 1990.

[9] L. Dusza et al., "The relationship between electrical resistance of vaginal mucus and plasma hormonal paramters during periestrus in sows," *Theriogenology*, vol. 45, pp. 1491–1503, 1996.

[10] S. Yamauchi et al., "Prediction of the estrous cycle and optimal insemination time by monitoring vaginal electrical resistance (ver) in order to improve the reproductive efficiency of the okinawan native agu pig," *Animal Reproduction Science*, vol. 113, pp. 311–316, 2009.

[11] D. M. Hidalgo et al., "Relationship between vaginal mucus conductivity and time of ovulatin in weaned sows," *The Canadian Journal of Veterinary Research*, vol. 79, pp. 151–154, 2015.

[12] M. F. Zink and J. R. Diehl, "Efficacy of using vaginal conductivity as an indicator of the optimum time to breed in swine," *Journal of Animal Science*, vol. 59, no. 4, pp. 869–874, 1984.

[13] P. Rezac et al., "Effect of probe location on changes in vaginal electrical impeedance during the porcine estrous cycle," *Theriogenology*, vol. 59, pp. 1325–1334, 2003.

[14] P. Rezac et al., "Effect of sow parity on vaginal electrical impeedance," *Animal Reproduction Science*, vol. 72, pp. 223–234, 2002.

[15] P. Rezac and I. Olic, "Relationship between opposite changes of vaginal and vestibula impedance during estrous cycle in sows," *Theriogenology*, vol. 66, pp. 868–876, 2006.

[16] P. Rezac, "Potential applications of electrical impedance techniques in female mammalian reproduction," *Theriogenology*, vol. 70, pp. 1–14, 2008.

[17] M. Tadesse et al., "The use of vaginal electrical resistance to diagonse estrus and early pregnancy and its relation with size of the dominant follicle in dairy cattle," *Kasetsart Journal - Natural Science*, vol. 45, no. 3, pp. 435–443, 2011.

[18] I. Tasal et al., "Estimation of early pregnancy by electrical resistance values of vaginal mucosa in cows and heifers," *Revue Med Vet*, vol. 156, no. 2, pp. 91–94, 2005.

[19] G. S. Lewis et al., "Changes in electrical resistance of vulvar tissue in holstein cows during ovarian cycles and after treatment with prostaglandin $f_{2\alpha}$," *Animal Reproduction Science*, vol. 18, pp. 183–197, 1989.

[20] R. Marshall et al., "Electrical conductivity probes for detection of estrus in cattle," *Transactions of the ASAE*, pp. 1145–1156, 1979.

[21] F. Feldmann et al., "The electrical conductivity inside the bovine vaginal wall," *Animal production*, vol. 26, pp. 61–65, 1978.

[22] W. Leidl and R. Stolla, "Measurement of electric resistance of the vaginal mucus as an aid for heat detection," *Theriogenology*, vol. 6, no. 23, pp. 237–249, 1976.

[23] P. D. Carter and J. H. Dufty, "Assessment of vaginal impedance measurements as an indicator of oestrus in cattle," *Australian Veterinary Journal*, vol. 56, pp. 321–323, 1980.

[24] M. B. Aboul-Ela et al., "Relationships between intravaginal electrical resistance, cervicovaginal mucus characteristics and blood progesterone and lh," *Animal Reproduction Science*, vol. 5, pp. 259–273, 1982.

[25] A. R. Lehrer et al., "Bio-impedance monitoring of genital tissues of cows as an aid in cattle reproductive management - a review," *Proceedings of the New Zealand Society of Animal Production*, vol. 55, pp. 221–223, 1995.

[26] D. Schams et al., "The oestrous cycle of the cow: Hormonal parameters and time relationships concerning oestrus, ovulation, and electrical resistance of the vaginal mucus," *Acta Endocrinologica*, vol. 86, pp. 180–192, 1977.

[27] L. Adam et al., "Impedometric properties of the vulvar and vaginal tissues of ewes during the oestrous cycle," *Journal of Reproduction and Fertility*, vol. 61, pp. 11–17, 1981.

[28] P. M. Bartlewski et al., "The relationship between vaginal mucous impedance and serum concentrations of estradiol and progesterone throughout the sheep estrous cycle," *Theriogenology*, vol. 51, pp. 813–827, 1999.

[29] E. Theodosiadou and T. Tsiligianni, "Determination of the proper time for mating after oestrous synchronisation during anoestrous or oestrous by measuring electrical resistance of cervial mucus in ewes," *Veterinarni Medicina*, vol. 60, no. 2, pp. 87–93, 2015.

[30] C. Taradach, "Monitoring of the oestrus cycle in the rat by measurement of vagina impedance," *Arch. Toxicology Supplement*, vol. 5, pp. 184–186, 1982.

[31] L. M. Jaramillo et al., "Using vaginal wall impedance to determine estrous cycle phase in lewis rats," *Lab Animal*, vol. 41, no. 5, pp. 122–128, 2012.

[32] L. Bartos, "Vaginal impedance measurement used for mating in the rat," *Laboratory Animals*, vol. 11, pp. 53–55, 1977.

[33] S. D. Ramos et al., "An inexpensive meter to measure differences in electrical resistance in the rat vagina during the ovarian cycle," *Journal of Applied Physiology*, vol. 91, pp. 667–670, 2001.

[34] K. A. Gupta and G. N. Purohit, "Use of vaginal electrical resistance (ver) to predict estrus and ovarian activity, its relationship with plasma progesterone and its use for insemination in buffaloes," *Theriogenology*, vol. 56, pp. 235–245, 2001.

[35] E. Barsoukov and J. R. Macdonald, *Impedance spectroscopy: theory, experiment, and applications, 2nd edition.* NJ: Wiley, 2005.

[36] A. Lasia, *Electrochemical Impedance Spectroscopy and its Applications.* NY: Springer, 2014.

[37] H. P. Schwan, "Alternating current electrode polarization," *BioPhysik*, vol. 3, pp. 181–201, May 1966.

[38] H. P. Schwan, "Four-electrode null techniques for impedance measurement with high resolution," *The Review of Scientific Instruments*, vol. 39, no. 4, Apr. 1968.

[39] Z. Moron, "Considerations on the accuracy of measurements of electrical conductivity of liquids," presented at the XVIII IMEKO World Congress, 2006.

[40] E. Poleze et al., "Consequences of variation in weaning-to-estrus interval on reproductive performance of swine females," *Livestock Science*, vol. 103, pp. 124–130, 2006.